CONFIDENTIAL
RESTRICTED DATA
Atomic Energy Act 1954

Astronuclear

WANL-TNR-002

NOTICE

This report was prepared as an account of work sponsored by the United States Government. Neither the United States nor the United States Energy Research and Development Administration, nor any of their employees, nor any of their contractors, subcontractors, or their employees, makes any warranty, express or implied, or assumes any legal liability or responsibility for the accuracy, completeness or usefulness of any information, apparatus, product or process disclosed, or represents that its use would not infringe privately owned rights.

WESTINGHOUSE ELECTRIC CORPORATION
ASTRONUCLEAR LABORATORY
P. O. Box 10864
Pittsburgh 36, Pa.

March, 1962

Classification cancelled (or changed to ...)
by authority of DOE
by ...

SHIELDING & RADIATION ANALYSIS - NERVA PHASE 1 ACTIVITY

(Title Unclassified)

NERVA NUCLEAR SUBSYSTEM

MASTER

CONFIDENTIAL
RESTRICTED DATA
Atomic Energy Act 1954

ATTACHMENT I

Number	Title	Class.
[illegible]-TNR-002	Shielding & Radiation Analysis - NERVA Phase I Activity	CRD
[illegible]-TNR-003	Reactor Nuclear Design-NERVA Phase I Activity	CRD
[illegible]-TNR-004	Reactor Thermal Design-NERVA Phase I Activity	CRD
[illegible]-TNR-006	NERVA Reactor Support Information for E-MAD Facility Phase I	CRD
[illegible]-TNR-007	Interface Studies Phase I	CRD
[illegible]-TNR-008	Reactor Shield Design Phase I	CRD
[illegible]-TNR-009	NERVA Beryllium Reflector Phase I	CRD
[illegible]-TNR-012	Cantilever Bending Tests of KIWI B-1 Module Phase I	CRD
[illegible]-TNR-021	Reliability Program Plan Phase I	CRD
[illegible]-TNR-022	Reliability Program Phase I	CRD
[illegible]-TNR-024	NERVA B-1 Reactor Phase I	CRD
[illegible]-TNR-025	NERVA B-2 Reactor Phase I	CRD
[illegible]-TNR-026	NERVA B-4 Reactor Phase I	CRD
[illegible]-TNR-027	NERVA Design Requirements Phase I	CRD
[illegible]-TNR-033	Materials for Design	CRD
[illegible]-TNR-034	Reactor Control System NERVA Phase I	CRD
[illegible]-TNR-035	Reactor Control Components Phase I	CRD
[illegible]-TNR-036	Control Drum Actuator Development	CRD
[illegible]-TNR-038	Transient Reactor Experiments on NERVA Fuel Material	CRD
[illegible]-TNR-039	Re-Entry and Burnup of Reactor Fragments	CRD
[illegible]-TNR-040	Survey of Fission Product Release from NERVA Fuel Material	CRD
[illegible]-TNR-050	Advanced Reactor Study Phase I	CRD
[illegible]-TNR-062	Laminar Flow Instabilities Part I	CRD
[illegible]-TNR-067	Aerodynamic Heating and Oxidation of Graphite in Free Molecule Flow Regime	CRD
[illegible]-TNR-070	Toxicity of NERVA Reflector Material Following a Launch Pad Accident	CRD

Number	Title	Class.
[illegible]-TNR-072	Experimental Study of the Re-Entry Oxidation of NERVA Fuel	CRD
[illegible]-TNR-075	Preliminary Investigation of NERVA Core Destruct Chemicals	CRD
[illegible]-TNR-076	KIWI B-5 Shield Design and Fabrication	CRD
[illegible]-TNR-076	KIWI B-5 Shield Volume II Radiation Design and Analysis	CRD
[illegible]-TNR-076	KIWI B-5 Shield Volume III Thermal Design and Analysis	CRD

Astronuclear

ABSTRACT

SHIELDING AND RADIATION ANALYSIS

NERVA PHASE I ACTIVITY

This report describes shield nuclear and thermal design data, and radiation environment data generated during Phase I of the NERVA Contract. The shield nuclear analyses include definitions of the radiation environment around a shielded and unshielded core, propellant tank heating for the shielded and unshielded conditions, and a vehicle optimization study for determining the minimum weight of the vehicle system required to limit the propellant heating to an acceptable level. The thermal analyses were carried out for both the heated bleed and the hot bleed cycles. Various heat exchanger shield design configurations were investigated and are included in this report.

TABLE OF CONTENTS

(Table of Contents, Cont'd)

LIST OF TABLES

(List of Tables, con't)

(List of Tables, con't)

(List of Tables, con't)

LIST OF FIGURES

(List of Figures, con't)

(List of Figures, con't)

(List of Figures, con't)

(List of Figures, Con't)

1.0 INTRODUCTION

The purpose of this report is to present the information generated during Phase I of the NERVA Contract pertaining to shield nuclear and thermal design and to the reactor radiation environment.

The proposed shield for the NERVA engine is an integral part of the reactor assembly. The primary purpose of the shield is to reduce the heating of the hydrogen in the propellant tank in order to minimize the vehicle system weight.

The mechanical design of the shield and the physical properties of the lithium hydride neutron shield material are described in detail in other reports.

The nuclear analysis includes the definition of the radiation environment around a KIWI B-1 reactor which has operated for 20 minutes at 1120 MW, for both the unshielded and what is presently conceived to be the maximum shielded case.

The total heat input to the propellant tank for an unshielded condition was calculated for three tank bottom half angles of 25°, 30°, and 37.5° for a 30 foot diameter tank. A parametric study of various shield thicknesses and diameters was then carried out to determine their effect on the heat input to the propellant tank for the same three half angles.

A vehicle shielding optimization study was also performed to determine the minimum weight of the vehicle system required to limit the propellant heating to an acceptable level. Some of the parameters in the study included: separation distance of core and propellant tank, shield thickness, tank angle, and pressure of the propellant in the tank.

Several heat exchanger shield design configurations were investigated including a flat plate capsule geometry, and various types of cylindrical capsule geometries. Thermal analyses were carried out for both the heated bleed and the hot bleed cycles.

2.0 SUMMARY AND CONCLUSIONS

The radiation environment around an unshielded and a maximum shielded KIWI B-1 reactor core has been presented for subsequent determination of heating rates, activation data, and other analysis pertaining to the engine, vehicle components, and propellant of the NERVA system.

Two separate nuclear radiation studies were carried out. The first dealt with a minimum weight shield system based on shield parameters of thickness, distribution, and shape for a 90% reduction in total propellant tank heat input and at the minimum tank to engine separation distance as determined by engine component arrangement. From this study, it was determined that the shield composition should be 63% lithium hydride, 27% stainless steel and 10% void for coolant passages. It should have a uniform thickness over the core radius and have a conical lateral surface reducing to zero thickness at the reflector radius for all tank bottom geometries.

For a 90% heat attenuation in a 30 foot diameter tank with a bottom angle with respect to the core center of 37.5°, a shield is required which has a thickness of 31.5 cm and weights 1660 pounds. It is note-worthy that only 3% of the total shielded heat input to the propellant is due to fast-neutrons. Thus, the gradient of heat deposition at the front face of the propellant and any tendancy for the propellant to stratify is markedly reduced by the shield.

The second study, termed the optimization study, included the following parameters: separation distance of core and propellant tank, shield thickness, tank angle with respect to the core center, and propellant pressure. This study determined the minimum weight system based on the assumption that 10% of the propellant remained in the tank at the end of

operation and that at this point the hydrogen was a saturated liquid. The flow model within the tank during operation was the completely mixed case.

Several recommendations can be made as a result of the optimization study. (1) A tank angle of 37.5° should be used as a basis for preliminary designs. (2) The tank design pressure should be 20 psia, or the minimum commensurate with structural requirements. (3) The optimum shield weight for a 30 psia tank pressure is about 650 lbs. The arrangement for this system consists of a lithium hydride - stainless steel shield covering the reflector radius (62 cm.), and having a 9.5 cm. thickness; the bottom of the tank is located 8.5 feet above the core center. This shield weight can be reduced to some extent by shaping.

When a more definite value is established for the amount of propellant to remain in the tank for decay heat cooling purposes, the optimization study must be reviewed. In general, however, it does not appear that a 90% heat attenuating shield at minimum tank to engine separation will be required if the propellant flow model approaches the mixed flow case.

The shield mechanical design selected for a flight engine after investigation of many possible configurations consists of cylindrical lithium hydride pellets encased in stainless steel cylinders that are sealed with welded steel end plugs. These capsules are 0.5 inches in diameter and are bundled between two steel support plates in a triangular array to form the shield.

The radiation heating deposited in a 31.4 cm. thick shield is approximately 2.1 MW. The maximum heat rate is 0.60 BTU/sec - in^3 at the face of the shield immediately above the reactor. For the heated bleed cycle which flows approximately 4.0 pounds per second of hydrogen through the shield, the maximum temperature of the lithium hydride pellets is maintained at about 700°R below their melting temperature even with the adverse tolerance buildup condition.

3.0 SHIELD NUCLEAR DESIGN

3.1 ANALYTICAL METHODS

Shielding Computer Program 14-0[1] was used to calculate gamma ray fluxes and dose rates, and fast neutron dose rates in and around the reactor-shield assembly.

This program evaluates point-to-point kernel functions and integrates over cylindrical source regions to perform reactor-shield penetration calculations. Reactor and shield geometries are described by combinations of regions formed by rotation of rectangles and trapezoids about the reactor-shield axis or parallel axes or by translation of convex quadrilaterals parallel to any axis of the rectangular coordinate system. Compositions are expressed as volume fractions for each material in the reactor-shield assembly and are associated with the appropriate geometrical regions by code numbers. The distances traversed from each source point to the detector are determined by a stepping procedure in conjunction with an analytical procedure.

Cylindrical volume, cylindrical or plane surface, axial or radial line, or point sources may be described. Source-density distributions must be the same for neutrons and gamma rays, and are assumed independent of angular position, but are separable along the radius and axis of the source region.

Gamma ray fluxes and dose and energy absorption rates can be computed for positions around sources emitting photons of as many as twenty source energies. Exponential attenuation is used in conjunction with empirical expressions for combining buildup factors in light and heavy material.

An extensive modification of a material attenuation function suggested by R. D. Albert and T. A. Welton[2] is used for computing fast neutron dose rates from fission sources in mixtures of hydrogenous and heavy shield materials. This theory combines a theoretical hydrogen cross-section with integration over the fission neutron spectrum to obtain the uncollided flux as a function of penetration distance into the shield medium. The attenuation effects of materials other than hydrogen are included by assuming exponential attenuation and treating the cross section as energy - independent adjustable parameters to be determined by best fit to experimental data. This treatment is based on the assumption that all heavy materials are followed by sufficient hydrogenous material that the use of effective removal cross sections is valid. The fast neutron dose rate is thus not energy dependent since the method of calculating the neutron kernel results in an integration over the fission neutron energy spectrum.

In spite of the limitations of point kernel calculations, the results of experiments of comparing calculations and measurements within and outside of very complex shields have been quite encouraging.

These measurements include water centerline dose rates from the Oak Ridge Bulk Shielding Reactor, and centerline water and oil traverses at the Lid Tank Shielding Facility. The latter experiments included materials such as steel and lead between the source plate and the detector. Recently, successful comparisons were made with experimental data obtained at the GE-ANPD Battelle Source Plate Facility. These experiments included radiation measurements through and behind arrays of single and multiple shield materials. In addition, the point kernel programs agreed within the limits of experimental error with

calorimetric nuclear heating experiments performed at the Shield Test Pool Facility at the GE-ANPD Idaho Test Station.

In addition, the point kernel method is versatile and readily adaptable to digital computer solution. Consequently, the method can be used to perform shield analyses quickly.

A one-dimensional multigroup P1 code is presently being used for calculating neutron flux data. This code, P1MG[3], solves the one-dimensional P1 equations in the consistent Greuling - Goertzel approximation for fifty-five groups. The code produces as output, multigroup fluxes for 54 fast groups and one thermal group. Currents, isotopic slowing-down densities, and pointwise and regionwise few-group macroscopic cross sections are also obtained.

Diffusion theory has been applied primarily to the analysis of reactors. Its use for shielding applications has been more limited because the diffusion approximation tends to make the spatial dependence of the calculated fluxes inaccurate in shield regions. However, it appears that while diffusion theory leaves something to be desired in the calculation of the spatial dependence of fluxes in shields, it is suitable for calculating the energy dependence of these fluxes. Once the fluxes can be normalized, the energy spectrum becomes available.

A recent technique[4] has been developed in which the point kernel program is used to obtain the spatial distribution of the neutrons, and the diffusion program is used to obtain the energy distribution. The diffusion results are then normalized at each detector point by the ratio of the fast neutron dose rate computed by the point kernel method to that computed by the diffusion method as follows:

$$D_1 = D_{14-0} \frac{\int_u \phi(u)du}{\int_u \phi(u)\, K(u)du}$$

where D_1 = normalized neutron total flux

D_{14-0} = point kernel fast neutron dose rate

$\phi(u)$ = program P1MG output flux at each lethargy level, u

$K(u)$ = response of the detector used to measure the D_{14-0}, i.e., Hurst dosimeter response function.

The normalizing factor can then be applied to the various lethargy or energy groups in order to obtain useable neutron energy flux data.

Presently, the thermal diffusion theory constants used as input to Program P1MG are being obtained from a SOFOCATE[5] code. This code assumes a hydrogen moderated reactor with a thermal cutoff energy of 0.625 ev. All shielding calculations to date have been based on these data. In the future, diffusion theory constants will be obtained from the TEMPEST[6] code which uses a 1.86 ev cutoff for a graphite moderated reactor. Therefore, the neutron flux data used in the present shield analysis will change, but to what extent is not yet known.

Methods development is necessary for improving shielding calculations. This development will include utilization of, and comparison with, two-dimensional codes, transport theory, and Monte Carlo calculations.

3.2 UNSHIELDED RADIATION CONDITIONS

3.2.1 FLUXES AND DOSE RATES AROUND THE CORE

The configuration used in these calculations consisted of the reactor core, the graphite and beryllium reflector, the aluminum top support plate, and a cylindrical aluminum pressure vessel. The dimensions considered are as follows:

	Radius	Length	Void Volume Fraction
Reactor Core	17.74 inches	4.33 feet	0.168 and 0.178
Graphite	19.94	4.58	----
Beryllium	24.44	4.33	0.10
Pressure Vessel	24.94	5.04	----
Top Support Plate	17.74	0.58	0.65

An approximate drawing of the geometry is shown in Figure 1 (1/8 scale). Rotation of the rectangles about the Z axis results in cylindrical geometry.

The reactor core was considered in two sections, having void volume fractions of 0.168 and 0.178, respectively. A void fraction is defined as that part of the volume of the material allowed for coolant passages. The aluminum top support plate is about 0.9 inches longer than that in current designs.

Shielding Computer Program 14-0 was used to calculate gamma ray fluxes for thirteen source energy groups at twelve azimuthal angle (α) positions at 5, 10, and 20 feet around the reactor assembly. This angle is measured from the core centerline with the top end of

the core designated 0°, i.e., $\alpha = 180^{\circ}$ would be the nozzle end. The source-detector separation distance is measured from the center of the active core.

Within the cylindrical reactor source regions, approximately 1100 source points were distributed over one-half the core. The source point spacing was varied depending on the detector point location. A skewed cosine function was used to describe the axial power distribution. The radial power was assumed to be flat. The reactor total power output was equal to 1120 megawatts. The gamma ray source energy fission spectrum for thirteen energy groups consisted of contributions due to prompt fission gamma rays, short half life gamma rays, delayed gamma rays, and those due to neutron capture in U_{235}. The reactor operating time was assumed to be twenty minutes.

In computing the gamma ray point kernels, water dose buildup factors were applied to all materials. This assumption is valid since water has an effective Z of about 7.5. This is similar to carbon (Z = 6), aluminum (Z = 13), and beryllium (Z = 4).

Gamma ray fluxes for each energy group, as well as the total, are presented in Tables 1, 2, and 3 for distances of 5, 10, and 20 feet from the center of the reactor core. Appropriate conversion factors were applied to obtain gamma ray dose rates, rads/sec, for each energy level. These dose rates are presented in Tables 4, 5, and 6 at each of the above distances.

Although a decrease in the gamma flux might be expected at $\alpha = 0^{\circ}$ over that at 180° due to a shielding effect of the support plate, such is not the case. This is because the power distribution values at that end of the core are higher than at the nozzle end, which

counteracts the effect of the support plate shielding.

Gamma ray total iso-fluxes are presented in Figure 2. The gamma ray total iso-dose rates are plotted in Figure 3.

Fast neutron dose rates at the same angular positions around the unshielded reactor were computed using the neutron point kernel function coded in Program 14-0. However, in the case of a "bare" core calculation, where very little hydrogenous material is present, this kernel has to be altered somewhat. In place of the hydrogenous kernel, a carbon kernel was used. This carbon kernel was fitted to moments method data[7] consisting of differential neutron number flux as a function of distance in carbon due to a unit, point, isotropic, fission neutron source. Removal cross sections were then applied to all non-carbon type materials. The resulting fast neutron dose rate is not energy dependent, and is that due to neutrons of all energies.

At $\alpha = 0^{\circ}, 90^{\circ}$, and 180°, the resulting neutron dose rates were converted to fluxes, assuming an emergent neutron energy of 1 Mev. Since these fluxes appeared reasonable, it can be assumed that the fast neutron dose rates are correct within the limits of a point-to-point attenuation method.

The fast neutron dose rates in rads(ethylene)/sec for each angle and distance are presented in Table 7 and are plotted in Figure 4.

For convenience, the total dose rates are plotted in Figure 5, and presented in Table 8.

The neutron spectra in the vicinity of the core were obtained using a one-dimensional multigroup P1 code, 'P1MG'.

For this analysis, the core was split into 11 regions axially and 7 regions radially and the 55 group neutron spectra were calculated along the axis and the radial line of symmetry from the unshielded core. These data were then normalized by integration with the Hurst response function to the corresponding 14-0 fast neutron dose rates to obtain the total fast neutron and thermal neutron fluxes as shown in Tables 9 and 10 and Figure 6. Table 11 then gives the fast neutron fluxes for 26 energy groups at 5 feet from the core axially, top and bottom, and radially, on the line of symmetry. Since the reactor is considered operating in void, these same spectra distributions can be used at other distances.

Additional calculations were performed to determine the dose rate and flux levels at several positions one foot from the pressure vessel surface, and one foot from the nozzle end of the reactor core.

Several changes were made in the physical description. The beryllium reflector void fraction was increased to 20 per cent, and the top support plate thickness was decreased to six inches. A nine inch thick void region was inserted between the support plate and the pressure vessel to simulate more accurately a shielded configuration.

To facilitate the use of these data, the actual location of the detector points is presented here in tabular form. The center of the cylindrical coordinate system is located at the center of the reactor core, (r = 0, Z = 0).

Astronuclear

Angle, α	r, cm.	Z, cm.
0°	0	139.71
25°	45.059	139.71
54°	93.849	66.04
90°	93.849	0
126°	93.849	-66.04
162°	45.059	-96.52
180°	0	-96.52

The gamma ray fluxes, gamma ray dose rates, fast neutron dose rates, and total dose rates for the above detector locations are presented in Tables 12, 13, 14, and 15, respectively. Fast neutron and thermal fluxes for $\alpha = 0^\circ$, 90°, and 180° are presented in Table 16.

Fluxes at positions very close to a cylindrical volume source do not follow the usual geometrical attenuation function, $1/D^2$, where D refers to the separation distance of source and detector. Only sources which are essentially a "point" source exhibit this phenomenon. Hence, these data cannot be reasonably plotted in the iso-flux and iso-dose curves presented in this report.

3.2.2 UNSHIELDED PROPELLANT TANK HEATING

For an analytical approach to the propellant heating problem, it is necessary to know both the magnitude and distribution of heat deposition in the tank. This knowledge of the heat distribution is desirable in selecting plausible flow models from which temperature rises can be calculated. In this study, it was assumed that heat is deposited in the propellant by three processes distinguished by the type of interaction involved. The relative heating magnitudes due to these processes will determine the total heat distribution. The following is a brief description of these three processes pertaining to interactions in liquid hydrogen:

1) Core gamma ray interactions;

Gamma rays interact with matter through many interaction processes of which three are of primary importance: pair production, photoelectric effect, and Compton scattering. The first two reactions represent pure absorption processes in which the gamma ray energy is absorbed. The third interaction is characterized by a fractional energy transfer taken up by the atom recoil. Due to its comparitively weak electron binding energy and electric field, hydrogen can be considered a pure Compton scatterer. Figure 7 shows attenuation of core gamma radiation in the liquid hydrogen propellant of density 4.4 lbs/ft^3. A factor of ten reduction is attained in about 8.1 feet of propellant. These data are based on Program 14-0 calculations using the KIWI B-1 core as a cylindrical source located ten feet from the tank bottom.

2) Fast neutron elastic scattering;

Fast neutrons are slowed down in liquid hydrogen by multiple scatterings, and are subsequently

absorbed. These scatterings result in an essentially complete transfer of energy taken up by the kinetic motion of the hydrogen atoms. The scattering is isotropic in the center-of-mass system with an average of 63 percent energy degradation per collision. Figure 7 shows that a factor of ten reduction is attained in about 1.3 feet of propellant.

3) Capture-gamma reaction;

As the neutron is being slowed down, its probability of absorption increases. These absorptions will result in a change in the energy level of the hydrogen atom, converting it to deuterium, and in the process emitting a 2.23 Mev gamma ray. These "capture" gammas then interact with the hydrogen, releasing heat in the same manner as the core gamma ray radiation described above

From the above discussion, it is evident that core-gamma radiation and thermal neutron radiation causing production of capture gamma rays, will effect heat deposition throughout the propellant, whereas fast neutron heating will be concentrated toward the front face of the propellant tank and will be negligible further into the propellant.

Tank heat input data were calculated for three different tank angles, 25°, 30°, and 37.5° The lower section of the tank is assumed to be the frustrum of a cone, the apex of which is located at the center of the reactor core; the major base is equal to the tank diameter (30 feet) and the minor base is 8.437 feet above the center of core The tank angle is half the angle of the cone In Table 17 are listed the total heat input for each of the three tanks, as well as that for each of the three processes previously described. These results indicate that about 52% of the total heat is due to core gamma radiation, 37% to capture gammas, and 11% to fast neutron scattering

The gamma and neutron energy fluxes were calculated at ten detector points on each tank surface. These fluxes were then adjusted by the inverse R^2 effect using the core-center

as the reference point to obtain the fluxes over a plane area at the bottom of the tank. Figures 8, 9, and 10 illustrate the heat input versus radial position on this plane area for the three tank angles. The heat inputs are broken down into the neutron kinetic, capture gamma, and core gamma components. Total heat inputs were obtained by integrating the normal component of the total energy flux over the plane area.

These heat input data were calculated using both Program 14-0 and Program P1MG. Program 14-0 was used to calculate the core gamma ray heating for 13 energy groups, and the fast neutron dose rate at each detector point. About 1100 source points were located in one-half of the reactor core volume in these problems. The neutron flux calculated using Program P1MG was normalized to the fast neutron dose rate data. These fluxes were, of course, centerline data, but should be reasonably valid at any position along the tank surface.

3.3 SHIELDED RADIATION CONDITIONS

3.3.1 PARAMETRIC DATA FOR DETERMINING SHIELD THICKNESS

Two material configurations were included in this study: 1) a homogeneous lithium hydride and stainless steel mixture, and 2) liquid hydrogen and borated stainless steel. Stainless steel was selected because it is both an excellent gamma shield material and a good structural material. Lithium hydride and liquid hydrogen were selected because of their low density, yet high hydrogen atom density which is one of the requirements for a good neutron shield material.

Program 14-0 was used to compute the gamma ray and neutron dose rates at a detector point located on the centerline at the bottom of the propellant tank with various thicknesses of both types of shields located above the top of the support plate. The shield covered the entire core radius. A six inch-thick aluminum top support plate and a one-half inch thick aluminum pressure vessel were included in the calculations.

Shield thicknesses included in this study are as follows:

1) 30, 40, and 50 centimeters of lithium hydride, each containing 0, 20, 40, and 60 per cent stainless steel;

2) 0, 6, and 12 inches of liquid hydrogen, each combined with 0, 2, 4, and 6 inches of borated stainless steel.

Results of these parametric data are shown in Figures 11 through 14 inclusive. The actual gamma ray heat flux as a function of shield thickness is presented for each type shield. However, due to the many hand calculations required to obtain neutron heating rates, only neutron dose rate is presented in Figures 12 and 14. It was then assumed that the heat flux was proportional to the dose rate.

It was previously established that about 52% of the total heat input to the propellant tank was due to core gamma radiation and about 48% due to neutrons. With this knowledge, the following equation can be established to determine the heat input to the tank as a fraction of the unshielded heat input.

$$P = 0.52\, F_\gamma + 0.48\, F_n$$

where P = Fraction of unshielded propellant heat input

F_γ = Ratio of shielded to unshielded heat due to gamma rays

F_n = Ratio of shielded to unshielded heat due to neutrons.

Several values of the fraction P were selected for investigation, namely, .2, .1, .07, and .04, which correspond to attenuations of 80, 90, 93, and 96 per cent. It was believed that within this range of centerline attenuation, an optimum would exist which would produce a total reduction of 90% in total propellant heating for a 30-foot diameter tank.

Several shield thicknesses and compositions were analyzed to determine the resulting values of P. Typical results thus obtained are illustrated in Figure 15 where the fraction P is plotted as a function of shield thickness (lithium hydride and stainless steel). From these curves, for instance, it will be seen that several different shields can produce a fraction P = .2, or 80% attenuation along the centerline.

Since, more than one shield thickness, depending on its material composition, would produce a desired P value, it was necessary to determine which shield was a minimum weight shield. In determining the minimum weight shield it is necessary to include the effect of additional interstage and plenum weights associated with thick shields. The minimum weight shield for P = .2, for instance, is shown in Figure 16 where the total weight (including shield weight, and vehicle and plenum weights) is plotted as a function of per cent by volume of steel. These results are also presented in Table 18.

It was assumed that a tank-core center separation distance of 8.437 feet and a plenum thickness of 5" are minimums. On this basis, the interstage vehicle weight per inch of shield above 5" was calculated to be 28.57 lbs/in., and the plenum weight, 8 lbs/in. For a shield radius equal to the core radius the combined vehicle and plenum weights would be equivalent to 1.024 gms per cm^3 of shield for thicknesses greater than 5 inches.

Similar calculations were performed for the liquid hydrogen - borated stainless steel shield.

It soon was evident, however, that the liquid hydrogen - borated steel shield was heavier on a gm/cm^2 (thickness x density) basis than the lithium hydride - steel shield. As an example, for a 90% centerline attenuation, the minimum total weight liquid hydrogen - steel shield was 83.9 gm/cm^2 compared to 68 gm/cm^2 for the lithium hydride - steel shield.

The shield thickness for the lithium hydride – steel system determined in the above manner were utilized as described in the next section of this report to determine their effect on total tank heat input.

3.3.2 SHIELDED PROPELLANT TANK HEATING

Propellant heating may result in two adverse effects. Extreme temperature rises will induce cavitation and unsteady flow at the pump inlet for a selected tank pressure. Secondly a thicker and therefore, heavier tank wall will be required for an increased pressure in the tank to prevent cavitation. The former effect will determine a maximum tolerable but not necessarily desirable, heat input. The desirable heat input will be that which gives a minimum over-all system weight determined by the trade-off between tank weight for pressurization and shield weight for attenuation. These effects are discussed in more detail in Section 3 4 which describes the vehicle optimization study.

Pending the results of experimental data*, an analytical model of propellant flow is not now sufficiently defined so as to correlate propellant temperature rise with tank heat input. To avoid design stagnation, this dilemma has been temporarily circumvented by arbitrarily choosing a 90% heat input reduction factor as a criterion for shield design Shield design will henceforth be modified commensurate with the availability of reliable experimental date.

The results discussed in the previous section of this report show that the optimum shield material for reduction factors in the range 80 – 96% on the centerline consists of lithium hydride with 27% by volume of stainless steel. The purpose of this section is to present the results of optimizing the radial distribution and shape of the shield independent of other

* Experiments to be carried out by LASL and the Lewis Laboratory.

parameters as discussed in Section 3.4 on the optimization study. Table 19 lists the shield thicknesses for various centerline attenuating factors using lithium hydride with 27% stainless steel as the shield material.

To determine the effect of shield radius on tank heating, heat inputs were calculated for the three tank angles using two shield radii and shield thicknesses corresponding to 80, 90, 93, and 96% centerline reduction factors. In the case of the 96% shield the tanks were moved 10 cm. further from the core to retain the same space between the pressure vessel and the tank bottom. The shield radii examined correspond to the core radius (45.059 cm) and the reflector radius (62.099 cm). Tables 20, 21, and 22 and Figure 17 contain the results of this study. Tables 20 and 21 list for each tank angle the total heat input for each shielded case, and the per cent reduction. Table 22 lists the weight of each shield. Presented in graphical form in Figure 17 are the total heat inputs for each shielded case for each tank angle, versus shield weight. (The data for the 45° tank angle referred to in Figure 17 were extrapolated). Figures 18, 19, and 20 illustrate the variation of tank heat input with radial position on a plane area at the bottom of the tank for the three tank angles using the 90% centerline reduction shield and both shield radii. In the shielded case the heat input for the larger radius shield consists of approximately 84% core-gamma, 13% capture gamma, and 3% neutron kinetic components. The corresponding percentages for the unshielded case are 52, 37, and 11%. Thus, the sharp heat input gradient due to neutrons will be rendered relatively less severe by shielding.

As can be seen in Figure 17 the larger radius shield gives the minimum weight of two radii examined for a 90% over-all heat input reduction and all tank angles. The following table gives the shield weights for a cylindrical shield of uniform thickness to the outer reflector radius for the 90% over-all heat input reduction at various tank angles.

Tank Angle (θ°)	Shield Weight (lb)
25°	1410
30°	1480
37.5°	2000
45°	2850

Radiation leaking from the reactor side is over-attenuated by the uniform thick shield. It seemed expeditious to shape the outer fringes of the shield. Using the thickness of the 96% centerline reduction shield as a base, the following configurations were examined for the 37.5° tank angle. (This angle was selected since the optimization study indicated that this is the optimum angle).

Case 1 -- A diagonal cut was made from a thickness of 31.86 cm. at the core outer radius to zero thickness at the reflector outer radius.

Case 2 -- A diagonal cut as in Case 1 but to a thickness of 15.93 cm. at the reflector outer radius.

The following table presents the results of these two cases and also the unshaped case, based on a 31.4 cm. uniformly thick shield to the reflector outer radius. The last column lists the per cent reduction per pound of shield for each case.

	Shield Weight lbs.	Over-all % Reduction	% Reduction/ Weight
Unshaped	2000	90.00	.045
Case 1	1660	89.60	.054
Case 2	1924	91.30	.047

It is evident that Case 1 in which the diagonal slice projects to zero thickness at the reflector outer radius has the weight advantage for the 37.5° tank angle. All the previous shielding analyses

included a void region above the beryllium reflector and adjacent to the aluminum support plate. The effect of filling this void with shield material was investigated to find if there would be a possible weight advantage in doing so. Case 1, as described above, was used for this purpose. The results are as follows: shield weight, 2066 lb.; per cent reduction, 92.73%; per cent reduction / lb., 0.0449 %/lb. Thus, filling the void region does not represent a weight advantage. This same effect was found for smaller tank angles.

Therefore, it is recommended that Case 1 be used as the shield design for the 25°, 30°, and 37.5° tank angles.

Such a shield weighs 1660 lbs. for the 37.5° tank angle as compared to 2000 lb. for the unshaped case. Shield weights for the 25° and 30° tank angles for Case 1 are 1176, and 1360 pounds, respectively. These weights do not include any shield structure.

3.3.3 SHIELDED FLUXES AND DOSE RATES (MAXIMUM SHIELD)

This analysis included a KIWI B-1 shield design similar to that described in Section 4.2 of this report. The lithium hydride encased in stainless steel cylinders was considered as a homogeneous mixture. An extremely precise geometrical description was used in Program 14-0 for calculating gamma ray flux data and fast neutron dose rates. This geometry included a description of the aluminum support plate, the stainless steel structure, and the pressure vessel, as well as the homogenized shield material. The shield used here was 31.4 cm. in thickness at the centerline commensurate for a 90% total heat reduction in a 37.5° angle tank (Section 2.3.3). This shield is anticipated to be the maximum size unit for consideration in the NERVA engine.

Calculational methods used are the same as those described in the previous section of this report describing the unshielded radiation environment. A new one-dimensional multigroup P1 problem was utilized for obtaining neutron spectra. A hydrogenous neutron kernel was used in Program 14-0 for computing fast neutron dose rates. The azimuthal angles considered to be affected by the shield are 0°, 15°, 30°, and 45°. The other angles were assumed the same as those computed in the non-shielded case.

Gamma ray fluxes for each energy group, as well as the total, are presented in Tables 23, 24, and 25 for distances of 5, 10, and 20 ft. from the core center. Gamma ray dose rates for each angle and distance are presented in Tables 26, 27, and 28. Fast neutron dose rates and fluxes are listed in Tables 29, and 30, respectively, and, for convenience, the total dose rates are listed in Table 31.

Table 32 gives the fast neutron fluxes for 26 energy groups at 5 feet from the core axially at the top on the line of symmetry ($\alpha = 0^\circ$).

Figures 21, 22, 23, and 24 illustrate, respectively, the shielded gamma ray iso-fluxes, gamma ray iso-dose rates, fast neutron dose rates, and total dose rates around the shielded reactor core assembly. As was stated previously, it was assumed that only four angles were affected by the shield, from $\alpha = 0^\circ$ to $\alpha = 45^\circ$. The data plotted for all other angles is the same as the unshielded environment data.

The shielded and unshielded data have certain dissimilarities which should be noted as follows: 1) the aluminum pressure vessel thickness was increased to more than one inch; 2) the top support plate design is no longer a right circular cylinder; 3) an improvement was made in the gamma ray source fission spectra data; and, 4) an hydrogenous kernel was used

for computing fast neutron dose rates outside the shield, rather than a carbon kernel as used in the unshielded case. The dissimilarities between the two cases affected the radiation levels by less than 1%.

The fast neutron and thermal fluxes at $\alpha = 0^{\circ}$ are presented in Figure 25 as a function of distance from the center of the reactor core.

3.3.4 SHIELDING EFFECT OF ENGINE COMPONENTS

A preliminary study was made to determine if the engine components affect the gamma and neutron flux incident on the bottom of the propellant tank.

Three engine components that lie along the core centerline were included. These are: the turbopump, the gimbal, and the tank shut-off value. The tank was considered to have a flat bottom located about 8.7 feet from the center of the core. The turbopump was located about one foot from the top of the pressure vessel, and was described as a right circular cylinder having a length of 1.6 feet and about a one foot diameter. The material of the pump was assumed to be 85% aluminum and 15% stainless steel by volume, with a total weight of about 300 pounds.

The gimbal was described as an annulus 0.45 feet in length, with an inner diameter of 0.419 feet and an outer diameter of 0.538 feet, the center of which was located 3.4 feet above the pressure vessel. The gimbal, consisting of titanium, weighed about 20 pounds.

The tank shut-off valve was described as an annulus 0.671 feet in length, with an inner diameter of 0.538 feet, and an outer diameter of 0.7 feet, located at the tank bottom. The valve, consisting of aluminum, weighed about 16 pounds.

Program 14-C was used to compute the dose rates at several radii along the bottom of the tank for both conditions, i.e., with and without the engine components. Results of this study are shown in Figure 2[illegible]. A shaped shield, 31.4 cm. thick on the center-line, was included in both cases.

These data indicate that over a small distance along the tank bottom these particular engine components decrease the dose rates significantly. At a radius of 10 cm. the gamma dose rate is decreased by a factor of 6.3, and the neutron dose rate, by a factor of 10.

These engine components effect a localized decrease in tank heating, but do not effect much of a decrease in the over-all propellant heating problem. Results are significant enough, however, to indicate that the shielding effect of other engine components located off the axis of symmetry must be analyzed. The results presented here are preliminary and are subject to change pending more accurate and up-to-date engine design configurations.

3.4 VEHICLE SHIELDING OPTIMIZATION STUDY

A study was made to determine the minimum weight of the system required to reduce the propellant heating to an acceptable level. The system defined here consists of the liquid hydrogen propellant tank, shield above the core, and the interstage weight required to separate the reactor core from the propellant tank. The temperature of the liquid hydrogen must be kept below saturation if the propellant is to retain reliable pumping qualities. This may be accomplished by increasing the pressure on the propellant or by limiting the tank heat input by means of a shield or separation distance. The study was based on the following parameters: -

Tank Shape	- 30' Dia. Cylinder with conical bottom
Tank (cone) Angle	- 37 1/2° truncated 8.45' above apex (base configuration)
Propellant Weight	- 97,680 lbs.
Tank Volume	- 22,200 ft^3
Minimum Separation	- 8.45 ft, center of core to bottom of tank
Effective Interstage Weight Factor for Nuclear Stage	- 1/2.7
Reactor Opercting Time	- 20 min. (1200 sec.)
Propellant Flow Rate	- 74 lbs/sec.
Shutdown Coolant	- 8800 lbs. LH_2 (= 10% of operating mass)
Heating Rate, Unshielded	- 1.24 MW at 37 1/2° and 8.45' (base configuration)
Shield Material	- 63% Li H, 27% SS and 10% void (volume)
Tank Pressure	- 30 psia (base configuration)
Allowable Temperature	- 42° (Saturation at 30 psia) (Base configuration)
Interstage Sleeve Weight	- 28.5 lbs/in.

The variable parameters considered were shield thickness and,

Separation Distance	- 8.45 ft - 25 ft.
Tank Angle	- 25° - 37 1/2°
Tank Pressure	- 20 - 40 psia

The propellant heating rate is affected by the following: 1) the distance between the tank and the reactor core (separation distance); 2) the shape of the tank, and 3) the radiation attenuation between the tank and reactor core. The study correlates these three factors as well as the effect on tank weight of several design pressures, and the corresponding allowable heating rates. An allowable heating rate is defined here as that which will not cause the liquid hydrogen to reach saturation temperature at the design pressure before engine cutoff after 20 minutes of operation, and with 10% propellant remaining in the tank.

The propellant tank may be separated from the core to reduce the solid angle subtended at the core and thereby reduce the heating rate in the propellant. The separation distances considered were measured from the center of the core to the bottom of the tank and ranged from a minimum dictated by engine equipment of 8.45 to 25 ft., which is the maximum believed practical. With the maximum separation distance of 25 ft., the heating rate is 1/5 of the value at 8.45 ft. These data are shown in Figure 27.

The bottom of the tank may be conically shaped to reduce the solid angle subtended from the core since the heating rate in the propellant is proportional to the volume "seen" by the core. Tank angles between 25° and 37 1/2° were considered. Decreasing the tank angle from 37 1/2° to 25° reduces the heating rate by 1/2. These results are shown in Figure 28. However, this change from 37 1/2° to 25° increases the hook-up distance between the nuclear

and chemical stages (interstage sleeve length) by approximately 13 feet. The increase in tank surface area and weight for decreasing tank angles was negligible.

The interstage sleeve and engine connection weight has been estimated to be 28.5 lbs./in., based on some previous work on the RIFT studies. Since this sleeve is not carried by the nuclear stage for its full mission as a shield would be, its weight effect on the payload will be less than a shield of equal weight. This "weight trade-off" factor for a 3-stage rocket with a mission within NERVA's capabilities has been determined to be 1/2.7. Thus, one pound of hardware weight or payload in the nuclear stage is equivalent to 2.7 pounds of hardware weight in the previous chemical stage. The weight trade-off factor between the first chemical stage and the third nuclear stage for this same vehicle was determined to be 1/11. The effective interstage weight used in this study was, therefore, 28.5/2.7 or 10.55 lbs/in. of length. The effective change in interstage and tank weight as a function of tank angle for several separation distances is shown in Figure 29.

A combined neutron and gamma shield placed above the core will also reduce the propellant heating. Lithium hydride plus 27% by volume of stainless steel has been chosen as the most effective shield based on attenuation per pound (see Section 3.3.1). Three shield arrangements have been considered; they are a shield which -

1. Covers only the core (radius - 45 cm.)
2. Covers the core and reflector (radius - 62 cm.)
3. Completely shadows the tank based on a point source located at the bottom centerline of the core.

The shield thickness will vary with tank angle, spearation distance and allowable heating rate. The shield thickness and weight were reduced as the separation distance was increased so that the propellant heating rate was approximately constant for each arrangement. The direct relation assumed between shield effect and distance effect is correct for the complete shadowing case but results in an overestimate of the weight for the limited radius shields since the smaller shields do not affect the total solid angle subtended by the tank, whereas, the separation does. The first two shields are easier to install than the third since they conveniently fit inside the reactor pressure vessel. The vessel must be enlarged to contain a shield which would completely shadow the tank at small separation distances and large tank angles.

A further weight reduction of the shield will be achieved when the shield is shaped for the most effective arrangement. This optimization study assumed the shields to be a simple disk of uniform thickness located above the core.

It was assumed that all the radiation energy impinging on the tank is absorbed by the propellant and is instantaneously mixed uniformly throughout the volume. The first assumption is conservative since the amount of gamma radiation absorbed will decrease as the liquid hydrogen level is lowered.

Three heat distribution models were considered: instantaneous mixing, no-mixing, and stratification. The instantaneous mixing model was used in this study because the acceptable heating rate for this model is lower than for the no-mixing model. Furthermore, baffles may be installed in the tank to prevent stratification if experiments show this condition to prevail.

The temperature of the 10 per cent propellant remaining in the tank after 20 minutes

of operation was determined for several heating rates assuming complete mixing. These temperatures and corresponding vapor pressures are shown as a function of heating rate in Figure 30. The temperatures were based on the specific heat values shown in Figure 31 (from WADD-TR-6056)[11] and a propellant flow rate of 74 lbs/sec. The tank weight was then determined as a function of heating rate (Figure 32) by combining the data of Figure 30 with a previous RIFT estimate of tank structural weight as a function of pressure (Figure 33). The tank wall consists of two aluminum sheets separated by 1 inch of fiber glass insulation.

An allowable heating rate for the 30 psia reference design tank was found to be 0.38 MW (Figure 30) for the complete mixing model. A preliminary investigation showed that a propellant flow rate of 74 lbs/sec. is adequate to remove this heat in the "no-mixing" model with less than the 5° temperature rise in the complete mixing case. Thus designing for the mixing case would give satisfactory operation if the flow obeys the "no-mixing" model.

Stratification of the heated propellant at the top of the tank could be prevented by installing suitable baffles in the tank. The effects of uninhibited stratification will be studied later in the program.

The reference system on which this study was based consisted of a 7400 lb propellant tank designed for an internal pressure of 30 psia and located 8.45 ft. above the center of the unshielded core. The bottom of the tank was conically shaped to reduce the heating rate. The unattenuated heat input to a $37\ 1/2^{\circ}$ tank was 1.24 MW, however, this arrangement does not limit the propellant heating to an acceptable level and was only intended to serve as a reference arrangement. Using this arrangement as a base, the shield, interstage and tank weights were combined for several variations of tank angle, separation distance and propellant

heating rates to determine the minimum incremental system weight increase required to prevent excessive propellant heating. The total system weight increase as a function of separation distance for several tank angles is shown in Figures 34 - 38.

Figure 34 shows the incremental weight needed to provide zero net positive suction head at the end of a 20 minute run for a shield which covers the core radius. Figure 35 shows similar data for a shield which covers the reflector radius. Both of these curves are for a tank heat input of 0.38 MW which requires a maximum tank pressure of 30 psia for the complete mixed case. Figure 36 illustrates total additional weights for the 30 psia tank pressure where the tank is completely shadowed by shields. The incremental weight increase for 0.12 MW heat input (representing a 20 psia tank pressure) and the reflector radius shield is shown in Figure 37. Figure 38 shows the weight increase required for a tank design pressure of 40 psia with shields having radii of 45 and 62 cm.

Increased tank pressures lead to higher total weights as shown in comparing Figures 35, 37, and 38. The incremental system weights shown on these curves were based on a 62 cm. radius shield, and a 20, 30 and 40 psia tank pressure respectively. The weight of the tank increases 2250 lbs from 20 to 40 psia while the weight of the shield and interstage decreases from 1800 to 300 lbs for the higher heating rates (0.12 MW at 20 psia to 0.58 MW at 40 psia). The savings in shield weight at higher tank pressure is insufficient to compensate for the increased tank weight. The tank design pressure therefore should be the minimum commensurate with structural requirements.

These curves also show that separation is preferred over decreasing tank angle as a method of reducing the heating rate. The change in tank angle from 37 1/2° to 25°

requires a 13 ft. increase in the interstage sleeve and reduces the heating rate to 1/2 of its original value. However, if the tank is moved 13 ft. farther from the core (at 37 1/2°), the heating rate is reduced more since much of the radiation absorbed in the periphery of the 25° cone will pass unattenuated through the elevated 37 1/2° tank. Thus, for the mixed heat distribution case separating the reactor from the tank is much more effective than reducing the tank angle.

In order to determine the optimum tank angle, the minimum system weights from Figures 17, 35, 36, 37, and 38 and calculated values for 45°, were combined as a function of tank angle (Figure 39). This figure shows that the minimum system weight occurs at a tank angle between 35° and 40° for all cases. It is therefore recommended that for preliminary designs a tank angle of 37 1/2° be used.

Of all the cases studied, the minimum incremental weight for an acceptable system occurs at 20 psia tank pressure and is found on Figure 37. This minimum system weight occurs at a tank angle of 37 1/2° with a 1175 lb. shield (16.9 cm. thick x 62 cm. radius) and a tank-core separation distance of 13.5 ft. In addition to producing the minimum system weight, this arrangement has more shielding than the 30 or 40 psia systems and could therefore afford more protection to the components and instruments above the engine.

If other reasons than investigated here dictate that the reactor to tank separation distance should be maintained at the minimum as dictated by components, of 8.45 ft, then the minimum over-all system weight would occur with a 30 psia tank pressure, a 37 1/2° tank angle and a 650 lb. shield which is 9.5 cm. thick and 62 cm. in radius. The penalty in maintaining the minimum separation distance is only 200 pounds in system weight.

4.0 SHIELD ELEMENT THERMAL DESIGN

4.1 PRELIMINARY NUCLEAR ANALYSIS OF SHIELD HEAT DEPOSITION

A preliminary analysis was performed to determine a gross estimate of the radiation heat deposition in the shield. The shield consisted of a right circular cylinder placed above the core support plate, 22.5 cm. thick, with a radius of 62 cm. The shield was assumed to be a homogeneous mixture of 63% lithium hydride, 27% stainless steel, and 10% void by volume.

Three important mechanisms of radiation heat deposition were investigated. The following is a description of these mechanisms and a presentation of the results.

1) Fast-Neutron Kinetic Heating

Fast neutrons are rapidly degraded in energy due to elastic scattering. Most of the energy deposited in this manner is transferred to the hydrogen atoms. At the incident face of the shield the heat deposition rate per unit volume of shield from neutron scattering is 1.25 watts/cm^3.

2) Core Gamma Heating

Gamma absorption due to the photoelectric and pair-production effects results in a complete transfer of energy. An additional transfer results from Compton scattering typified by a fractional energy loss per collision. Gamma heating is the chief mode of energy transfer in heavy elements where the photoelectric effect and pair production predominate. Thus, for the present shield, the stainless steel absorbs a large part of the gamma heat deposited. At the incident face of the shield the heat deposition rate due to gamma absorption is 10.9 watts/cm .

3) (n, α)Heating

For the shield material under consideration, an additional mode of heat transfer exists due to the $Li^6(n, \alpha) H^3$ reaction of lithium with a reaction energy, or Q value, of 4.784 Mev. This effect is by far the dominant mode of energy transfer in the front part of the shield, but is of decreasing relative significance deeper in the shield interior due to the rapid absorption of neutrons. At the incident face the heat deposition rate due to the (n, α) reaction is 44.5 watts/cm^3.

Figure 40 shows the variation in core-gamma, fast-neutron, (n, α) and total heat deposition rates throughout the shield. The total deposition rate was fitted by a sum of exponentials and is represented analytically by the equation:

$$W = (20.2)\, e^{-0.127\, d} + (23.2) e^{-0.342\, d} + (13.29)\, e^{-1.058\, d}$$

where W = watts/cm^3 and d is the distance from the incident face of the shield along the axis of symmetry.

Program 14-0 was used to compute the gamma ray heat deposition and fast neutron dose rates along the centerline axis of the shield. Neutron and (n, α) heating are based on a one-dimensional P1 analysis normalized to the fast neutron dose rate data at various distances in the shield.

It was assumed that these same heating rates persist along the entire shield radius extending to the pressure vessel inside wall. With this assumption, which tends to overestimate the heating, a shield 22.5 cm. thick would have about 2.8 MW of power deposited.

4.2 DESIGN CONFIGURATION INVESTIGATED

Five shield element geometries, schematically shown as configurations 1 through 5 on Figures 41 and 42, were analyzed to determine if they satisfy heat transfer and materials requirements for the heated bleed engine.

The heated bleed engine was selected for the original computations since it is the most critical from heat transfer considerations. In the heated bleed cycle, the nuclear radiation heating in the shield is removed by the turbine flow. For the NERVA engine this is about 4 lb/sec. With this relatively small amount of flow, the gas velocities through the shield are low, thus resulting in a lower gas side heat transfer coefficient and a higher bulk temperature than would be the case for the hot bleed cycle where all of the hydrogen for the reactor (70 lb/sec) passes through the shield.

Both flat plate and circular element geometries were considered for the shield. For each geometry the thermal analysis determines the maximum temperature which occurs in the lithium hydride at the plane of the shield facing the reactor. On this plane the heat generation is a maximum and is 0.9525 BTU/sec-in^3. This heating rate is based on the radiation heat deposition presented in Section 4.1, where the total heat deposited in the shield was calculated as 2.8 MW.

For this analysis a one-dimensional heat transfer cclculation was performed assuming the shield element consisted entirely of lithium hydride. The gas side heat transfer coefficient was taken to be equal to:

$$h_f = 0.036 \frac{k_f}{D} (Re)_f^{0.8} (Pr)_f^{0.4}$$

where h = convective heat transfer coefficient.

k = thermal conductivity of hydrogen.

D = hydraulic diameter.

Re = Reynolds number.

Pr = Prandtl number.

subscript f = properties evaluated at average (film) temperature between wall and bulk temperature.

Both a single pass and a double pass flow design as defined by Figure 43 were investigated for one of the cylindrical element geometries. It resulted that the single pass design was better from a heat transfer view point. Therefore, all consecutive analyses were done on the single pass design.

More detailed analyses were made on the shield geometry finally selected for the preliminary heated and hot bleed engines and are reported in Section 4.3.

4.2.1 FLAT PLATE GEOMETRY

The flat plate shield geometry is described in Figure 41, configuration 1. Each element consists of a Li H slab sandwiched between two stainless steel plates. The edges of the two plates may be welded together or to a common strip of steel. Either way, the Li H would be completely sealed within stainless steel. The shield elements are arranged parallel to the shield axis and spaced apart such that the void fraction is 10 per cent.

An analysis of this geometry was made and the results are contained in Figure 44 which shows the maximum temperature reached in the lithium hydride as a function of composite element thickness. This maximum temperature occurs in the plane of the shield immediately

above the reactor at the center of the Li H slab. The figure also shows the spacing between the elements, and the stainless steel cladding thickness as a function of element thickness which satisfies the nuclear radiation shield volumetric composition.

The maximum thickness of the shield element is determined by the maximum allowable Li H temperature. Since the melting temperature of Li H is 1724°R, and if 100R° margin is built into the design, it is found that a 0.9 inch thick element, with a corresponding maximum temperature of 1630°R, will be the maximum allowable thickness of the shield element. The minimum allowable thickness of the shield element is determined by the minimum allowable manufacturing spacing. A shield with a minimum spacing of 50 mils could be constructed by using wire as a spacer. This spacing would dictate a minimum element thickness of 0.45 inch. Therefore, as far as the heat transfer aspect of the shield design is concerned, the flat plate element thickness can be in the range between 0.45 inch and 0.90 inch.

The Li H slab can be made by either casting molten Li H in a high pressure hydrogen atmosphere or by compressing Li H powder. Casting of Li H presents a problem due to its high shrinkage upon solidification, but this difficulty can be overcome by using special casting techniques.

Compaction of Li H does not appear to present any major problems. Compaction can be done at room temperature but it is more feasible at elevated temperatures. At room temperature it is possible to compact Li H to density of 95% of the theoretical density by using a pressure of 85,000 psi, whereas by compressing Li H at a temperature of 1600°R, densities of 98% or better of theoretical density can be obtained at pressures of only 1,000 to 1,500 psi.

It is important to attain high Li H densities due to the fact that the thermal conductivity of Li H is very sensitive to changes in density in the 95% to 100% of theoretical density range. The thermal conductivity of Li H is also strongly dependent on its temperature. The value of thermal conductivity used in the shield calculations is 3.5 BTU/Hr - Ft-R^{o}, evaluated at 99% of theoretical density and 800^{o}R.

4.2.2 CYLINDRICAL GEOMETRIES

CONFIGURATION 2, FIGURE 41

In this design each shield element consists of Li H rods or pellets encased in stainless steel cylinders whose ends are capped and welded to seal the Li H. These capsules are arranged in a triangular array and are fixed by the bottom locating plate and the top support plate. If the shield is designed so that the capsules are touching, the per cent void is 9.2% for any capsule diameter; if the capsules are spaced so that they do not touch, the per-cent void will vary as a function of the spacing and diameter.

An analysis was performed at a power level of 2.8 MW with a maximum volumetric heating of 0.9525 BTU/sec - in^{3}. Results of this analysis are shown in Figures 45 and 46 for a single pass and double pass shield respectively. The variation of maximum temperature with the outside diameter of the capsule is illustrated. The parameter, per cent void, appearing on these curves depends on the spacing of the capsules.

With a cylindrical geometry such as this, it is best to design for as large a tube diameter as possible; this would minimize the number of tubes (number of tubes is inversely proportional to their diameter squared) and thereby decrease the cost of the shield and facilitate

its manufacturing and assembling. The maximum capsule diameter must not only be within the allowable limits dictated by the maximum allowable Li H temperature, but is must also be small enough so that it does not invalidate the assumption made for nuclear calculations that the shield is a homogeneous mixture.

CONFIGURATION 3, FIGURE 41

This shield concept could be made by using a block of steel and drilling holes into it in a triangular array. In these holes are placed encapsulated Li H cylinders which are smaller than the hole such that a cooling annulus remains around the Li H. In operation, coolant passes through the annulus to cool both the Li H and the steel structure. The annulus is designed such that the void is always 10%. Figure 47 shows the variation of maximum temperature at the center of the lithium hydride as a function of its diameter.

A drawback of this design is that in order to maintain the desired composition, the holes would have to be drilled rather close together leaving a very small amount of material between each hole to hold the structure together. This is in the range of 20 to 50 mils. Since the structure would experience thermal gradients, thermal transients, and imposed vibrations, the stainless steel between the holes may very well fail.

CONFIGURATION 4, FIGURE 42

This shield is made by using a block of stainless steel and drilling holes into it in a triangular array. These holes are then either filled with Li H pellets or filled with Li H powder which is then compacted in the block. The Li H is then sealed within these holes on both sides by welding a disk plate on the faces. In the center of the steel triangle formed by the Li H

filled holes, small holes are drilled which constitute a void per cent of 10%. These small holes are the coolant flow channel.

To analyze this configuration, it was assumed that steel has the same heat generation and the same thermal conductivity as Li H. This resulted in a structure consisting of Li H with coolant channels arranged in a hexagonal array. Then a symmetrical element was taken which consists of a 30° - 60° triangle with a circular segment removed at the 60° angle. The heat generated in this element would be conducted to the surface of the circular segment and removed by the coolant. The problem was to determine the variation of the maximum temperature, which exists at the vertex of the 30° angle, as a function of diameter of the coolant channel. Poisson's Equation was solved in cylindrical coordinates to get a general solution of the temperature field. Boundary conditions were applied for this problem to obtain the temperature at the 30° angle vertex. The results of this analysis are shown in Figure 48 where the maximum Li H temperature is plotted as a function of coolant channel diameter.

Since the prescribed composition (10% void, 27% steel, 63% Li H) must be maintained, there exist relationships between the coolant channel diameter and (1) the lithium hydride hole diameter, (2) the distance between the centers of the Li H chamber and coolant channel. The geometry was further investigated at a condition where the maximum Li H temperature is 1500°R. This corresponds to a coolant channel diameter of 0.120 inches, a Li H hole diameter of 0.428 inches, and a distance between the centers of these two of 0.296 inches. Therefore, the thickness of the stainless steel which separates these two holes on their centerline will be 22 mils. The minimum spacing permissible between two holes when drilling

into 12 inches of stainless steel is about 20 mils. Thus it would appear that a coolant channel diameter of about 0.12 inches is the only one practical. Smaller channel diameters would present manufacturing difficulties and larger channel diameters would result in excessive lithium hydride temperatures.

CONFIGURATION 5, FIGURE 42

This design consists of tubes embedded in a lithium hydride block in a triangular array. The lithium hydride would be completely sealed within a stainless steel housing. The inside of the tubes form the coolant channels. The maximum temperature occurs at the center of the triangles formed by the tubes; its variation with inside tube diameter is shown in Figure 49. The geometry was analyzed by simulating it by an equivalent concentric cylinder of lithium hydride around the stainless steel tube. One drawback of this design is that pressure buildup in the Li H chamber would be harder to contain than in small cylindrical elements.

4.3 DETAILED ANALYSES OF SELECTED SHIELD DESIGN

From overall heat transfer, manufacturing, materials, and strength considerations, shield configuration 2, of Figure 41, was selected as the most desirable for the flight engine. The predominant reason for selecting this particular array was manufacturing and processing considerations, since this method of manufacturing has been used in fuel element design in the past. The final shield geometry was modified as shown in Figure 42, configuration 6.

4.3.1 NUCLEAR ANALYSIS OF RADIATION HEAT DEPOSITION

A more detailed analysis was performed to estimate the radiation heat generation in the shield design of configuration 6.

A precise description of the geometry included the latest design of the aluminum top support plate, the stainless steel shield plenum and structure, and a one inch thick aluminum pressure vessel. The shield material was considered a homogeneous mixture of 63% lithium hydride, 27% stainless steel, and 10% void by volume. The shield thickness at the centerline was 31.4 cm. This shield is commensurate with a 90% overall reduction in propellant heating for a 37.5° tank angle.

The same three mechanisms of radiation heat deposition discussed in Section 4.1 were investigated in the shield, namely, fast neutron kinetic, core gamma, and n,α heating. In addition, the heating due to thermal neutron capture (n,γ heating) in the steel at the front face of the shield was estimated.

Program 14-0 was used to compute the core gamma ray heating, and fast neutron dose rates, along three axial traverses located at radii of 0, 22.5295, and 45.059 cm. A one-dimensional P1 analysis was made at the centerline (radius = 0 cm.). The neutron and n,α heating were obtained at each traverse by normalizing the P1 data to the fast neutron dose rate computed at each detector location. The n, γ heating in the steel was determined by hand calculations, and is also based on the P1 approximation of the thermal flux. Figures 50 thru 52 show the variation in core-gamma, fast neutron, n,α, and total heat deposition rates throughout the shield at each radial traverse. Also, shown in these graphs is the heat deposition rates in the steel and aluminum.

From these data the total heat deposition was calculated to be 2.1 MW, of which about 0.35 MW is deposited in the steel nearest the reactor core. The radiation heating rate

data presented here are subject to change pending a better method of calculating the thermal and fast neutron flux levels.

The localized increase in heating on the front face of the shield due to gamma rays and neutrons streaming through the holes in the support plate was estimated. It was assumed that the unscattered flux streaming through a hole is proportional to $(\frac{r}{L})^2$ where r is the radius and L is the length of the hole. If the core is assumed to be a self-absorbing homogeneous source, the uncollided flux, ϕ, at the upper edge of the support plate due to an emergent flux, ϕ_o, from the core is $\phi = \phi_o (\frac{r}{L})^2$. This equation is applicable to both neutron and gamma fluxes. The effect of single-scattering was estimated and found to be negligible in comparison with the direct beaming effect.

The results of these calculations indicate that there will be a 7% local increase in heating on the front face of the shield at a point directly over a hole in the support plate.

4.3.2 DETAILED THERMAL ANALYSIS

The thermal analysis of the modified shield schematically shown as configuration 6 on Figure 42 includes several factors not considered in the previous analysis of configuration 2. These factors include the following:

1) The non-symmetrical temperature field that occurs because the tubes may be in contact which will decrease the effective surface area for heat convection. To compensate for this, it was assumed that the effective convective area was 2/3 of the tube surface.

2) The total heat flux. The total heat flux considered in this analysis was doubled due to uncertainties involved in the nuclear analysis techniques described in Section 4.3.1.

3) Non-uniform flow. As the fluid flows radially in the plenum chamber below the shield, it will cause a variation in the fluid static pressure. This will effect a non-uniform axial flow distribution through the shield. Thus, the flow rate in some channels will be much less than that used to calculate the convective film coefficient. In effect, this will increase the temperature drop through the film thereby increasing the maximum temperature at the center of the lithium hydride. To correct the maldistribution of fluid, it was decided to incorporate an orificing arrangement either downstream or upstream of the shield in order to cause a relatively high flow controlling pressure drop compared to that through the coolant channels. In this analysis, then, it was assumed that the local mass flow through the channels could be as low as 90% of the nominal.

4) Tube Clearance. Since the lithium hydride pellets are manufactured separately and then are placed in the tubes, there must be clearance between the pellets and the tubes. Manufacturing tolerances are such that the maximum clearance will be 4 mils when the pellets are concentric within the tubes. This gap will be filled with helium. These preliminary calculations assumed that the heat generated in the lithium hydride will be conducted through this helium film. The temperature drop through this film, which will tend to increas the maximum temperature at the center of the lithium hydride, was not considered in previous calculations.

5) Cracking of Li H. Thermal gradients which cause internal stresses and vibration shocks may crack the lithium hydride which will in effect decrease its density and, therefore, its thermal conductivity. Since the initial empty space within the capsules is limited, it is not believed that the pellets would shatter completely to a powder. Since no data is available

to relate thermal conductivity of lithium hydride with its relative density, it was assumed that cracking of the lithium hydride would effect an increase of 10% in the temperature drop.

4.3.2.1 HEATED BLEED CYCLE

The variation in the lithium hydride maximum temperature at the front plane of the shield with outside tube diameter was first evaluated for the heated bleed engine in which only the turbine drive fluid passes through the shield. Figure 53 shows this relationship. The maximum heat flux used in this calculation was 0.60 BTU/sec - in^3 compared with 0.9525 BTU/sec - in^3 used in previous calculations. This value of maximum heat flux was the result of recent changes in overall shield design, thus producing a total power absorbed in the shield of 2.1 MW rather than the 2.79 MW value used previously in the thermal calculations (see Section 4.3.1). Figure 53 shows that the maximum allowable capsule diameter is 0.83 inches, which is dictated by the melting temperature of Li H.

At this point a fixed capsule diameter of 0.5 inches was chosen with a corresponding maximum temperature of 1000°R so that additional detailed thermal and mechanical analyses could be made on the heated bleed shield design. A 1000°R maximum temperature was considered a realistic design value for the lithium hydride, and a 0.5 inch diameter capsule realistic for shield manufacturing. With this diameter and a heating rate of 0.60 BTU/sec - in^3, the axial maximum temperature distribution in the pellets was calculated for the heated bleed engine, and the results are shown in Figure 54.

4.3.2.2 HOT BLEED CYCLE

In a similar manner, the axial maximum temperature distribution in the lithium

hydride pellets for the hot bleed engine shield was calculated and the results are reported in Figure 55.

The difference in temperatures shown in Figure 54 and 55 is the result of a difference in the coolant flow path and flow rate in the heated bleed and hot bleed shields. The heated bleed engine cycle requires one pass cooling through the shield at a flow rate of 4.5 lb/sec; the hot bleed engine cycle requires two pass shield cooling at a flow rate of about 70 lb/sec. These two differences affect both the bulk temperature and the convective film coefficient which account for the differences in the axial maximum temperature distributions.

5.0 RADIATION LEVELS AFTER OPERATION

The radiation levels of the NERVA reactor components after power operation at 1120 MW were calculated. These values will be used to determine the shielding requirements for the E-MAD building and the radiation levels in the vicinity of the test stand. The sources considered were fission products, materials in the core, and activiation of the various components such as the core support plate, thermal shield, reflector, control drums, vessel, and nozzle. These values were determined for one 20 minute run and three equally spaced 20 minute runs in 30 days.

5.1 CORE SOURCES

The fission product activity in the core after the above operating conditions was determined for both 1000 seconds and 24 hours decay. The source values were obtained from Reference 8, which gives the gamma energy spectrum from U^{235} fission products in seven groups as a function of operating time and time after shutdown. For this study, the energies were combined into three groups. The ranges of these groups and the NERVA sources (S_v) after 24 hours are as follows:

Group	Energy (Eγ)	Energy Range	S_v (NERVA)
1	0.8 Mev	0 - 0.9 Mev	8.1×10^{10} mev/cm^3 - sec
2	1.5	0.9 - 1.8	2.0×10^{10}
3	2.5	$\geq$ 1.8	1.4×10^{10}

The grouping was made by assuming that all the energy emitted in the specified energy range is due to photons of energy Eγ. This assumption tends to overestimate the dose rates and shield requirements.

These sources were converted to dose rates at the surface of the core by the relations:

$$\phi = 1/2\ Sv\ \lambda$$

$$DR = \phi\ K\ (E\gamma),$$

where

λ is the relaxation length for the given radiation within the volume source ($= 1/\mu_s\ cm^{-1}$),

Sv is the volume source strength ($mev / cm^3 - sec$),

ϕ is the flux leaving the surface in the outward direction ($mev / cm^2 - sec$),

$K(E\gamma)$ is a flux to dose conversion factor and is a function of photon energy $\frac{R/hr}{mev/cm^2 - sec}$,

DR is the dose rate (R/hr).

In order that the E-MAD building be designed to handle reactors operated at 4000 MW, the NERVA levels could be ratioed by 4000/1120 and used for design.

The study included the activity induced in the core coolant channel cladding. It is planned to use niobium for this purpose. This activity contributes less than 1/2% to the fission product activity 24 hours after shutdown.

5.2 ACTIVATION

The radiation induced activity level of various impurities and constituents of the materials used in the reactor and engine components was determined for the following conditions:

a) 20 minute operation - 1000 second decay

b) 20 minute operation - 24 hour decay

c) three 20 minute runs equally spaced in thirty days - 24 hour decay after the third run.

The resulting decay gammas were combined into three energy groups, 0.8, 1.3, and 2 Mev. Data for the above conditions were obtained by hand calculations.

Data for condition "b" was later computed for a decay range of 0 to 10^5 minutes using a Fortran program coded for an IBM 7090 digital computer. This code calculates the gamma build-up and decay activity for each individual daughter of each constituent (up to three daughters), sub-totals the activity for each constituent, and finally gives the total activity. This data is calculated on a logarithmic time scale. These activities in conjunction with the energy spectra, and yields, were used to give the source strengths in mev/cm^3 sec. for various reactor components. Figures 56 through 58 show the results of these calculations for aluminum, niobium, and inconel. Similar data are being compiled for beryllium and graphite.

Table 33 lists for the various engine components, the materials, and their significant impurities considered after 1000 seconds operation and 24 hours decay.

The method used in the hand calculation of the source strengths $S_v(E)$, mev/cm^3-sec is as follows:

$$S_v(E) = \phi_n \Sigma_{act} F_{sat} E\gamma \gamma(E)$$

where

ϕ_n = neutron flux for the proper fast or thermal group considered, n/cm^2 - sec.

Σ_{act} = macroscopic activation cross section, cm^{-1}

F_{sat} = saturation fraction

= $(1 - e^{-\lambda t})\ (e^{-\lambda t})$

= $f_{growth} \times f_{decay}$

$E\gamma$ = energy, Mev, of photons given off

$\nu(E)$ = fractional yield, number of gamma of each energy level given off

It was assumed that $\Sigma_{act} = \rho\ N_o\ f\sigma_{act}$

where

ρ = material density, gms/cm^3

N_o = number density of material, atoms/gm of pure material

f = fractional abundance in natural material times fractional abundance in alloy

σ_{act} = microscopic activation cross section[9, 10] of material, cm^2

This procedure was carried out for each reaction under consideration, and the total source strength was obtained by summing up the contributions of each reaction into three energy groups.

For example, consider stainless steel (18-8):

Reaction: $Fe^{58}(n,\gamma)\ Fe^{59}$ $\qquad T_{1/2}(Fe^{59}) = 45$ days

$$N_o = 0.0108 \times 10^{24} \ \frac{\text{Atoms}}{\text{Gram of Pure Iron}}$$

$$f^1 = (f_{natural} \times f_{alloy}) = (0.003 \times 0.670) = 0.00201$$

$$\sigma_{thermal} = 0.900 \text{ barns} = 0.90 \times 10^{-24} \text{ cms.}^2$$

$$\rho = 7.9 \text{ grams/cm}^3$$

$$\Sigma = \rho N_o f \sigma = \left(7.9 \frac{\text{grams - iron}}{\text{cm}^3}\right) \left(.0108 \times 10^{24} \frac{\text{atoms of pure iron}}{\text{gram of pure iron}}\right)$$

$$\left(0.00201 \frac{\text{atoms of isotopes}}{\text{atoms of pure iron}}\right) \times \left(0.900 \times 10^{-24} \text{ cms}^2\right)$$

$$= .000154 \ \frac{1}{\text{cms}} = 1.54 \times 10^{-4} \text{ cms}^{-1}$$

$E\gamma$, Mev	Fractional Abundance ν (E)	$E\gamma\ \nu$ (E)
1.1	(0.56)	0.6160
1.4	(0.44)	0.6160
Total		1.2320

$$\phi_n = 1.9 \times 10^{15} \frac{\text{neutrons}}{\text{cm}^2 - \text{sec}}$$

$$\Sigma_{act} = 1.54 \times 10^{-4} \text{ cms}^{-1}$$

$$F_{sat} = F_{growth\ (20\ minutes)} \times F_{decay\ (24\ hours)} = 4.9 \times 10^{-4}$$

$$\sum^{E} [E_\gamma][\nu(E)] = 1.232 \frac{\text{Mev}}{\text{neutron}}$$

$$S_v(E) = (1.9 \times 10^{15} \frac{\text{neutrons}}{\text{cm}^2\ \text{sec}}) (\frac{1.54 \times 10^{-4}}{\text{cm}}) (4.9 \times 10^{-4}) (\frac{1.232\ \text{Mev}}{\text{neutron}})$$

$$= 17.6637 \times 10^{7} \frac{\text{Mev}}{\text{cm}^3 - \text{sec}} = 1.7663 \times 10^{8} \frac{\text{Mev}}{\text{cm}^3 - \text{sec}}$$

The source strengths for each material for three energy groups are listed in Table 34. The scandium (Sc^{46}) activity included in the table for beryllium accounts for less than 4% of the activation activity at 24 hours. Because of its relatively long half life (84 days), this isotope may be important after the decay of such short half life isotopes as 2.6 hour Ni and Mn and 15 hour Na.

TABLE I

GAMMA RAY FLUX LEVELS AROUND AN UNSHIELDED KIWI B-1 CORE

(Mev/cm^2 - sec x 10^{-12}) (Distance From Center of Core to Detector - 5 ft.)

Operating Time: 20 min Operating Power: 1120 MW

	Angle, α, Degrees					
Eγ - Mev	0	15	30	45	60	75
0.3	11.23	9.12	6.53	5.31	8.63	7.70
0.7	46.7	38.95	27.50	20.47	29.92	32.07
1.0	40.1	38.62	24.11	18.26	25.69	27.93
1.5	36.83	31.12	23.11	18.12	24.44	26.88
2.0	30.67	26.14	19.94	16.11	21.14	23.29
2.5	25.84	22.12	17.27	14.09	18.16	19.97
2.8	16.85	14.50	11.39	15.00	19.22	21.10
3.5	45.55	39.39	31.59	25.81	32.50	35.53
4.5	20.44	17.77	14.65	12.38	15.37	16.70
5.5	7.58	6.63	5.55	4.44	5.45	5.89
6.5	2.04	1.93	1.53	.89	1.09	1.17
7.5	.506	.45	.38	.35	.43	.46
9.0	.09	.08	.07	.07	.08	.09
Total	284.43	246.82	183.62	151.30	202.12	218.78

90	105	120	135	150	165	180
8.29	6.87	5.19	3.54	8.91	12.31	14.19
33.88	29.13	21.68	17.19	35.46	48.49	55.55
29.34	25.50	19.18	15.57	35.18	40.71	46.74
28.02	24.70	18.93	15.39	26.80	35.50	40.54
24.14	21.50	16.77	13.64	21.97	28.54	32.51
20.63	18.50	14.65	11.91	18.42	23.62	26.68
21.75	19.58	15.62	12.72	12.09	15.36	17.35
36.48	33.08	26.80	21.88	32.62	40.72	45.69
17.08	15.59	12.83	10.50	14.78	18.07	20.24
6.01	5.51	4.58	3.75	5.51	6.56	7.33
1.20	1.10	.92	.75	1.48	1.75	1.95
.47	.43	.36	.30	.37	.43	.48
.09	.08	.07	.06	.07	.08	.09
227.38	201.57	157.58	127.20	213.66	272.13	309.34

TABLE 2

GAMMA RAY FLUX LEVELS AROUND AN UNSHIELDED KIWI B-1 CORE

(Mev/cm^2 - sec x 10^{-11}) (Distance From Center of Core to Detector - 10 ft.)

Operating Time: 20 min Operating Power: 1120 MW

	Angle, α, Degrees					
Eγ - Mev	0	15	30	45	60	75
0.3	20.08	17.18	13.79	12.481	16.507	26.430
0.7	85.31	73.28	59.77	51.174	65.110	90.178
1.0	73.92	63.84	52.64	45.838	57.228	76.420
1.5	68.83	60.07	50.67	45.591	55.861	71.133
2.0	58.04	50.93	43.82	40.470	48.968	60.485
2.5	48.63	42.88	37.50	35.279	42.362	51.326
2.8	50.31	44.46	39.39	37.472	44.915	53.975
3.5	82.98	73.97	66.61	64.230	76.324	91.108
4.5	37.98	34.13	31.15	30.660	36.173	42.065
5.5	13.28	11.95	11.09	10.964	12.844	14.787
6.5	2.59	2.34	2.21	2.196	2.570	2.944
7.5	1.0	.91	.86	.863	1.007	1.146
9.0	.18	.17	.16	.163	.190	.215
Total	543.13	476.11	409.66	377.381	460.059	582.212

90	105	120	135	150	165	180
20.035	19.258	9.717	9.553	18.15	22.75	25.41
81.710	76.516	39.774	51.410	63.12	91.02	103.29
70.825	66.215	34.837	46.151	62.61	77.61	88.07
67.673	63.250	33.791	44.916	56.52	68.83	77.85
58.338	54.639	29.506	39.257	47.12	56.13	63.37
49.870	46.822	25.470	33.915	46.38	55.25	51.88
52.614	49.463	27.003	36.016	41.15	47.97	53.63
88.314	83.264	45.776	61.286	67.71	77.83	77.46
41.377	39.135	21.649	29.089	31.33	35.18	39.03
14.568	13.809	7.668	10.327	10.95	12.12	13.37
2.901	2.755	1.532	2.061	2.15	2.35	2.57
1.131	1.075	.600	.810	.84	.91	.99
.213	.203	.113	.154	.16	.17	.18
549.669	516.404	277.436	364.945	448.19	548.12	597.10

Astronuclear

TABLE 3

GAMMA RAY FLUX LEVELS AROUND AN UNSHIELDED KIWI B-1 CORE

(Mev/cm^2 - sec x 10^{-11}) (Distance From Center of Core to Detector - 20 ft.)

Operating Time: 20 min Operating Power: 1120 MW

	Angle, α, Degrees					
Eγ - Mev	0	15	30	45	60	75
0.3	4.22	3.75	3.22	3.79	4.01	5.41
0.7	18.11	16.10	14.00	15.70	16.24	20.21
1.0	15.70	14.10	12.40	14.04	14.29	17.37
1.5	14.80	13.30	11.90	13.84	13.95	16.46
2.0	12.60	11.40	10.40	12.20	12.36	14.15
2.5	10.60	9.62	8.95	10.58	10.55	12.08
2.8	11.00	10.00	9.43	11.20	11.18	12.73
3.5	18.00	16.80	15.90	19.12	18.97	21.37
4.5	8.43	7.78	7.55	9.09	8.97	10.02
5.5	2.95	2.74	2.69	3.24	3.18	3.53
6.5	.57	.53	.53	.64	.64	.70
7.5	.22	.21	.20	.25	.25	.27
9.0	.04	.03	.03	.04	.05	.05
Total	117.24	106.36	97.20	113.73	114.64	134.35

90	105	120	135	150	165	180
4.81	4.73	3.41	3.21	4.19	4.86	5.47
19.74	18.81	15.46	17.23	17.00	19.80	22.30
17.14	16.29	13.75	15.27	14.70	16.90	19.10
16.43	15.57	13.45	14.53	13.40	15.20	17.10
14.19	13.46	11.78	12.50	11.30	12.60	14.00
12.14	11.54	10.18	10.69	9.48	10.40	11.50
12.82	12.20	10.80	11.30	9.95	10.80	12.10
21.55	20.55	18 34	19.07	16.60	17.70	19.60
10.11	9.66	8.68	8.98	7.71	8.09	8.88
3.56	3.41	3.07	3.17	2.70	2.79	3.05
.71	.68	.61	.63	.53	.54	.59
.27	.26	.24	.25	.20	.21	.22
.05	.05	.04	.05	.03	.03	.04
133.53	127.21	109.81	116.88	107.81	119.94	133.96

Astronuclear

TABLE 4

GAMMA RAY DOSE RATE LEVELS AROUND AN UNSHIELDED KIWI B-1 CORE

(Rads/sec x 10^{-3}) (Distance From Center of Core to Detector - 5 ft.)

Operating Time: 20 min Operating Power: 1120 MW

	Angle, α, Degrees					
Eγ - Mev	0	15	30	45	60	75
0.3	8.09	6.57	4.70	3.82	6.21	5.54
0.7	34.00	28.36	20.02	14.90	21.78	23.34
1.0	27.90	26.88	16.78	12.71	17.88	19.44
1.5	23.53	19.89	14.77	11.58	15.62	17.18
2.0	18.40	15.62	11.96	9.67	12.68	13.97
2.5	14.47	12.39	9.63	7.89	10.17	11.18
2.8	9.10	7.83	6.15	8.10	10.38	11.39
3.5	22.96	19.85	15.92	13.01	16.38	17.91
4.5	9.65	8.39	6.91	5.84	7.25	7.88
5.5	3.27	2.86	2.40	1.92	2.35	2.54
6.5	.83	.78	.62	.36	.44	.47
7.5	.20	.18	.15	.14	.17	.18
9.0	---	---	---	.03	.03	.03
Total	172.40	149.66	110.01	89.97	121.34	131.05

90	105	120	135	150	165	180
5.97	4.95	3.74	2.55	2	8.86	10.22
24.66	21.21	15.78	12.5'	25.81	35.29	40.44
20.42	17.75	13.35	10.64	24.49	28.33	32.53
17.90	15.78	12.10	9.83	17.13	22.68	25.91
14.48	12.90	10.06	8.18	13.18	17.12	19.51
11.55	10.36	8.20	6.67	10.31	13.23	14.94
11.74	10.57	8.43	6.87	6.53	8.29	9.37
18.39	16.67	13.51	11.03	16.44	20.52	23.03
8.06	7.36	6.06	4.96	6.98	8.53	9.55
2.60	2.38	1.98	1.62	2.38	2.83	3.17
.49	.44	.37	.30	.60	.71	.79
.18	.17	.14	.12	.14	.17	.19
.03	.03	.03	.02	--	--	--
136.47	120.57	93.75	75.50	130.41	166.56	189.65

Astronuclear

TABLE 5

GAMMA RAY DOSE RATE LEVELS AROUND AN UNSHIELDED KIWI B-1 CORE

(Rads/sec x 10^{-3}) (Distance From Center of Core to Detector - 10 ft.)

Operating Time: 20 min Operating Power: 1120 MW

	Angle, α, Degrees					
Eγ - Mev	0	15	30	45	60	75
0.3	1.45	1.24	.99	.90	1.19	1.90
0.7	6.19	5.33	4.35	3.72	4.74	5.66
1.0	5.14	4.44	3.66	3.19	3.98	5.32
1.5	4.40	3.84	3.24	2.91	3.57	4.54
2.0	3.48	3.01	2.63	2.43	2.94	3.63
2.5	2.72	2.40	2.10	1.98	2.37	2.87
2.8	2.72	2.40	2.13	2.02	2.42	2.91
3.5	4.18	3.73	3.36	3.24	3.85	4.59
4.5	1.79	1.61	1.47	1.45	1.71	1.69
5.5	.57	.52	.49	.47	.55	.64
6.5	.10	.09	.09	.09	.10	.12
7.5	----	----	----	.03	.04	.04
9.0	----	----	----	.01	.01	.01
Total	32.74	28.61	24.51	22.44	27.47	33.92

90	105	120	135	150	165	180
1.44	1.39	.70	.69	1.31	1.64	1.83
5.95	5.57	2.89	3.74	4.60	6.63	7.53
4.93	4.61	2.42	3.21	4.36	5.40	6.13
4.32	4.04	2.16	2.87	3.61	4.40	4.97
3.50	3.28	1.77	2.35	2.83	3.37	3.80
2.79	2.62	1.43	1.90	2.60	3.09	2.91
2.84	2.67	1.46	1.94	2.22	2.59	2.90
4.45	4.20	2.31	3.09	3.41	3.92	3.90
1.95	1.85	1.02	1.37	1.48	1.66	1.84
.63	.60	.33	.45	.47	.52	.57
`2	.11	.06	.08	.09	.10	.10
. 4	.04	.02	.03	----	----	----
.01	.01	----	.01	----	----	----
32.97	30.99	16.57	21.33	26.98	33.32	36.48

TABLE 6

GAMMA RAY DOSE RATE LEVELS AROUND AN UNSHIELDED KIWI B-1 CORE

(Rads/sec x 10^{-3}) (Distance From Center of Core to Detector - 20 ft.)

Operating Time: 20 min Operating Power: 1120 MW

	Angle, α, Degrees					
Eγ - Mev	0	15	30	45	60	75
0.3	.30	.27	.23	.27	.29	.39
0.7	1.32	1.17	1.02	1.14	1.18	1.47
1.0	1.09	.98	.86	.98	.99	1.21
1.5	.95	.85	.76	.88	.89	1.05
2.0	.76	.68	.62	.73	.74	.85
2.5	.59	.54	.50	.59	.59	.68
2.8	.59	.54	.51	.60	.60	.69
3.5	.92	.85	.80	.96	1.78	1.08
4.5	.39	.37	.36	.43	.42	.47
5.5	.13	.12	.12	.14	.14	.15
6.5	.02	.02	.02	.03	.03	.03
7.5	.01	.01	.01	.01	.01	.01
9.0	---	---	---	---	---	---
Total	7.07	6.40	5.81	6.76	7.66	8.08

90	105	120	135	150	165	180
.35	.34	.24	.23	.30	.35	.39
1.44	1.37	1.12	1.25	1.24	1.44	1.62
1.19	1.13	.96	1.06	1.02	1.18	1.33
1.05	.99	.86	.93	.86	.97	1.09
.85	.81	.71	.75	.68	.76	.84
.68	.65	.57	.60	.53	.58	.64
.69	.66	.58	.61	.54	.58	.65
1.09	1.04	.92	.96	.84	.89	.99
.48	.46	.41	.42	.36	.38	.42
.15	.15	.13	.14	.12	.12	.13
.03	.03	.02	.02	.02	.02	.02
.01	.01	.01	.01	.01	.01	.01
---	---	---	---	---	---	---
8.01	7.64	6.53	6.98	6.52	7.28	8.13

TABLE 7

FAST NEUTRON DOSE RATE LEVELS AROUND AN UNSHIELDED KIWI B-1 CORE

Rads (ethylene) / Sec

Operating Time: 20 min Operating Power: 1120 MW

Angle, α, Degrees

Distance, Feet	0	15	30	45	60
5	1.62×10^5	1.38×10^5	9.68×10^4	5.08×10^4	4.65×10^4
10	3.01×10^4	2.61×10^4	2.00×10^4	1.32×10^4	1.08×10^4
20	6.45×10^3	5.69×10^3	4.57×10^3	4.74×10^3	2.84×10^3

Angle, α, Degrees

Distance, Feet	75	90	105	120	135
5	4.23×10^4	4.49×10^4	3.83×10^4	3.35×10^4	4.49×10^4
10	1.37×10^4	1.10×10^4	1.12×10^4	6.01×10^3	1.31×10^4
20	3.01×10^3	2.69×10^3	2.78×10^3	2.69×10^3	4.85×10^3

Angle, α, Degrees

Distance, Feet	150	165	180
5	1.09×10^5	1.52×10^5	1.76×10^5
10	2.17×10^4	2.90×10^4	3.33×10^4
20	4.94×10^3	6.33×10^3	7.22×10^3

TABLE 8

TOTAL DOSE RATE LEVELS AROUND AN UNSHIELDED KIWI B-1 CORE

Rads (ethylene) / Sec

Operating Time: 20 min Operating Power: 1120 MW

Angle, α, Degrees

Distance, Feet	0	15	30	45	60
5	3.34×10^5	2.92×10^5	2.07×10^5	1.41×10^5	1.66×10^5
10	6.88×10^4	5.47×10^4	4.45×10^4	3.50×10^4	3.80×10^4
20	1.35×10^4	1.21×10^4	1.04×10^4	1.14×10^4	1.05×10^4

Angle, α, Degrees

Distance, Feet	75	90	105	120	135
5	1.72×10^5	1.85×10^5	1.58×10^5	1.26×10^5	1.20×10^5
10	4.80×10^4	4.40×10^4	4.20×10^4	2.30×10^4	3.40×10^4
20	1.11×10^4	1.07×10^4	1.04×10^4	9.20×10^3	1.21×10^4

Angle, α, Degrees

Distance, Feet	150	165	180
5	2.39×10^5	3.18×10^5	3.65×10^5
10	4.86×10^4	6.24×10^4	6.98×10^4
20	1.15×10^4	1.36×10^4	1.54×10^4

TABLE 9

TOTAL FAST NEUTRON FLUX LEVELS AT SEVERAL DISTANCES FROM CENTER OF UNSHIELDED KIWI B-1 CORE

REACTOR POWER: 1120 MW

Distance, Feet	Total Fast Neutron Flux, N/Cm^2 - Sec		
	$\alpha = 0^\circ$	$\alpha = 90^\circ$	$\alpha = 180^\circ$
5	8.257×10^{13}	2.89×10^{13}	7.023×10^{13}
10	1.534×10^{13}	7.06×10^{12}	1.265×10^{13}
20	3.287×10^{12}	1.73×10^{12}	2.744×10^{12}

TABLE 10

THERMAL NEUTRON FLUX LEVELS AT SEVERAL DISTANCES FROM CENTER OF THE UNSHIELDED KIWI B-1 CORE

REACTOR POWER: 1120 MW

Distance, Feet	Thermal Neutron Flux, N/Cm^2 - Sec		
	$\alpha = 0^\circ$	$\alpha = 90^\circ$	$\alpha = 180^\circ$
5	2.038×10^{13}	5.984×10^{13}	1.489×10^{12}
10	3.786×10^{12}	1.455×10^{13}	2.818×10^{11}
20	8.114×10^{11}	3.573×10^{12}	6.108×10^{10}

TABLE 11

FAST NEUTRON FLUXES OUTSIDE AN UNSHIELDED KIWI B-1 CORE

(Neutrons/cm^2 - sec.) (Distance From Center of Core to Detector, 5 feet)

Operating Time: 20 min Operating Power: 1120 MW

Neutron Energy Group	$a = 0^\circ$	$a = 90^\circ$	$a = 180^\circ$
6.07 - 10 Mev	3.823×10^{11}	0.571×10^{11}	5.410×10^{11}
3.68 - 6.07	21.872	2.623	25.160
2.23 - 3.68	50.636	5.365	58.144
1.35 - 2.23	110.691	44.681	137.915
.821 - 1.35	107.485	30.609	114.112
.498 - .821	101.347	25.803	115.203
.302 - .498	48.218	22.845	53.186
.183 - .302	4.096	0.794	3.216
.111 - .183	14.326	1.982	8.246
.0674 - .111	8.551	1.382	5.285
.0248 - .0674	15.032	3.133	10.917
.00912 - .0248	4.382	1.045	3.216
.00335 - .00912	4.813	1.143	3.275
.00123 - .00335	44.613	12.759	34.447
454 - 1230 ev	42.296	14.256	31.546
167 - 454	41.212	15.229	27.576
101 - 167	22.691	8.909	13.418
61.3 - 101	22.064	9.021	11.863
37.2 - 61.3	21.416	9.165	9.030
22.6 - 37.2	20.611	9.270	7.567
13.7 - 22.6	22.213	10.645	5.476
8.32 - 13.7	18.524	9.499	4.577
5.1 - 8.32	16.997	9.169	4.285
3.06 - 5.1	16.299	9.796	3.726
1.86 - 3.06	14.651	9.583	3.035
1.125 - 1.86	13.416	9.664	2.737
.625 - 1.125	13.457	10.923	----
Total	825.735×10^{11}	289.864×10^{11}	702.568×10^{11}

TABLE 12

GAMMA RAY FLUX LEVELS ONE FOOT FROM THE SURFACE OF THE PRESSURE VESSEL AND NOZZLE END OF THE UNSHIELDED CORE

Mev/cm^2 - sec x 10^{-13}
Angle, α, Degrees

Operating Time: 20 min
Operating Power: 1120 MW

Eγ, Mev	0°	25°	54°	90°
0.3	1.072	.709	.853	2.028
0.7	4.593	3.208	3.923	8.373
1.0	3.962	2.806	3.498	7.236
1.5	3.651	2.644	3.447	6.819
2.0	3.033	2.231	3.045	5.832
2.5	2.571	1.912	2.703	5.057
2.8	1.973	1.475	2.139	3.955
3.5	3.375	2.551	3.838	6.930
4.5	1.563	1.193	1.871	3.302
5.5	.545	.419	.669	1.164
6.5	.151	.117	.192	.331
7.5	.058	.045	.075	.129
9.0	.009	.007	.012	.020
Total	26.556	19.317	26.265	51.176

Eγ, Mev	126°	162°	180°
0.3	.597	2.089	3.518
0.7	2.881	8.774	14.572
1.0	2.606	7.425	12.217
1.5	2.621	6.503	10.492
2.0	2.349	5.229	8.311
2.5	2.108	4.333	6.812
2.8	1.677	3.325	5.196
3.5	3.041	5.589	8.630
4.5	1.497	2.549	3.891
5.5	.539	.872	1.320
6.5	.155	.239	.361
7.5	.061	.092	.138
9.0	.009	.015	.022
Total	20.141	47.034	75.480

Astronuclear

TABLE 13

GAMMA RAY DOSE RATE LEVELS ONE FOOT FROM THE SURFACE OF THE PRESSURE VESSEL AND NOZZLE-END OF THE UNSHIELDED CORE

Rads/sec x 10^{-3}
Angle, α, Degrees

Operating Time: 20 min
Operating Power: 1120 MW

Eγ, Mev	0°	25°	54°	90°
0.3	7.718	5.105	6.142	14.602
0.7	33.437	23.354	28.559	60.955
1.0	27.576	19.529	24.346	50.363
1.5	23.329	16.895	22.026	43.573
2.0	18.198	13.386	18.270	34.992
2.5	14.398	10.707	15.137	28.319
2.8	10.654	7.965	11.551	21.357
3.5	17.010	12.857	19.343	34.927
4.5	7.377	5.631	8.831	15.585
5.5	2.354	1.810	2.890	5.028
6.5	.235	.474	.778	1.341
7.5	.226	.176	.293	.503
9.0	.034	.027	.046	.076
Total	162.546	117.916	158.212	311.621

Eγ, Mev	126°	162°	180°
0.3	4.298	15.041	25.329
0.7	20.974	63.875	106.084
1.0	18.138	51.678	85.030
1.5	16.748	41.554	67.044
2.0	14.094	31.374	49.866
2.5	11.805	24.265	38.147
2.8	9.056	17.955	28.058
3.5	15.327	28.169	43.495
4.5	7.658	12.031	18.366
5.5	2.328	3.767	5.702
6.5	.628	.968	1.462
7.5	.238	.359	.538
9.0	.034	.057	.084
Total	121.326	291.093	469.205

TABLE 14

FAST NEUTRON DOSE RATES ONE FOOT FROM THE SURFACE OF THE PRESSURE VESSEL AND NOZZLE END OF THE UNSHIELDED CORE

Rads(ethylene)/Sec.

α	D_N
0°	1.987×10^5
25°	1.458×10^5
54°	6.491×10^4
90°	1.391×10^5
126°	4.756×10^4
162°	3.390×10^5
180°	5.597×10^5

TABLE 15

TOTAL DOSE RATES ONE FOOT FROM THE SURFACE OF THE PRESSURE VESSEL AND NOZZLE END OF THE UNSHIELDED CORE

Rads / sec

α	D_N
0°	3.612×10^5
25°	2.637×10^5
54°	2.231×10^5
90°	4.507×10^5
126°	1.689×10^5
162°	6.301×10^5
180°	1.029×10^6

TABLE 16

NEUTRON FLUX LEVELS ONE FOOT FROM THE SURFACE OF THE PRESSURE VESSEL AND NOZZLE END OF THE UNSHIELDED CORE

Angle, α	Neutrons / cm^2 - sec. Fast Flux	Thermal Flux
0°	7.545×10^{13}	1.680×10^{12}
90°	8.569×10^{13}	1.767×10^{14}
180°	2.853×10^{14}	7.041×10^{13}

TABLE 17

HEAT INPUT TO PROPELLANT TANK

Tank Angle	W_γ (MW)	W_n (MW)	$W_{n,\gamma}$ (MW)	$W_{Tot.}$ (MW)
25°	0.331	0.070	0.239	0.640
30°	0.462	0.095	0.329	0.886
37.5°	0.663	0.130	0.450	1.243

W_γ = Core Gamma Heating

W_n = Fast Neutron Kinetic Heating

$W_{n,\gamma}$ = Capture Gamma Heating

TABLE 18

TOTAL AND MINIMUM SHIELD WEIGHTS FOR 80% CENTERLINE ATTENUATION
(Lithium Hydride - Stainless Steel Shield)

Per Cent Steel	Lithium Hydride Thickness, cm.	Stainless Steel Thickness, cm.	Shield Weight gm/cm^2
0	47.5	0	31.21
20	15.1	3.78	36.63
40	10.25	4.39	37.75
60	8.65	5.77	46.45

Per Cent Steel	Total Shield Thickness, cm.	Additional* Length, cm.	Engine Weight** gm/cm^2	Total Weight, gm/cm^2
0	47.5	34.8	35.64	66.85
20	18.88	6.18	6.33	42.96
40	14.64	1.94	1.99	39.74
60	14.42	1.72	1.76	48.21

Minimum Total Weight at 28 per cent Steel

Therefore, shield thickness = 14.64 cm.

= 10.54 cm. Lithium Hydride

= 4.1 cm. Stainless Steel

---

* Additional Length = Shield Thickness - 12.7 cm.

** Engine Weight = 1.024 gm/cm^3 x Additional Length

TABLE 19

SHIELD THICKNESSES FOR VARIOUS ATTENUATING FACTORS
(SHIELD MATERIAL: 63% Li H, 27% SS, 10% VOID BY VOLUME)

PER CENT ATTENUATION	SHIELD THICKNESS, cm.
80%	14.64
90%	22.50
93%	25.71
96%	31.86

TABLE 20

SHIELDED TANK HEAT INPUT, MW

TANK ANGLE	SHIELD THICKNESS, cm.			
	14.64	22.5	25.71	31.86
25°	.167* / .106	.118 / .050	.106 / .039	.0884 / .0211
30°	.271 / .139	.204 / .085	.197 / .0669	.152 / .0434
37.5°	.453 / .261	.384 / .189	.354 / .155	.319 / .0914

* Upper Number: Shield Radius = Core Radius = 45.059 cm.
Lower Number: Shield Radius = Reflector Radius = 62.099 cm.

TABLE 21

TANK HEAT INPUT REDUCTION FACTORS, PER CENT

TANK ANGLE	SHIELD THICKNESS, cm.			
	14.64	22.5	25.71	31.86
25°	73.9 / 83.4	81.6 / 92.2	83.4 / 93.9	86.2 / 96.7
30°	69.4 / 84.3	76.9 / 90.4	77.8 / 92.5	82.9 / 95.1
37.5°	63.6 / 79.0	69.1 / 84.9	71.5 / 87.5	74.3 / 93.7

TABLE 22

SHIELD WEIGHTS

Shield Thickness, cm.	W_c^*, lbs.	W_R^{**}, lbs.
14.64	537	1019
22.5	825	1566
25.71	942	1790
31.86	1168	2218

* Shield Radius = Core Radius

** Shield Radius = Reflector Radius

TABLE 23

GAMMA RAY FLUX LEVELS AROUND A SHIELDED* KIWI B-1 CORE

(Mev/cm^2 - sec x 10^{-12}) (Distance From Center of Core to Detector - 5ft.)

Operating Time: 20 min Operating Power: 1120 MW

	Angle, α, Degrees			
E_γ, Mev	0	15	30	45
0.3	---	---	.08	1.62
0.7	.19	.23	1.20	9.19
1.0	.35	.40	1.52	8.99
1.5	.77	.84	2.26	9.73
2.0	.91	.98	2.38	9.08
2.5	1.10	1.07	2.40	8.36
2.8	.89	.93	2.01	6.70
3.5	1.91	1.98	4.02	12.43
4.5	1.05	1.08	2.11	6.22
5.5	.40	.41	.79	2.27
6.5	.14	.14	.26	.74
7.5	.04	.04	.08	.23
9.0	.01	.01	.01	.05
Total	7.67	8.11	19.12	75.61

* Maximum Shield

TABLE 26

GAMMA RAY DOSE RATE LEVELS AROUND A SHIELDED KIWI B-1 CORE

(Rads / Sec x 10^{-2}) (Distance From Center of Core to Detector - 5 feet)

Operating Time: 20 Min Operating Power: 1120 MW

Angle, α, Degrees

Eγ, Mev	0	15	30	45
0.3	.014	.022	.576	11.664
0.7	1.383	1.674	8.736	66.903
1.0	2.436	2.784	10.579	62.570
1.5	4.920	5.367	14.441	62.175
2.0	5.460	5.880	14.280	54.480
2.5	5.656	5.992	13.440	46.816
2.8	4.806	5.022	10.854	36.180
3.5	9.626	9.979	20.261	62.647
4.5	4.956	5.098	9.959	29.358
5.5	1.728	1.771	3.413	9.806
6.5	.567	.567	1.053	2.997
7.5	.156	.156	.312	.897
9.0	.034	.034	.038	.190
Total	41.742	44.346	107.942	446.683

Astronuclear

TABLE 27

GAMMA RAY DOSE RATE LEVELS AROUND A SHIELDED KIWI B-1 CORE

(Rads/sec x 10^{-1}) (Distance From Center of Core to Detector - 10 feet)

Operating Time: 20 min Operating Power: 1120 MW

	Angle, α, Degrees			
Eγ, Mev	0	15	30	45
0.3	.058	.072	1.368	17.712
0.7	4.150	4.514	19.510	117.936
1.0	6.751	7.064	23.455	114.353
1.5	12.652	13.163	31.758	119.046
2.0	13.740	13.920	32.040	107.040
2.5	13.944	14.112	30.520	93.576
2.8	11.664	11.826	24.786	72.954
3.5	22.982	23.335	46.872	128.016
4.5	11.658	11.894	23.506	60.699
5.5	4.061	4.190	8.165	20.390
6.5	1.256	1.337	2.633	6.237
7.5	.351	.351	.741	1.870
9.0	.076	.076	.152	.380
Total	103.343	105.854	245.506	855.184

TABLE 28

GAMMA RAY DOSE RATE LEVELS AROUND A SHIELDED KIWI B-1 CORE

(Rads/sec x 10^9) (Distance From Center of Core to Detector - 20 Feet)

Operating Time: 20 min Operating Power: 1120 MW

	Angle, α, Degrees			
Eγ, Mev	0	15	30	45
0.3	.144	.360	4.608	21.672
0.7	9.755	13.541	58.822	188.625
1.0	15.730	20.114	68.765	195.854
1.5	29.075	34.634	90.163	222.180
2.0	31.500	37.200	90.360	209.040
2.5	31.864	37.408	85.568	188.832
2.8	26.676	31.158	69.174	149.364
3.5	52.618	61.286	130.234	269.960
4.5	26.715	31.341	65.183	130.791
5.5	9.331	11.016	22.680	44.626
6.5	2.916	3.483	7.250	13.932
7.5	.858	1.014	2.106	4.134
9.0	.190	.228	.456	.874
Total	237.372	282.783	695.369	1639.884

TABLE 29

TOTAL FAST NEUTRON DOSE RATES AROUND A SHIELDED KIWI B-1 CORE

Rads(ethylene)/Sec

Angle, α, Degrees

Distance, Feet	0	15	30	45
5	9.40×10^{2}	1.12×10^{3}	4.62×10^{3}	1.97×10^{4}
10	2.54×10^{2}	2.81×10^{2}	9.33×10^{2}	2.77×10^{3}
20	6.08×10^{1}	7.86×10^{1}	2.19×10^{2}	4.66×10^{2}

TABLE 30

NEUTRON FLUX LEVELS AT VARIOUS DISTANCES FROM A SHIELDED KIWI B-1 CORE

Angle $\alpha = 0^{\circ}$

Distance, Feet	Neutrons / cm^2 - sec	
	Fast	Thermal
5	4.248×10^{11}	6.772×10^{9}
10	1.148×10^{11}	1.828×10^{9}
20	2.749×10^{10}	4.381×10^{8}

TABLE 31

TOTAL DOSE RATES AROUND A SHIELDED KIWI B-1 CORE

RADS/SEC

Operating Time: 20 min Operating Power: 1120 MW

Distance, Feet	Angle, α, Degrees 0	15	30	45
5	5.11×10^3	5.56×10^3	1.54×10^4	6.43×10^4
10	1.28×10^3	1.34×10^3	3.38×10^3	1.13×10^4
20	2.98×10^2	3.61×10^2	9.14×10^2	2.11×10^3

TABLE 32

FAST NEUTRON FLUXES OUTSIDE A SHIELDED KIWI B-1 REACTOR CORE

(Neutrons/cm^2 - sec) (Distance From Center of Core to Detector, 5 feet)

Angle $\alpha = 0^\circ$

Neutron Energy Group	Flux
6.07 - 10 Mev	14.000×10^8
3.68 - 6.07	55.444
2.23 - 3.68	145.462
1.35 - 2.23	486.562
.821 - 1.35	757.152
.498 - .821	1001.509
.302 - .498	450.994
.183 - .302	22.277
.111 - .183	83.048
.0674 - .111	42.815
.0248 - .0674	80.096
.00912 - .0248	21.082
.00335 - .00912	19.328
.00123 - .00335	173.300
454 - 1230 ev	166.936
167 - 454	157.097
101 - 167	74.938
61.3 - 101	72.309
37.2 - 61.3	68.998
22.6 - 37.2	65.045
13.7 - 22.6	60.390
8.32 - 13.7	54.911
5.1 - 8.32	48.578
3.06 - 5.1	41.619
1.86 - 3.06	34.268
1.125 - 1.86	26.953
.625 - 1.125	22.950
Total	4248.061×10^8

TABLE 33

SIGNIFICANT CONSTITUENTS IN COMPONENT MATERIALS AFTER 20 MINUTES OPERATION AND 24 HOURS DECAY

ALUMINUM - Commercial Grades

Constituent	Maximum Concentration (Wt - %)	Activation Process	Half Life*	Source Strength 20 min exposure - 24 hr decay (mev/cc - sec)		
				0.8 Mev	1.3 Mev	2.0 Mev
Aluminum	80	$Al^{27}(n,\alpha)\ Na^{24}$	15 h		1.2×10^{8}	2.3×10^{8}
Copper	6.8	$Cu^{63}(n,\gamma)\ Cu^{64}$	12.8 h		7.6×10^{7}	
Manganese	0.9	$Mn^{55}(n,\gamma)\ Mn^{56}$	2.6 h	1.7×10^{8}		1.8×10^{8}
Zinc	6.1	$Zn^{64}(n,\gamma)\ Zn^{65}$	245 d		1.0×10^{7}	
		TOTAL		1.7×10^{8}	2.0×10^{8}	4.1×10^{8}

STAINLESS STEEL - Type 18-8

Iron	67.0	$Fe^{54}(n,p)\ Mn^{54}$	290 d	[illegible]	10^{6}	
		$Fe^{58}(n,\gamma)\ Fe^{59}$	45 d	**	4.3×10^{7}	
Chromium	20.0	$Cr^{51}(n,\gamma)\ Cr^{51}$	27.8 d	[illegible]	[illegible]	
Manganese	2.0	$Mn^{55}(n,\gamma)\ Mn^{56}$	2.6 h	[illegible]		1.1×10^{9}
Cobalt	0.2	$Co^{59}(n,\gamma)\ Co^{60}$	5.27 y		1.2×10^{8}	
Nickel	11.0	$Ni^{58}(n,p)\ Co^{58}$	71 d	7.2×10^{7}	7.3×10^{6}	
		$Ni^{64}(n,\gamma)\ Ni^{65}$	2.6 h		3.6×10^{6}	
		TOTAL		1.3×10^{9}	1.8×10^{8}	1.1×10^{9}

*isotopes whose half lives are less than 1 hour are omitted from the table since they will have decayed by seven decades (10^{-7}).

**Cr^{51} decay photons have an energy of .32 Mev and therfore are not included in the total.

TABLE 33 Con't

INCONEL - X

Constituent	Maximum Concentration (Wt.- %)	Activation Process	Half Life*	Source Strength 20 min. exposure - 24 hr decay (mev/cc - sec)		
				0.8 Mev	1.3 Mev	2.0 Mev
Nickel	70	$Ni^{64}(n,\gamma)\ Ni^{65}$	2.6 h	$1.1 \times 10^{**8}$	2.5×10^{7}	
		$Ni^{58}(n,p)\ Co^{58}$	71 d	9.8×10^{8}	9.8×10^{6}	
Chromium	16	$Cr^{50}(n,\gamma)\ Cr^{51}$	27.8 d	$9.8 \times 10^{**7}$		
Copper	0.2	$Cu^{63}(n,\gamma)\ Cu^{64}$	12.8 h		6.7×10^{6}	
Cobalt	1.0	$Co^{59}(n,\gamma)\ Co^{60}$	5.27 y		6.2×10^{8}	
Manganese	1.0	$Mn^{55}(n,\gamma)\ Mn^{56}$	2.6 h	6.2×10^{8}		5.6×10^{8}
Tantilum	1.2	$Ta^{181}(n,\gamma)\ Ta^{182}$	115 d	$2.2 \times 10^{**8}$	9.5×10^{8}	
		TOTAL		1.6×10^{9}	1.6×10^{9}	5.6×10^{8}

BERYLLIUM

	(PPM)					
Sodium	150	$Na^{23}(n,\gamma)\ N^{24}$	15 h		2.75×10^{7}	5.52×10^{7}
Nickel	400	$Ni^{58}(n,p)\ Co^{58}$	71 d	3.54×10^{5}	3.46×10^{5}	
Manganese	150	$Mn^{55}(n,\gamma)\ Mn^{56}$	2.6 h	4.08×10^{6}		4.13×10^{6}
Scandium	3	$Sc^{45}(n,\gamma)\ Sc^{46}$	84 d	1.45×10^{6}	1.82×10^{6}	
Cobalt	5	$Co^{59}(n,\gamma)\ Co^{60}$	5.27 y		1.67×10^{5}	
Copper	150	$Cu^{63}(n,\gamma)\ Cu^{64}$	12.8 h		2.42×10^{5}	
Aluminum	1600	$Al^{27}(n,\alpha)Na^{24}$	15 h		3.34×10^{5}	6.56×10^{5}
		TOTAL		5.88×10^{6}	3.01×10^{7}	6.03×10^{7}

GRAPHITE

Sodium	200	$Na^{23}(n,\gamma)\ Na^{24}$	15 h		2.2×10^{7}	4.4×10^{7}
Manganese	180	$Mn^{55}(n,\gamma)\ Mn^{56}$	2.6 h	2.9×10^{6}		2.9×10^{6}
Cobalt	100	$Co^{59}(n,\gamma)\ Co^{60}$	5.27 y		2.2×10^{6}	
		TOTAL		2.9×10^{6}	2.4×10^{7}	4.7×10^{7}

(*)(**) Refer to previous page.

TABLE 34

RESULTANT SOURCE STRENGTHS IN COMPONENT MATERIALS AFTER 20 MINUTES OPERATION AND 24 HOURS DECAY

COMPONENT MATERIAL	COMPONENT LOCATION	SOURCE STRENGTH (Sv) $\frac{\text{Mev}}{\text{cm}^3 - \text{sec}}$ 0.8 Mev	1.3 - Mev	2.0 Mev
Beryllium	Reflector	0.59×10^7	3.0×10^7	6.0×10^7
Graphite	Reflector	0.29	2.4	4.7
Aluminum	Support Plate or Reactor Vessel	17.	21	41
Inconel - X	Nozzle	160	170	56
Stainless Steel (18-8)	Reflector or Nozzle or Shield	130	18	110
Uranium Oxide + Carbon	Core (1120 MW)	8.1×10^{10}* 6.4×10^{12}**	2.0×10^{10} 8.5×10^{12}	1.4×10^{10} 6.1×10^{12}

* 24 hours after three equally spaced 20 minute runs in 30 days.

** 1000 seconds after one 20 minute run.

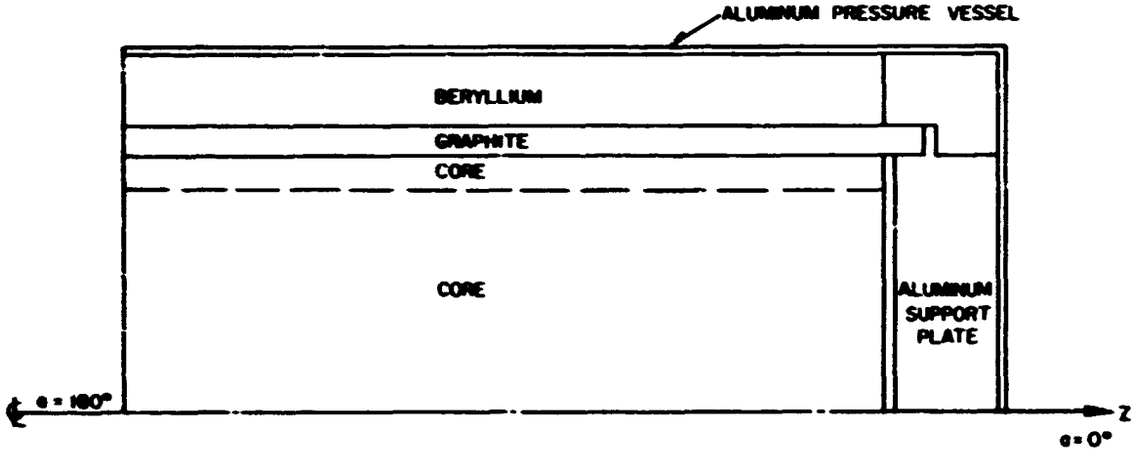

Figure 1 570A618

Geometrical Mockup of Reactor Configuration

Astronuclear

OPERATING POWER : 1120 MW
OPERATING TIME : 20 MINUTES

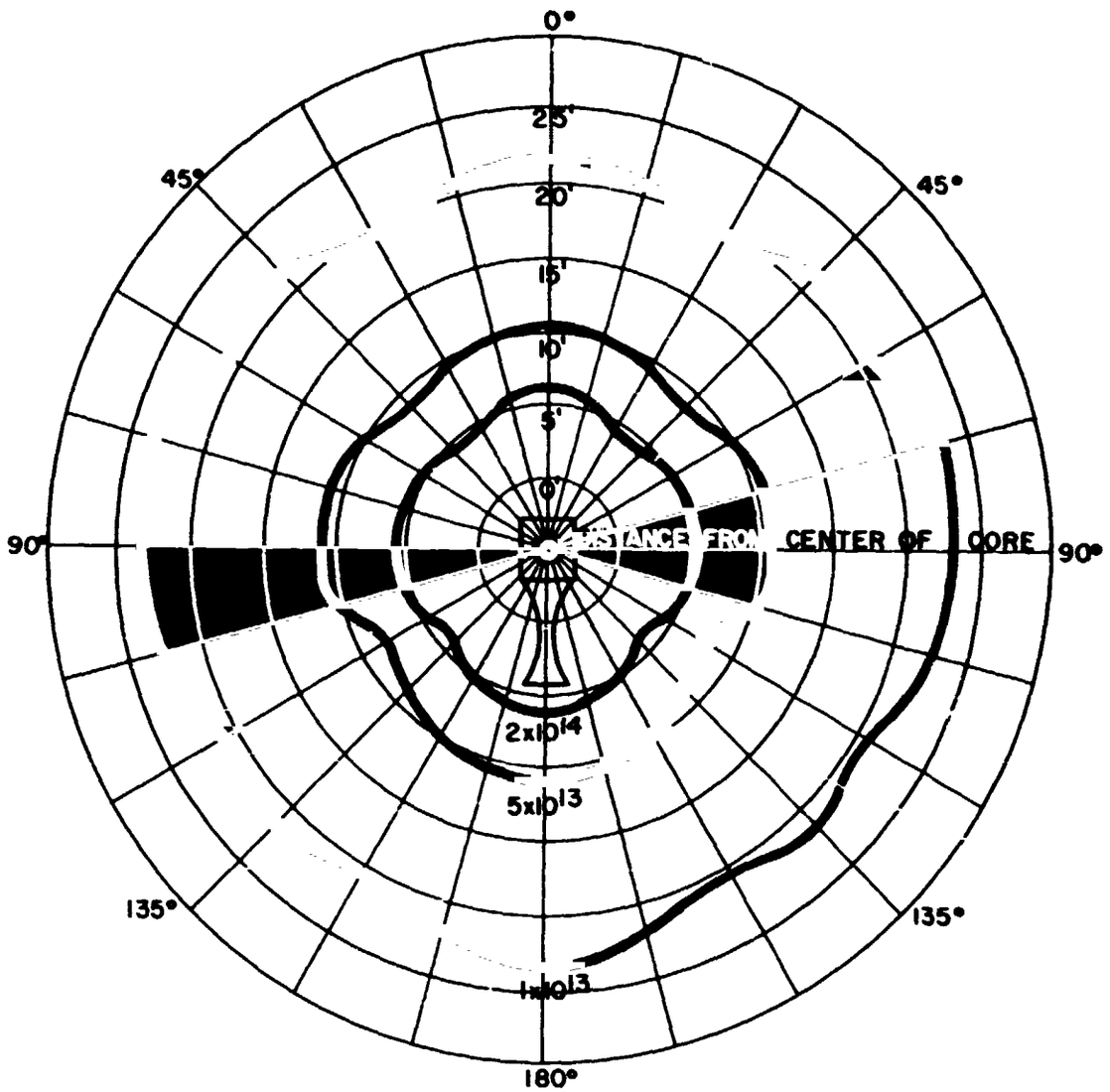

Figure 2 537554

Gamma Ray Flux Levels Around an Unshielded KIWI B-1 Core (MEV/CM^2-SEC)

OPERATING POWER : 1120 MW
OPERATING TIME : 20 MINUTES

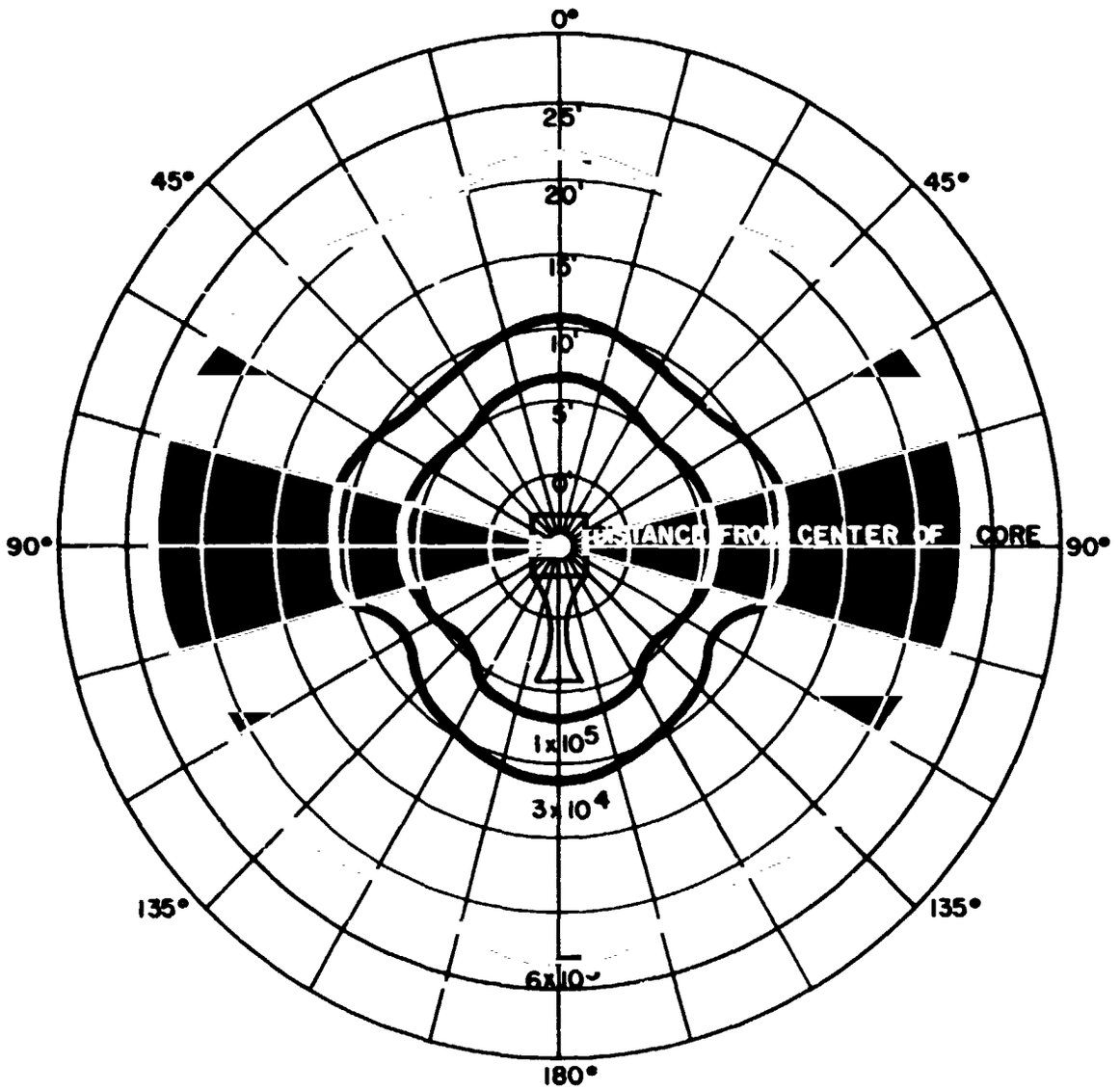

Figure 3

537555

Gamma Ray Dose Rate Levels Around an Unshielded KIWI B-1 Core (RADS/SEC)

Astronuclear

OPERATING POWER: 1120 MW
OPERATING TIME: 20 MINUTES

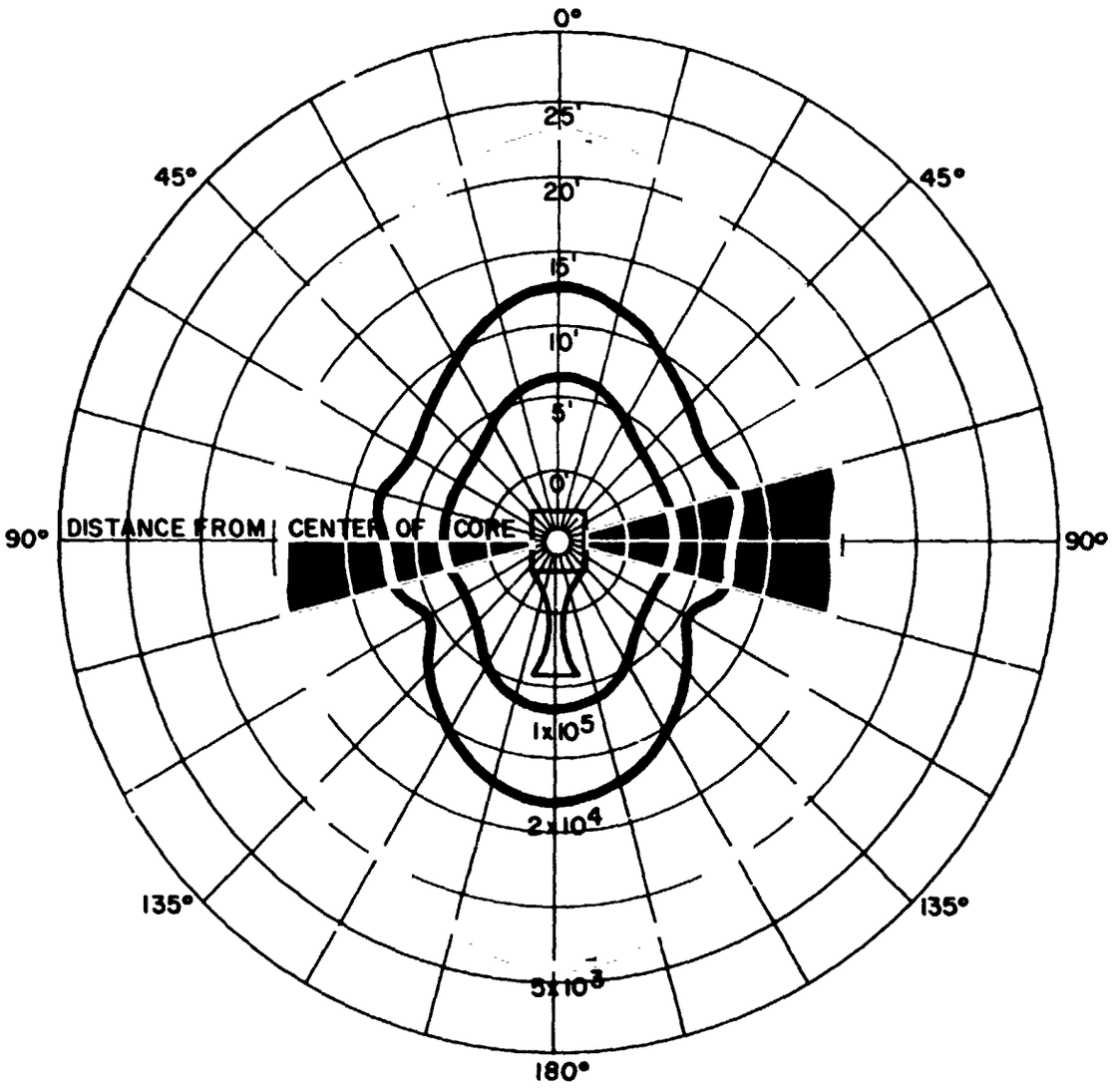

Figure 4 537553
Fast Neutron Dose Rate Levels Around an Unshielded KIWI B-1 Core (RADS (ETHYLENE)/SEC)

OPERATING POWER : 1120 MW
OPERATING TIME : 20 MINUTES

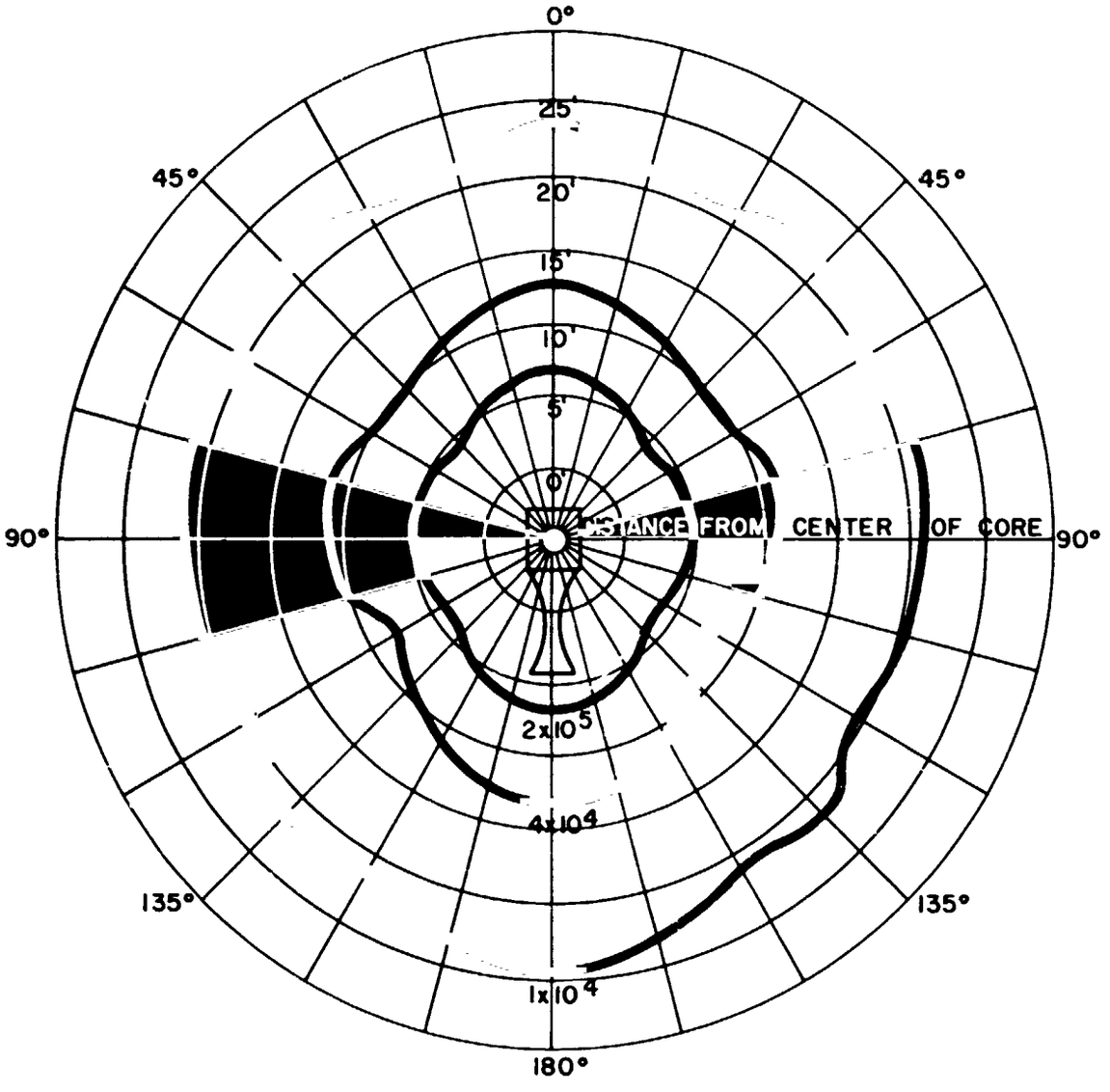

TOTAL DOSE RATE LEVELS AROUND AN UNSHIELDED KIWI B-1 CORE (RADS/SEC)

Figure 5 537556

Total Dose Rate Levels Around an Unshielded KIWI B-1 Core (RADS/SEC)

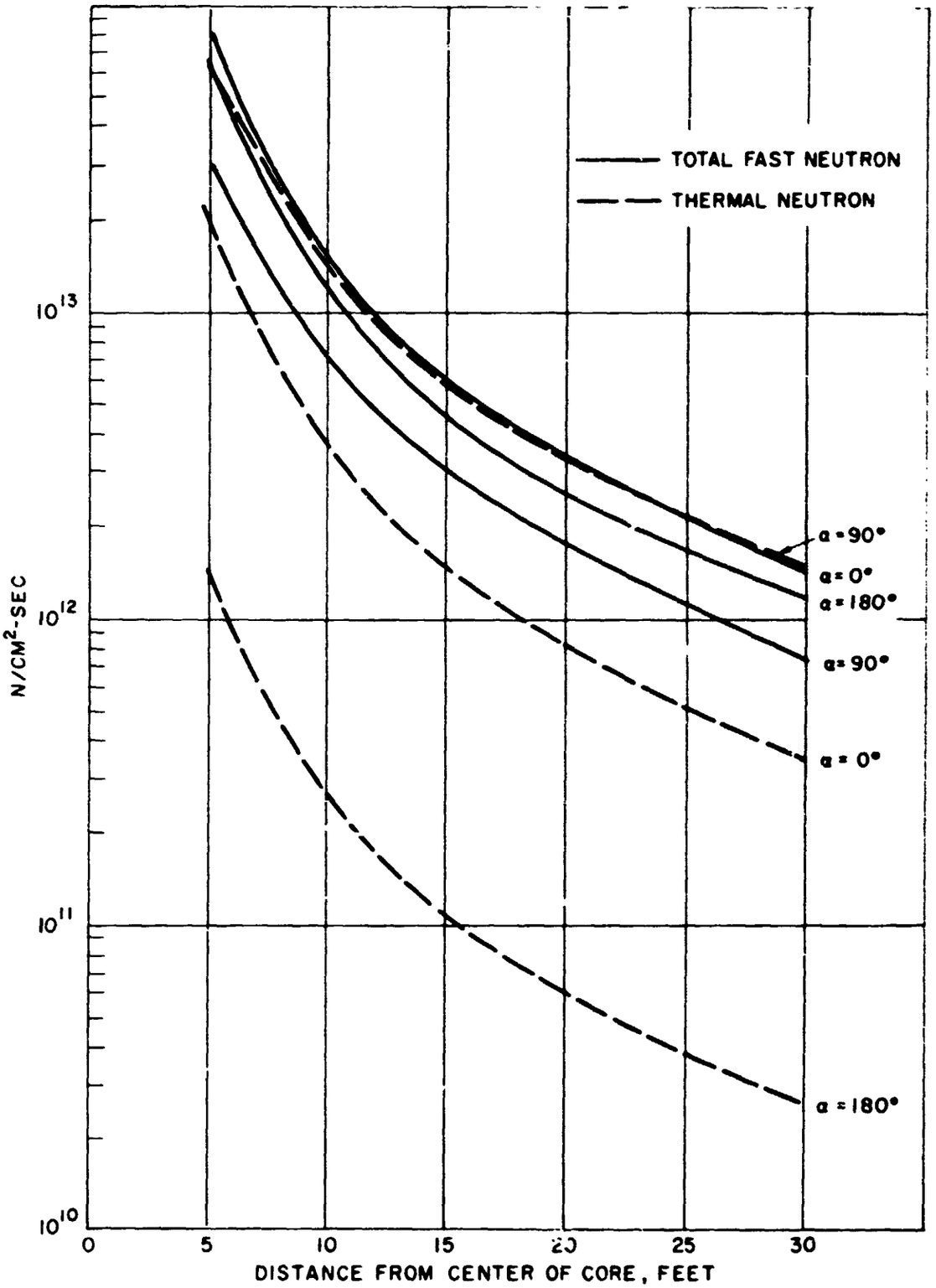

Figure 6 537236
Thermal Neutron Flux and Total Fast Neutron Flux at Several Positions Outside Unshielded KIWI B-1 Core, 1120 MW

Astronuclear

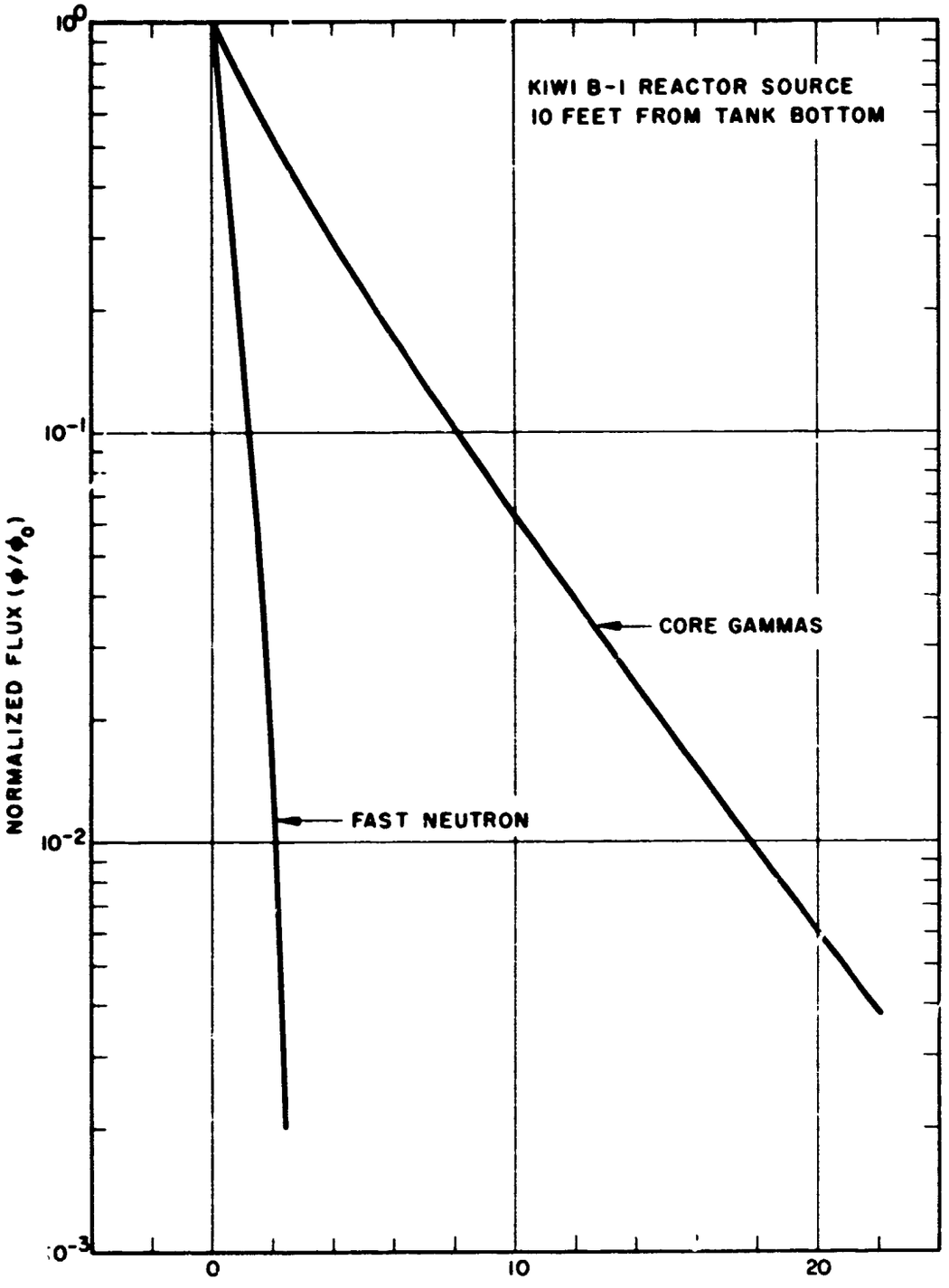

ATTENUATION OF FAST NEUTRONS AND CORE GAMMAS IN LIQUID HYDROGEN(ρ_{H_2} = 4.4 Lb./Ft. 3)

Figure 7 547088
Attenuation of Fast Neutrons and Core Gammas in Liquid Hydrogen (ρ_{H_2} = 4.4 Lb./Ft. 3)

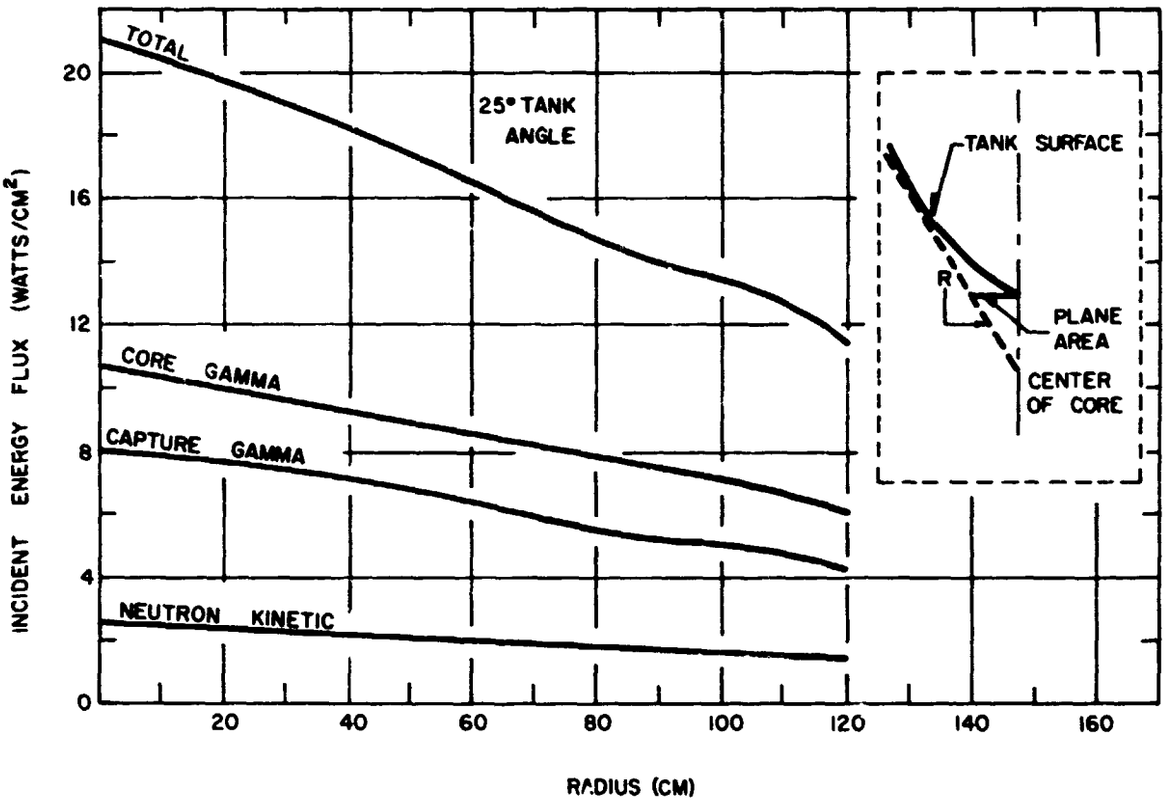

Figure 8 537608

Energy Flux Incident to Propellant Tank Projected on Plane Area at Bottom of Tank

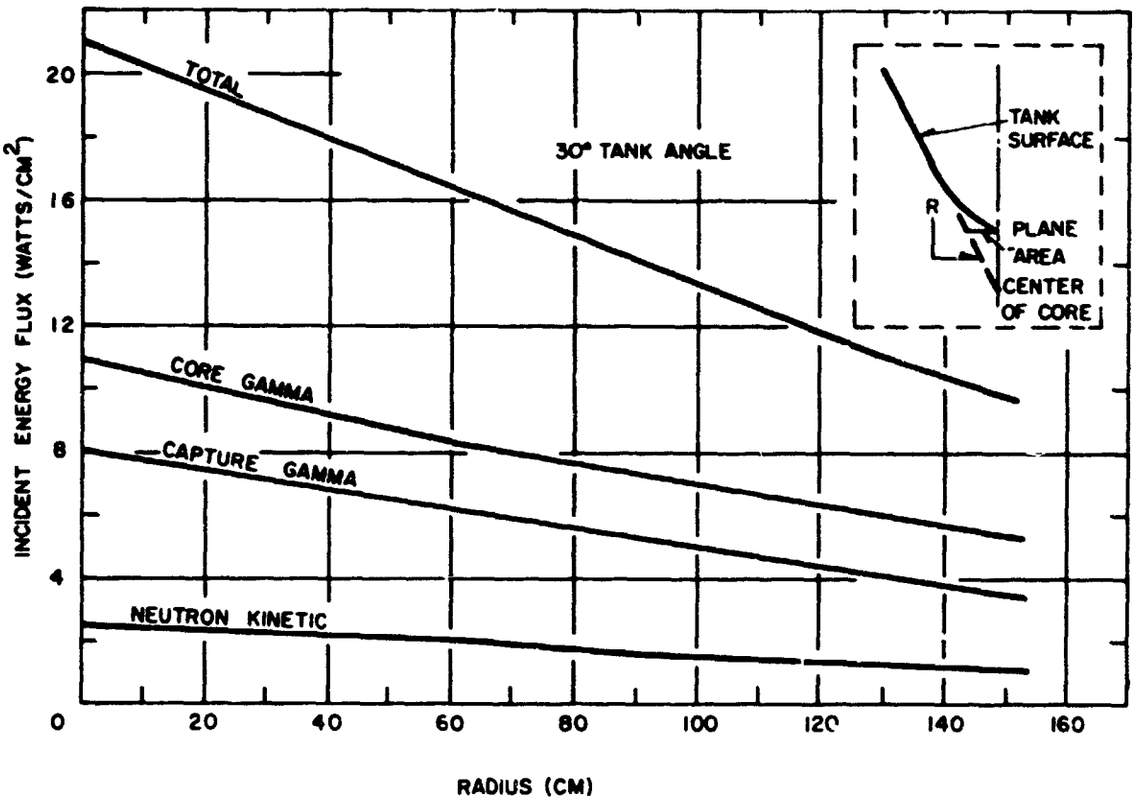

Figure 9 537609

Energy Flux Incident to Propellant Tank Projected on Plane Area at the Tank Bottom

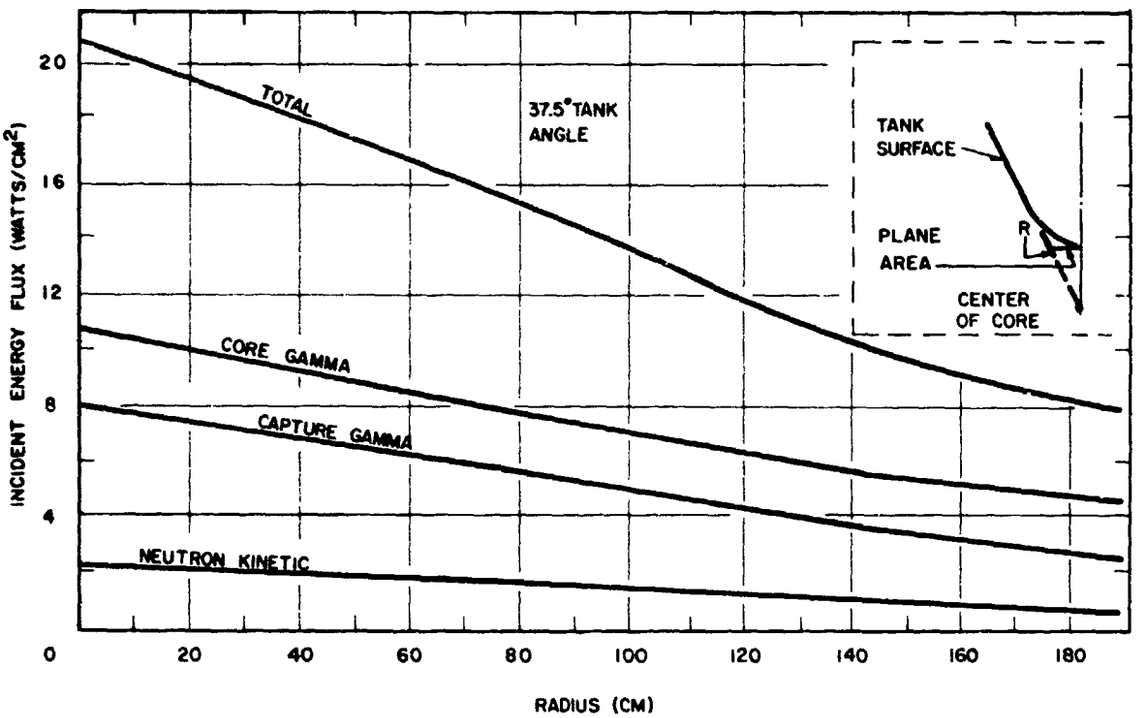

ENERGY FLUX INCIDENT TO PROPELLANT TANK PROJECTED ON PLANE AREA AT BOTTOM OF TANK

Figure 10 537610

Energy Flux Incident to Propellant Tank Projected on Plane Area at Bottom of Tank

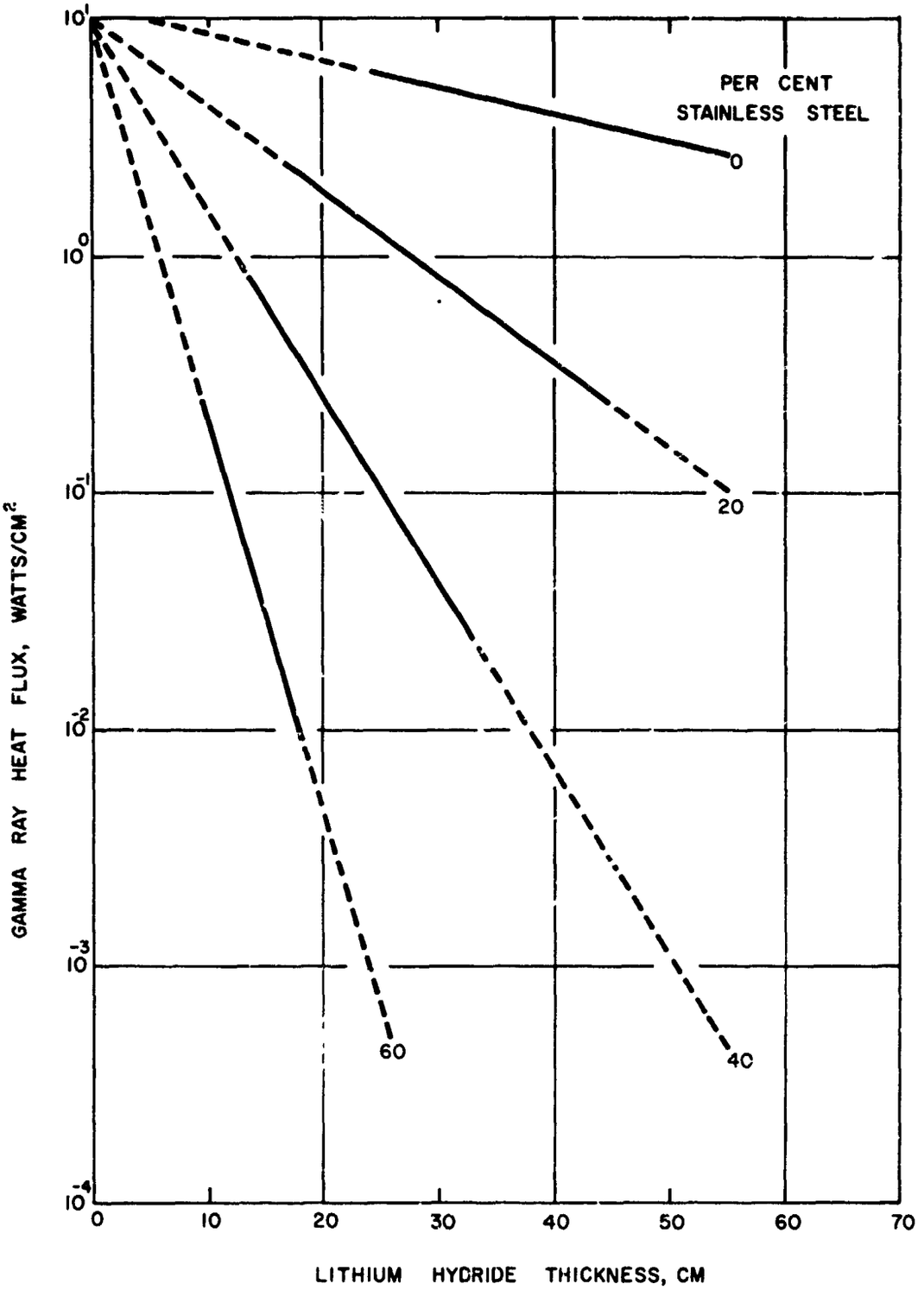

Figure 11 537611

Gamma Ray Heat Flux vs. Lithium Hydride Thickness

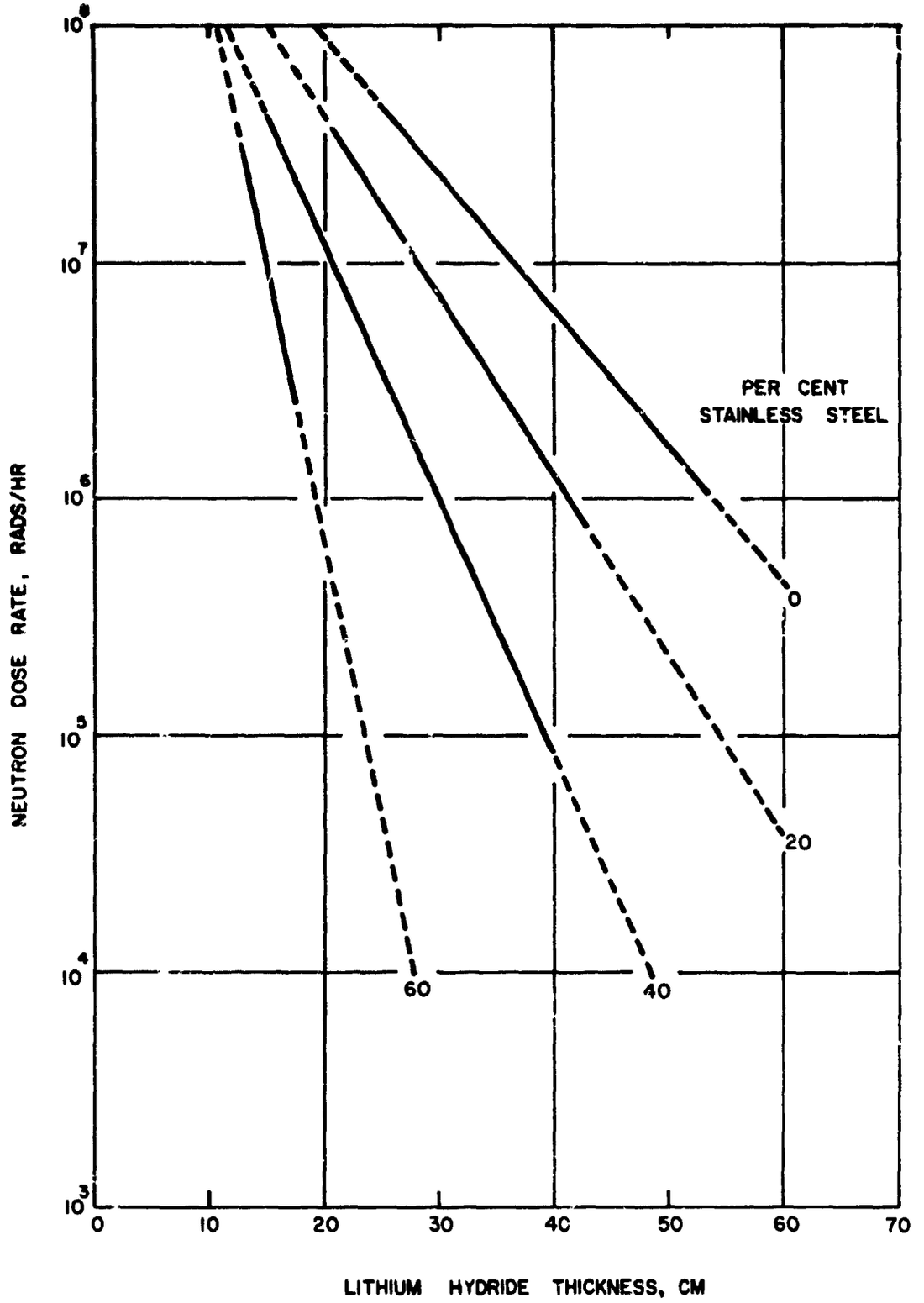

Figure 12

537612

Neutron Dose Rate vs. Lithium Hydride Thickness

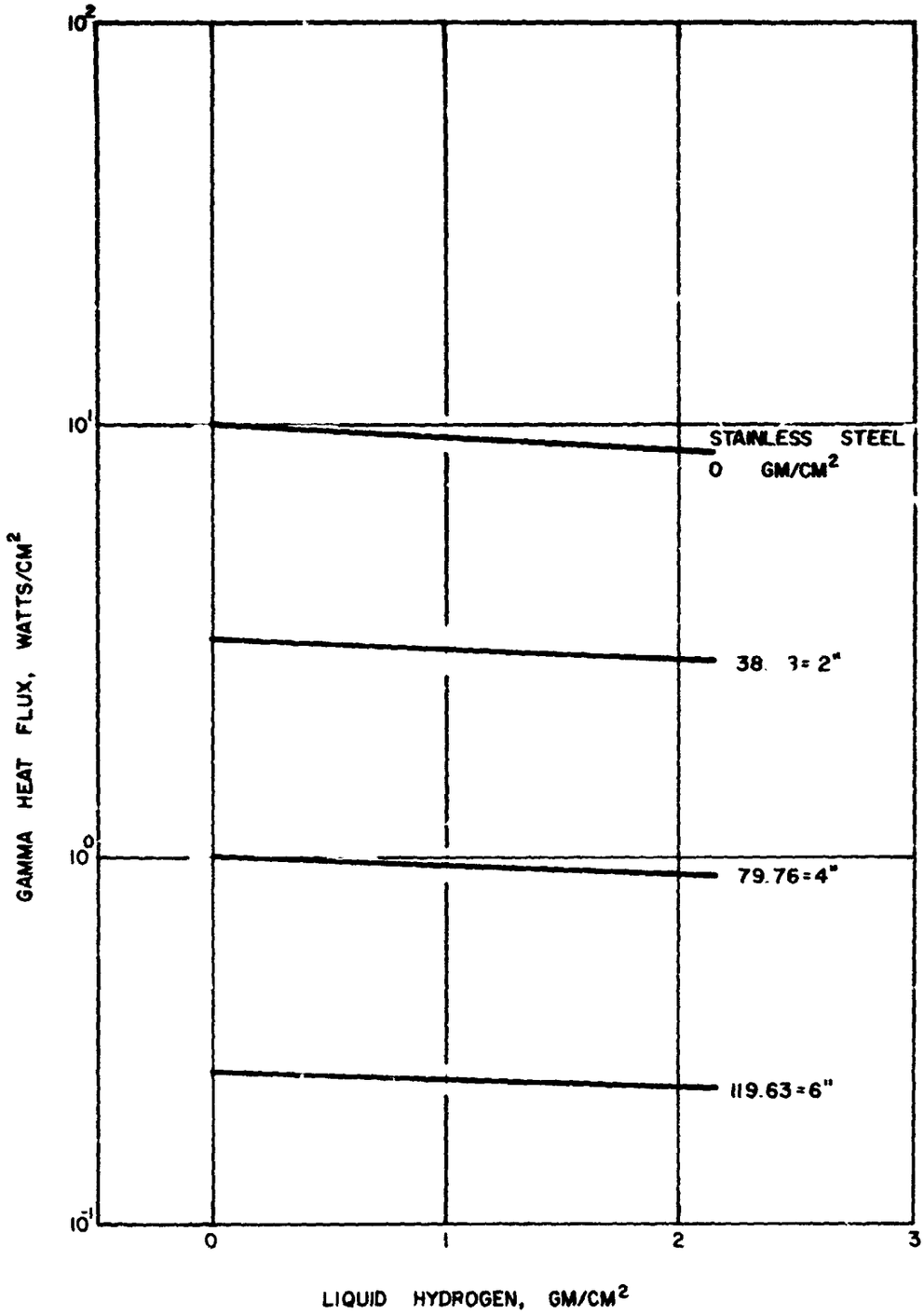

Figure 13 537613

Gamma Heat Flux vs. Liquid Hydrogen, GM/CM^2

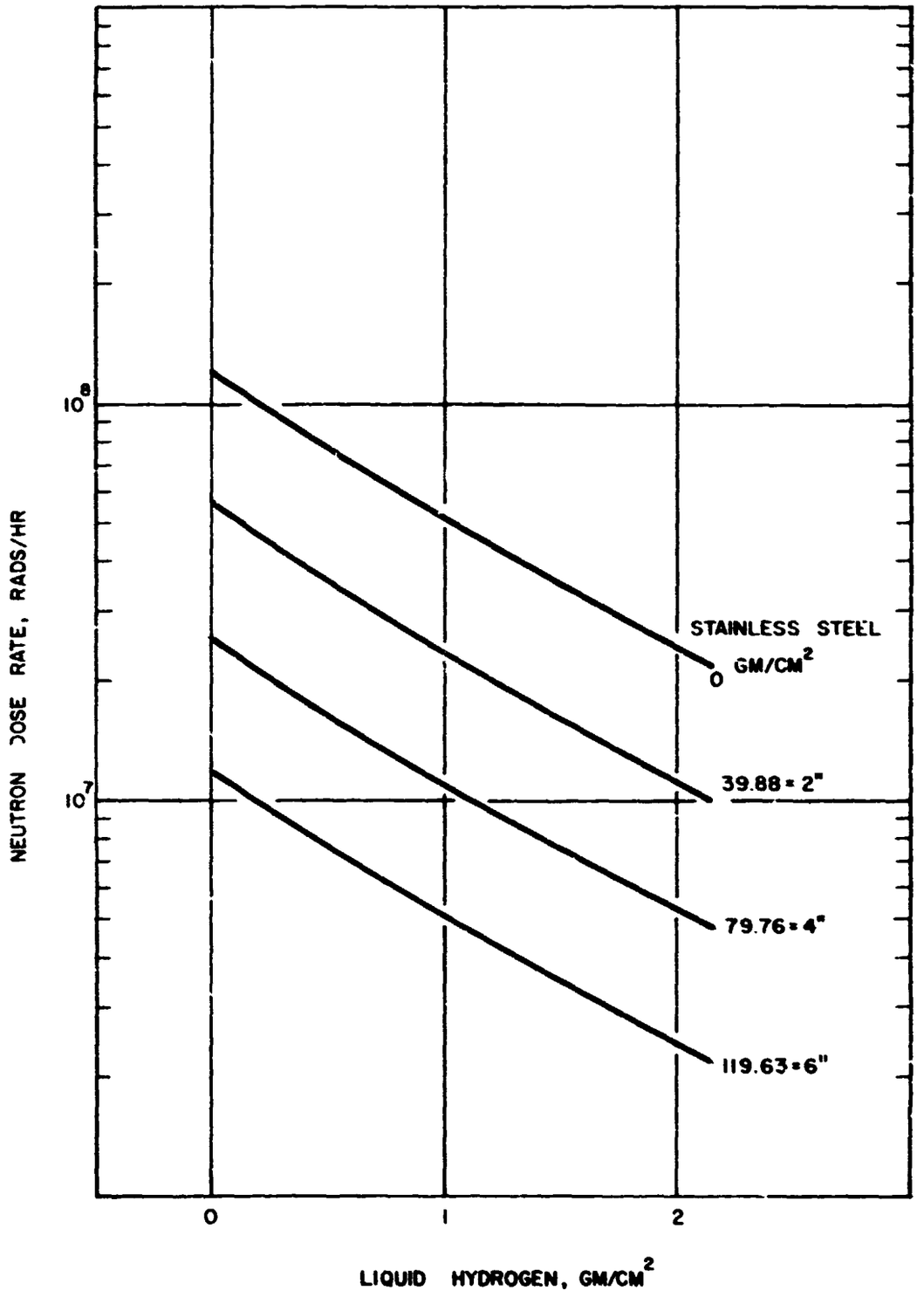

Figure 14 537614

Neutron Dose Rate vs. Liquid Hydrogen, GM/CM^2

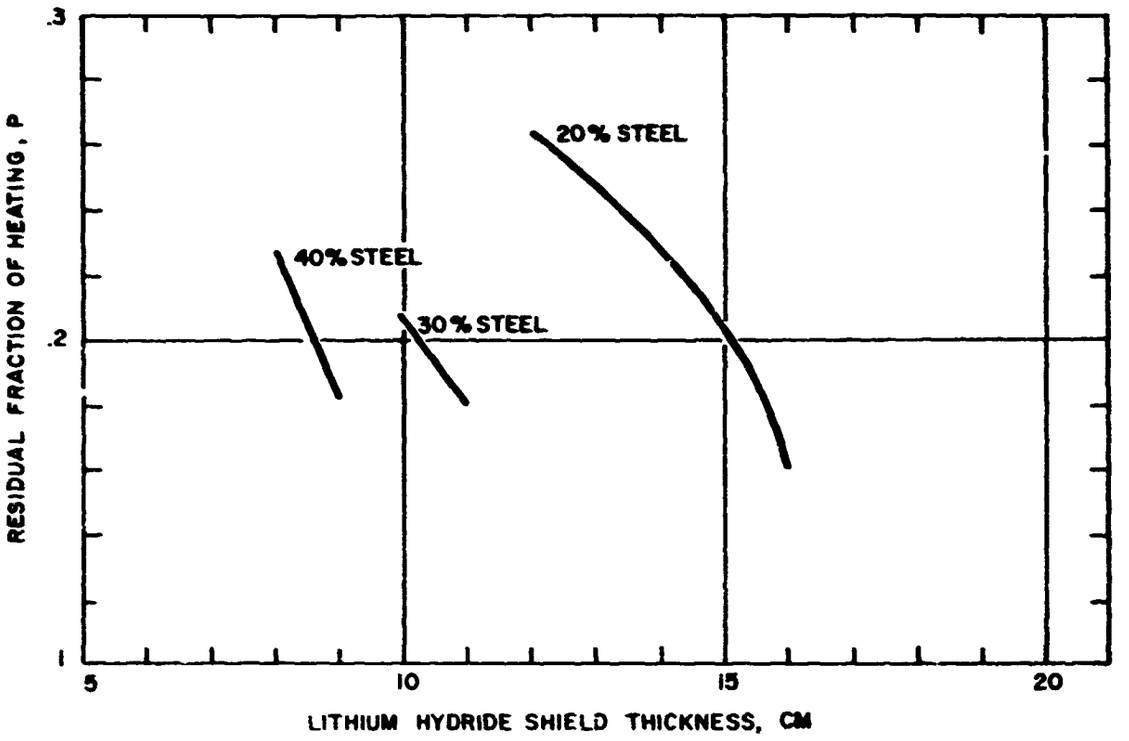

RESIDUAL FRACTION OF HEATING VS LITHIUM HYDRIDE SHIELD THICKNESS

Figure 15 537615

Residual Fraction of Heating vs. Lithium Hydride Shield Thickness

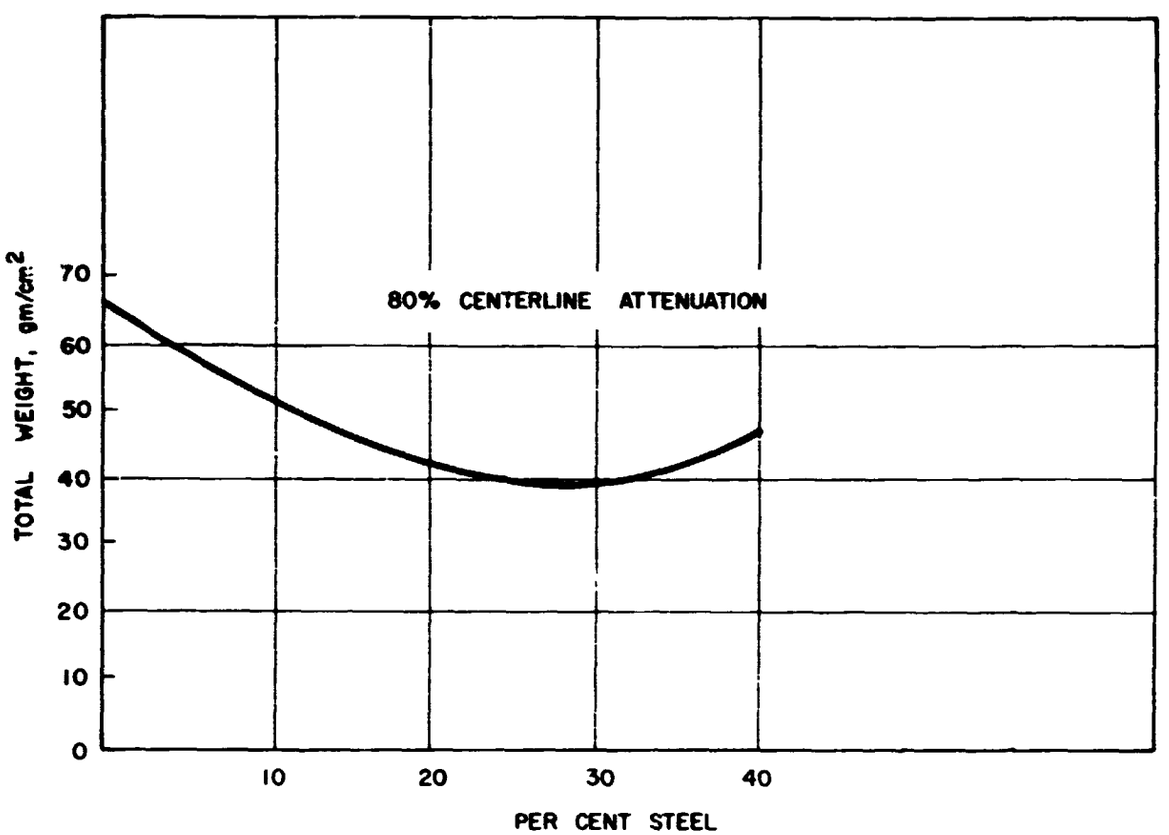

TOTAL WEIGHT VS PER CENT STEEL

Figure 16

Total Weight vs. Per Cent Steel

537616

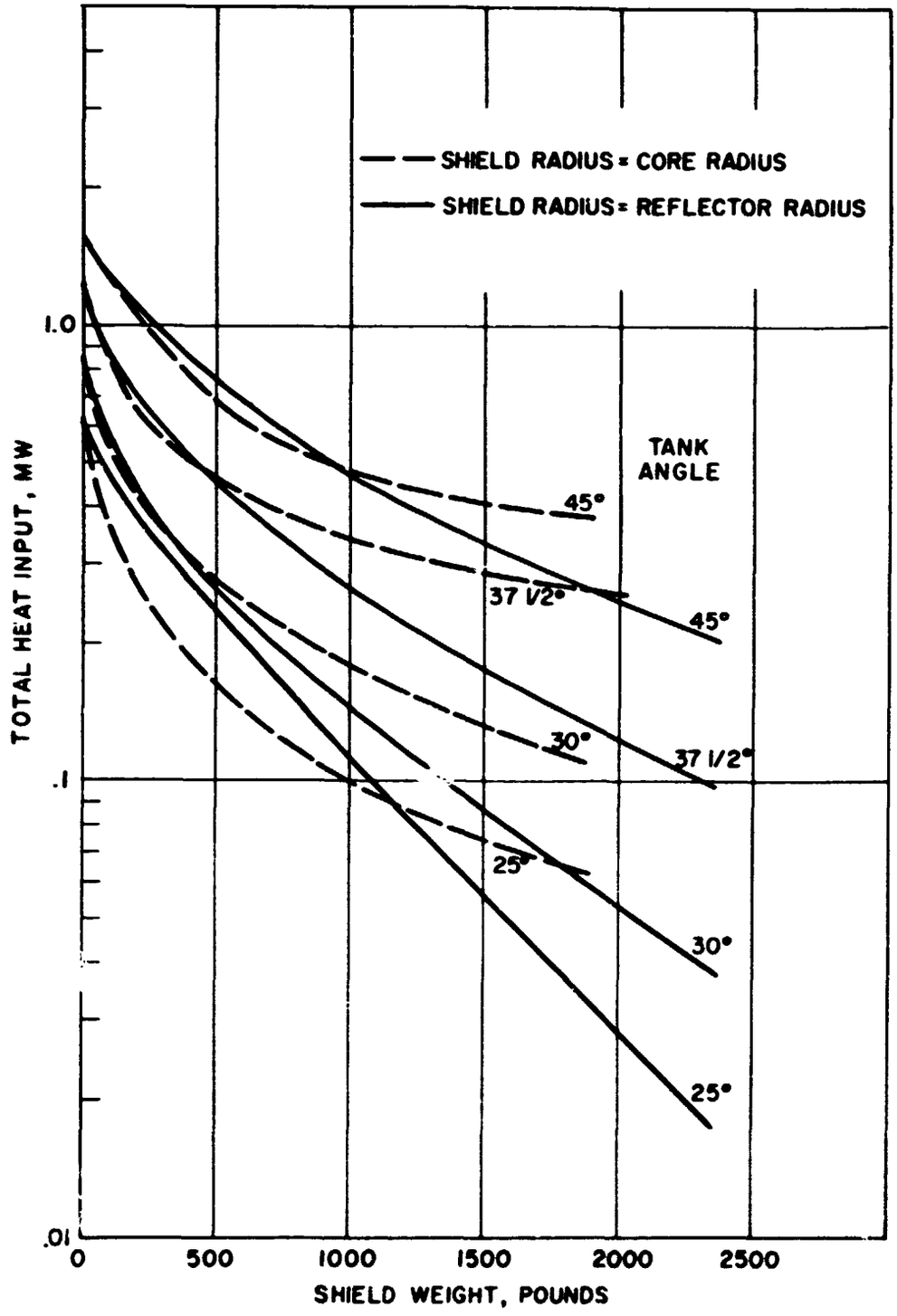

TOTAL PROPELLANT TANK HEAT INPUT VS SHIELD WEIGHT

Figure 17 537620

Total Propellant Tank Heat Input vs. Shield Weight

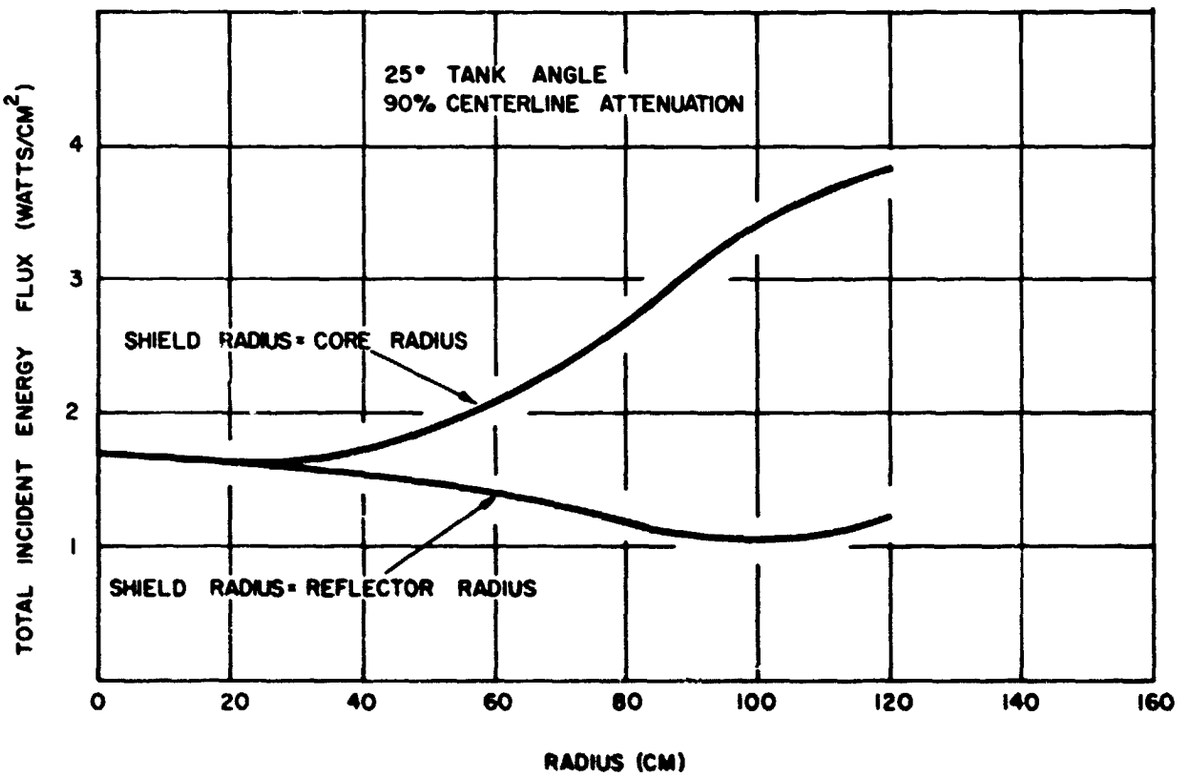

Figure 18 537617

Total Energy Flux Incident to Propellant Tank Projected on Plane Area at Bottom of Tank

Astronuclear

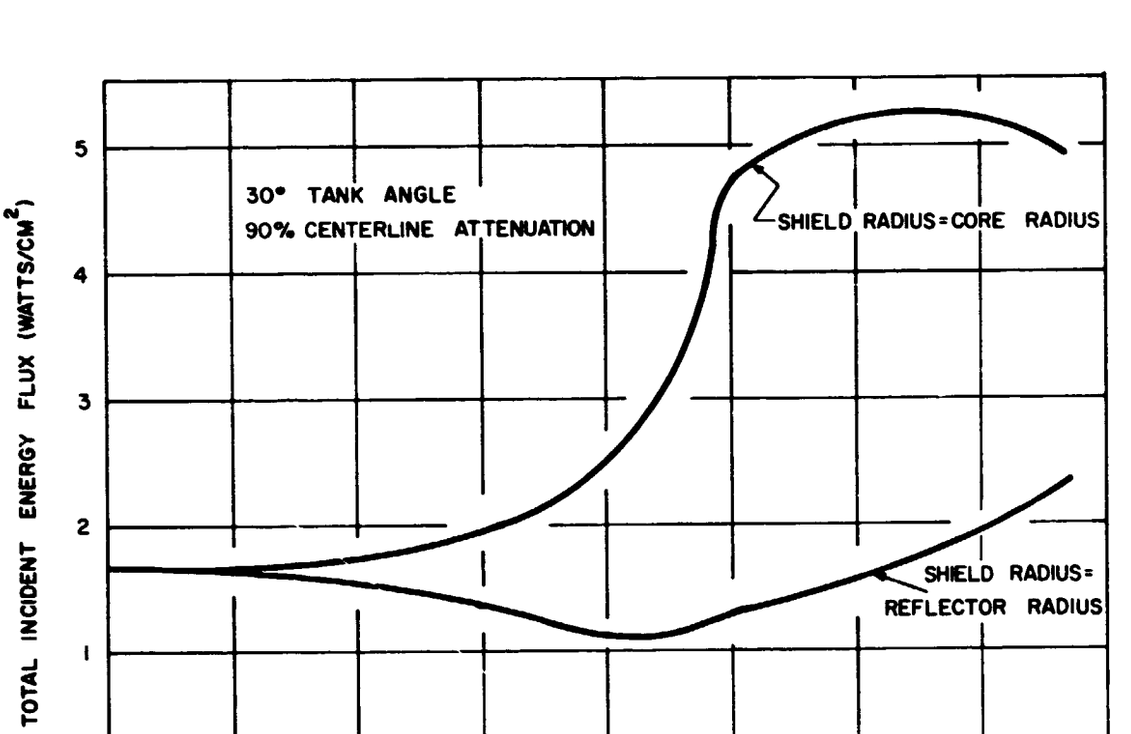

Figure 19 537618

Total Energy Flux Incident to Propellant Tank Projected on Plane Area at Bottom of Tank

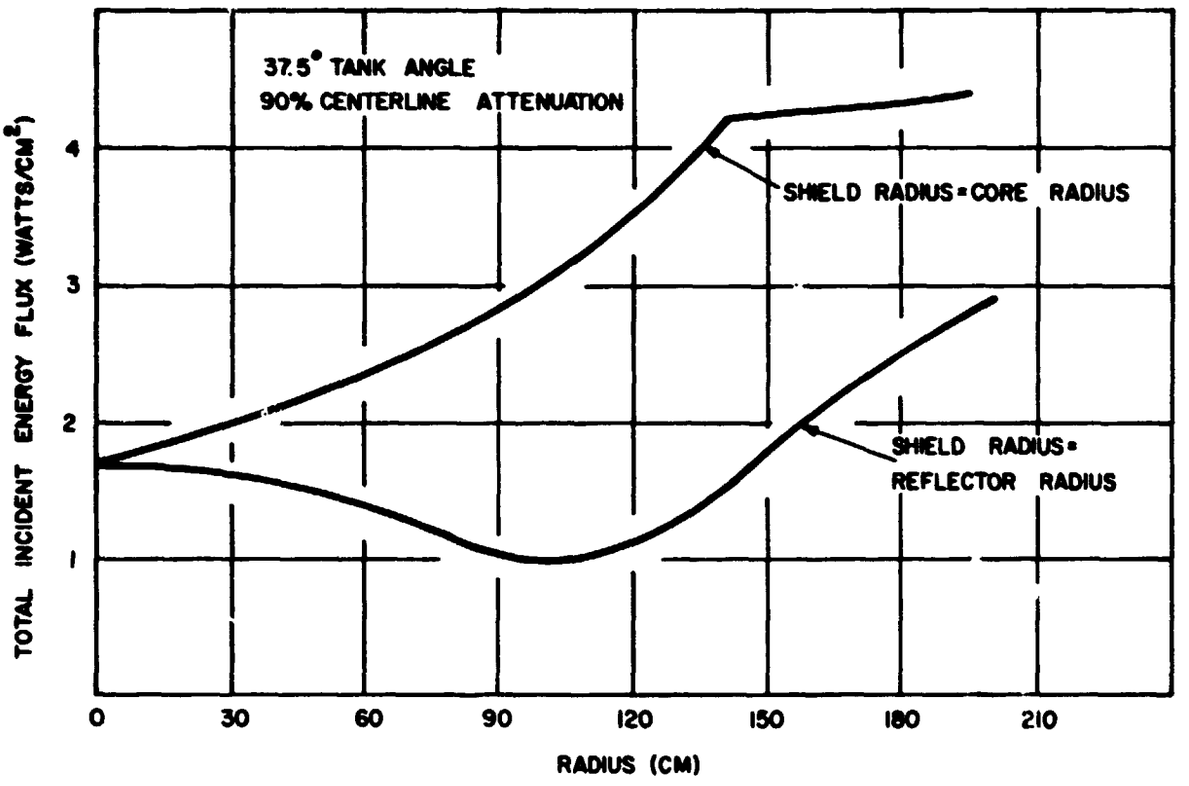

Figure 20 537619

Total Energy Flux Incident to Propellant Tank Projected on Planar Area at Bottom of Tank

Astronuclear

OPERATING POWER : 1120 MW
OPERATING TIME : 20 MINUTES
SHIELD : FOR 90 % PROPELLANT HEAT REDUCTION,
37.5° TANK ANGLE

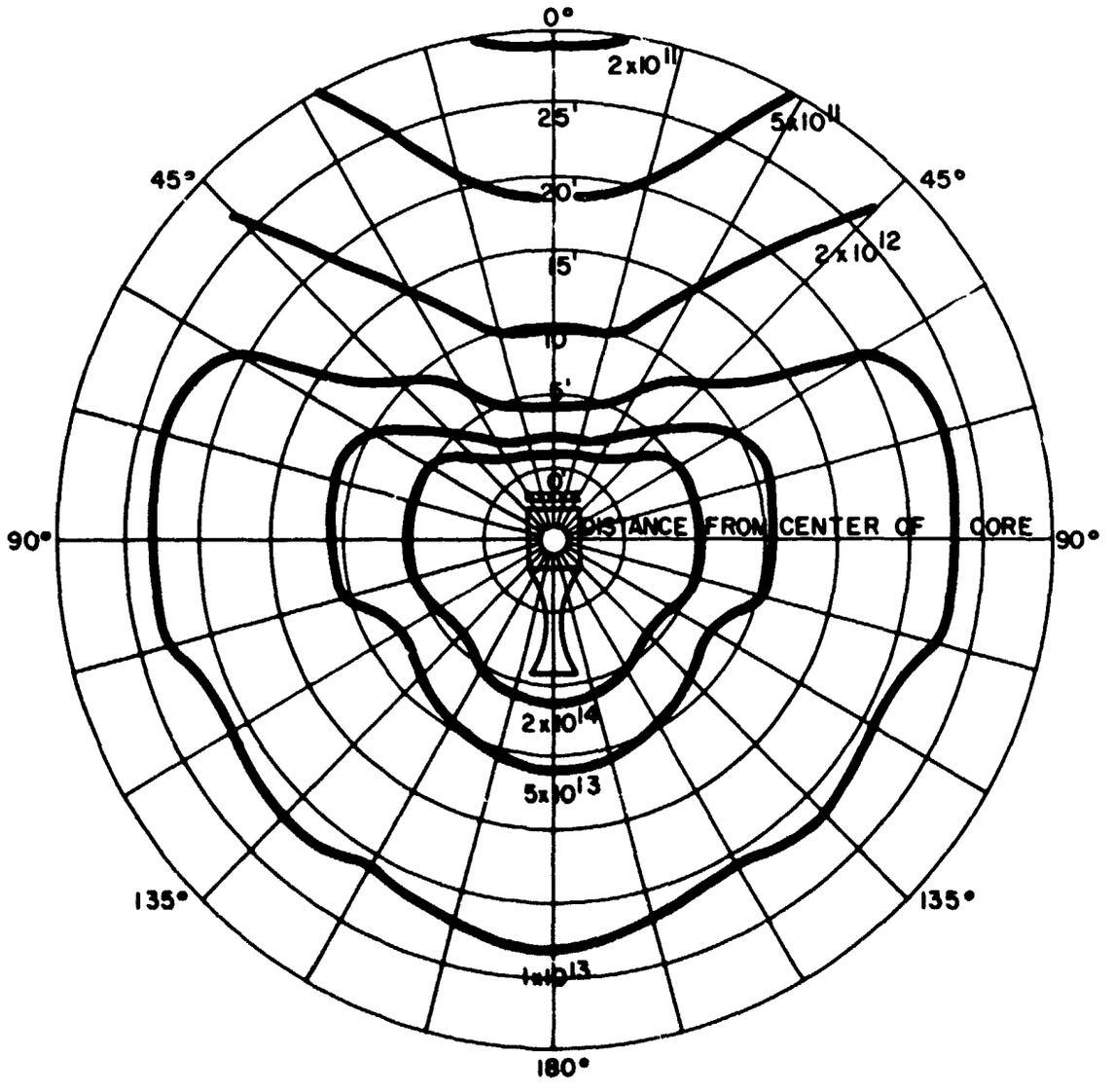

Figure 21 537639

Gamma Ray Flux Levels Around a Shielded KIWI B-1 Reactor Core (MEV/CM^2-SEC)

Astronuclear

OPERATING POWER : 1120 MW
OPERATING TIME : 20 MINUTES
SHIELD : FOR 90 % PROPELLANT HEAT REDUCTION,
37.5° TANK ANGLE

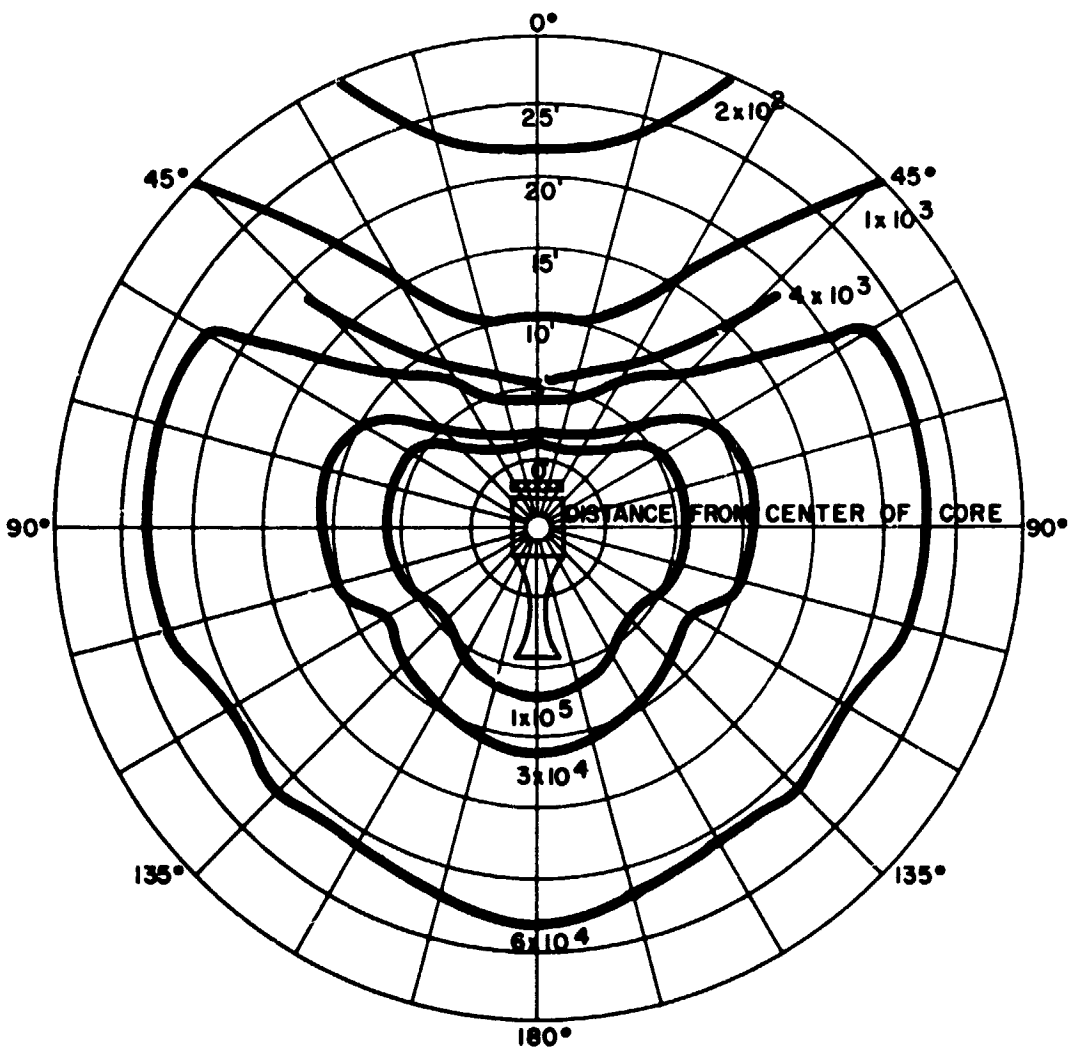

Figure 22

537640

Gamma Dose Rate Levels Around a Shielded KIWI B-1 Reactor Core (RADS/SEC)

OPERATING POWER : 1120 MW
OPERATING TIME : 20 MINUTES
SHIELD : FOR 90% PROPELLANT HEAT REDUCTION,
37.5° TANK ANGLE

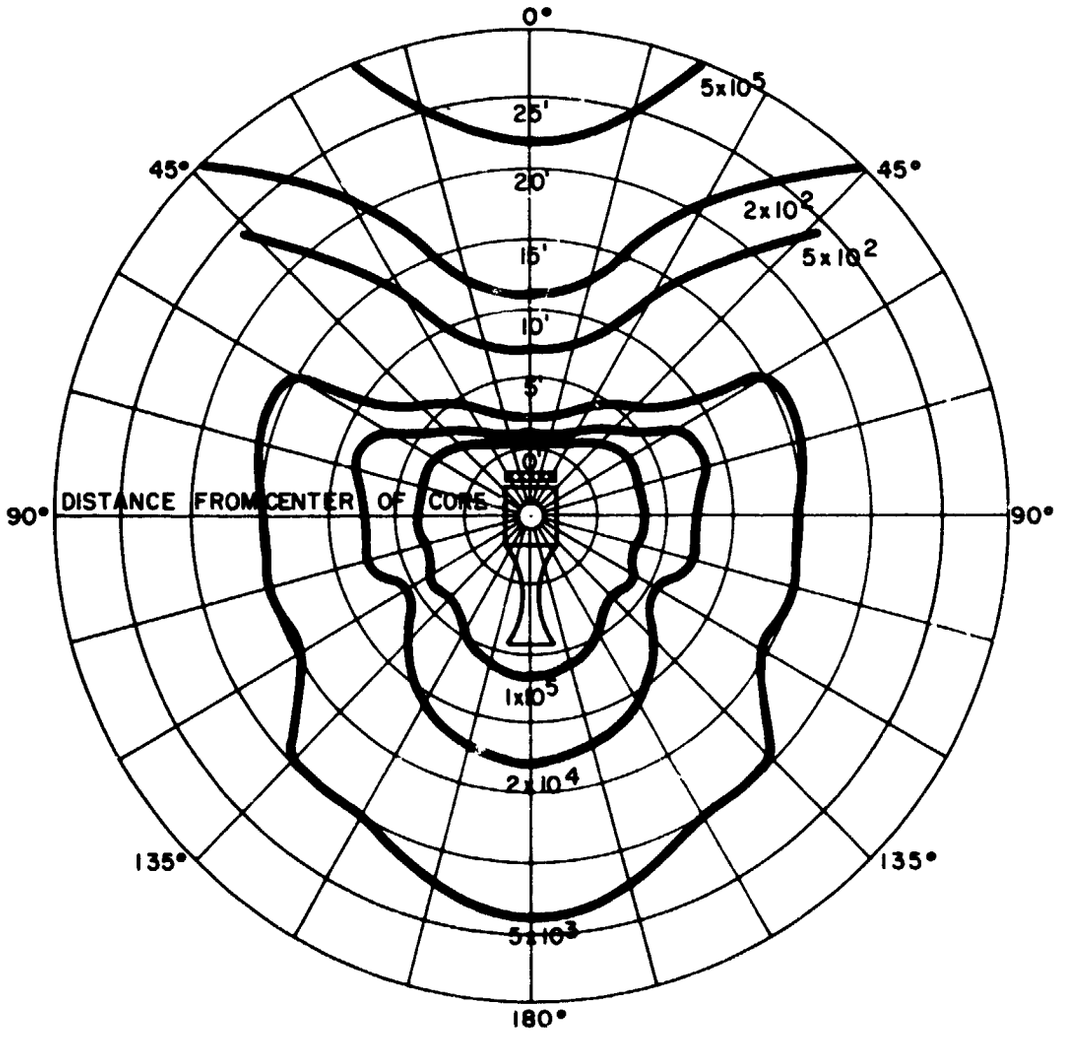

Figure 23 537641
Fast Neutron Dose Rate Levels Around a Shielded KIWI B-1 Reactor Core (RADS (ETHYLENE) SEC)

Astronuclear

OPERATING POWER: 1120 MW
OPERATING TIME: 20 MINUTES
SHIELD: FOR 90% PROPELLANT HEAT REDUCTION,
37.5° TANK ANGLE

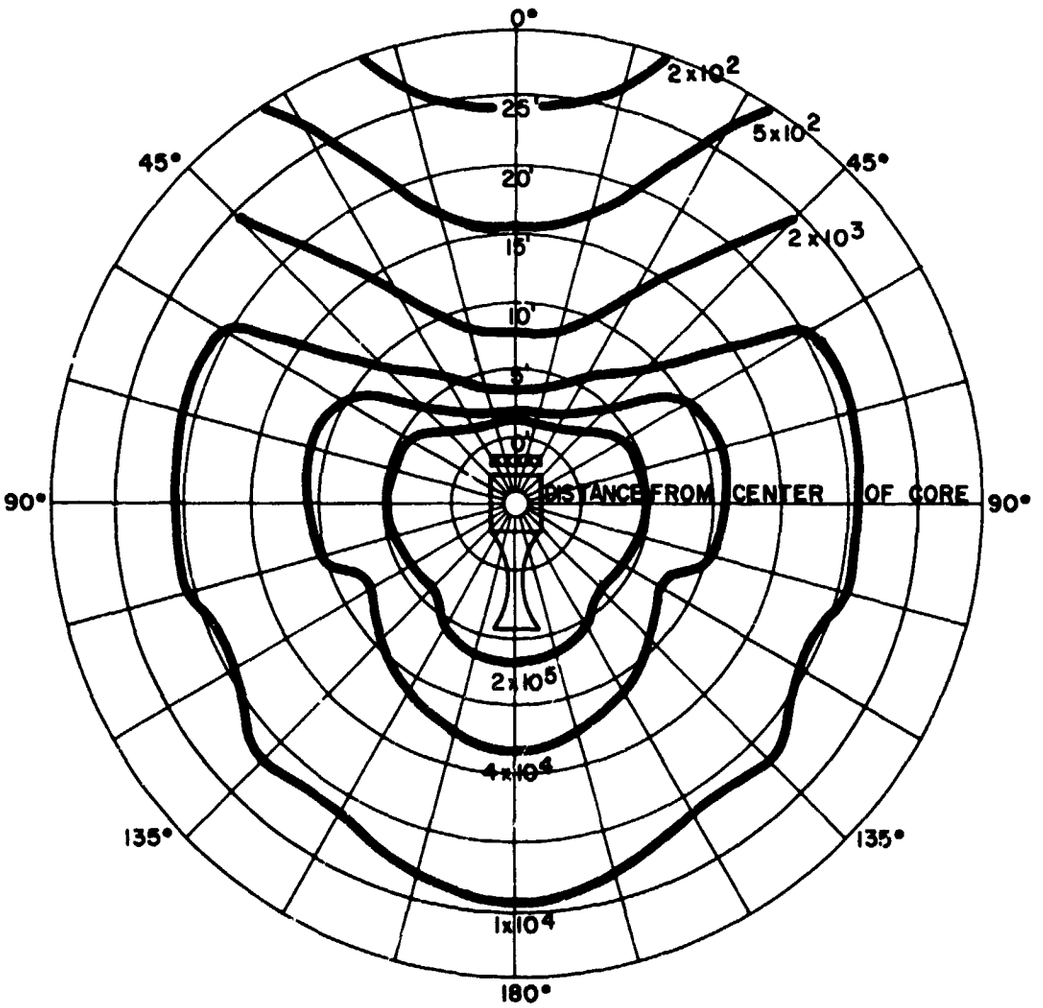

Figure 24 537643

Total Dose Rate Levels Around a Shielded KIWI B-1 Reactor Core (RADS/SEC)

Astronuclear

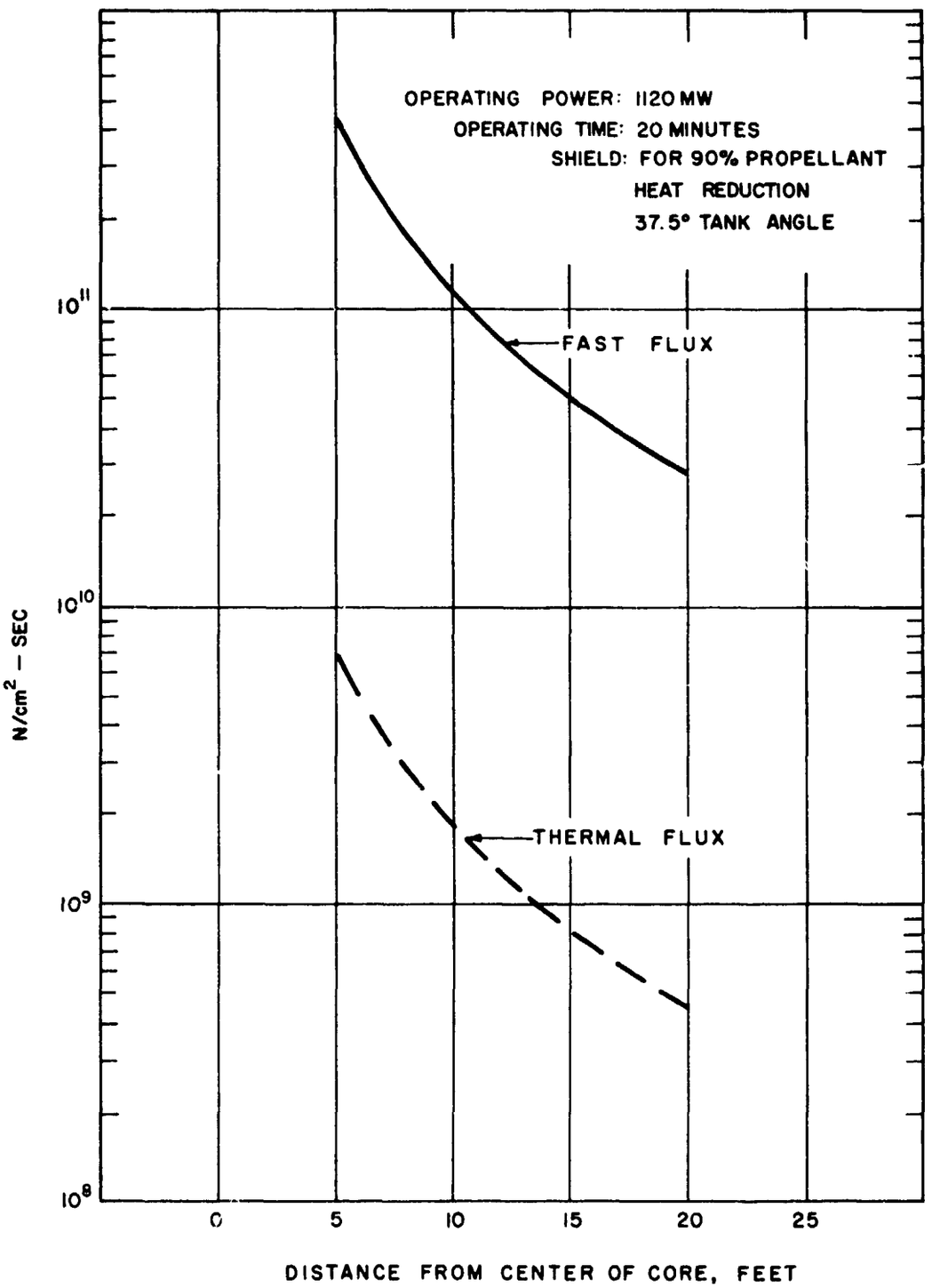

Figure 25 537642
Thermal Neutron and Total Fast Neutron Flux at $\alpha = 0^{\circ}$ Outside Shielded KIWI B-1 Reactor Core (N/cm^2-SEC)

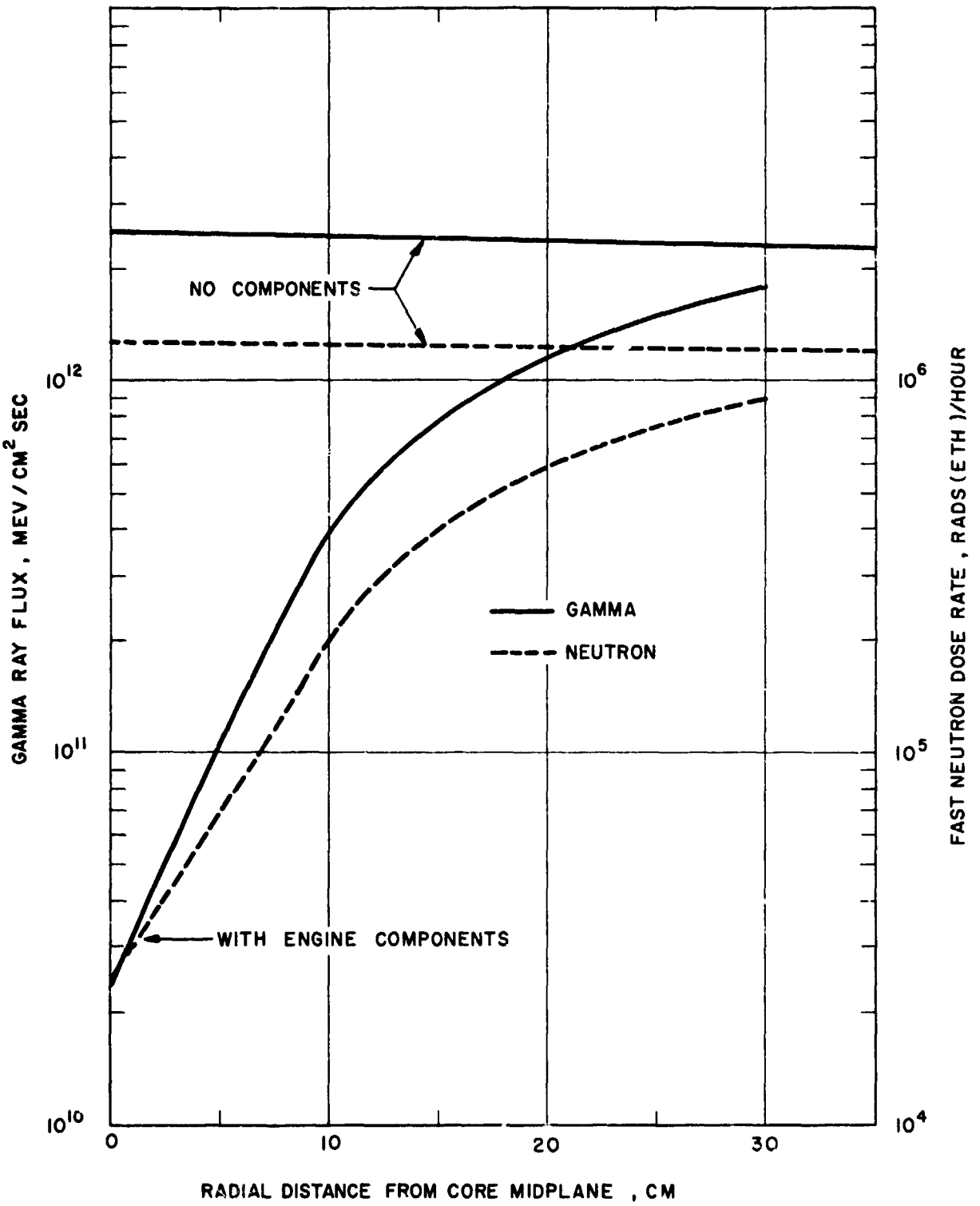

Figure 26 537552
Shielding Effect of Several Engine Components vs. Radial Distance Along Bottom of Propellant Tank

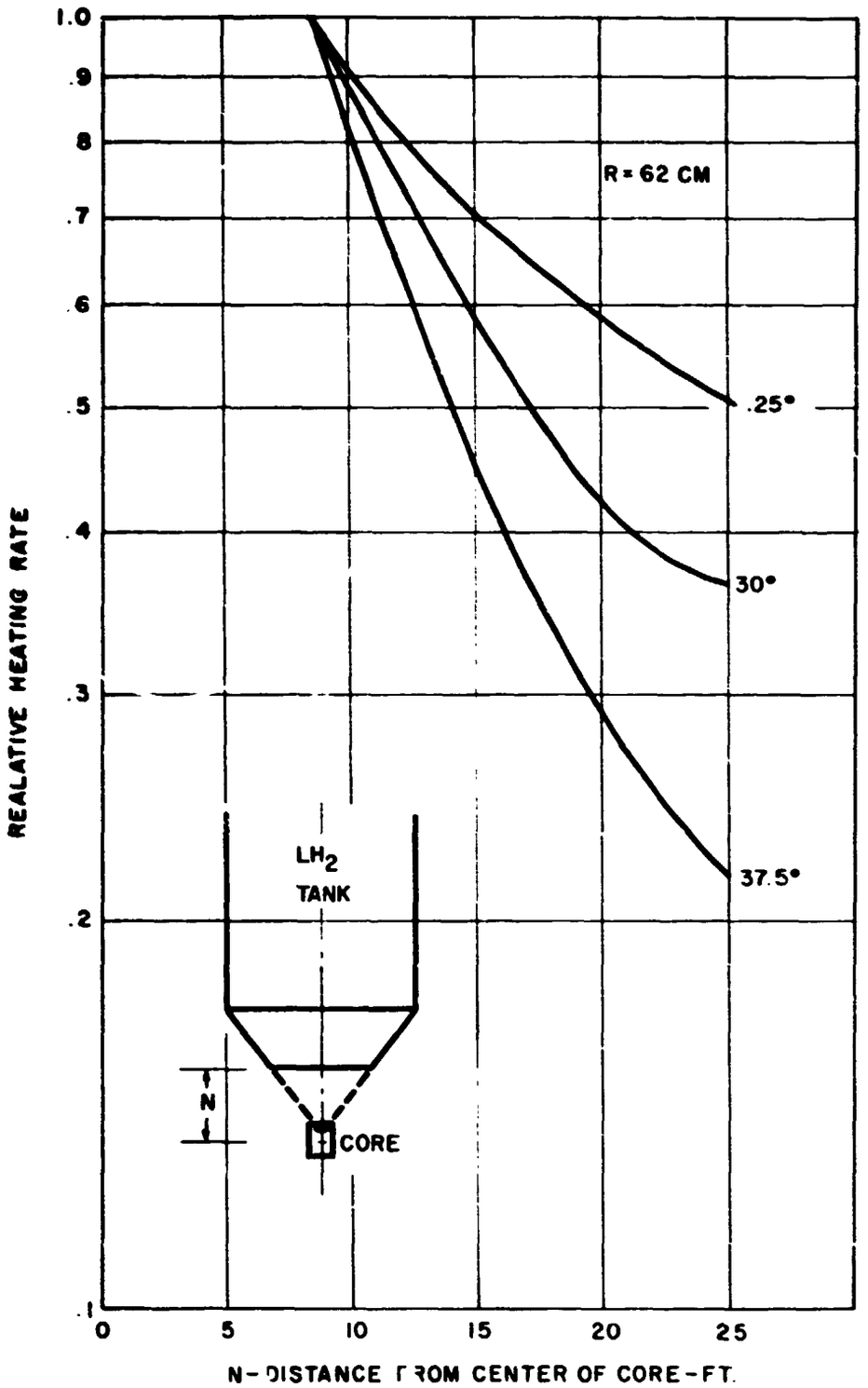

Figure 27 547195

Distance Attenuation Effect Along Vertical Centerline

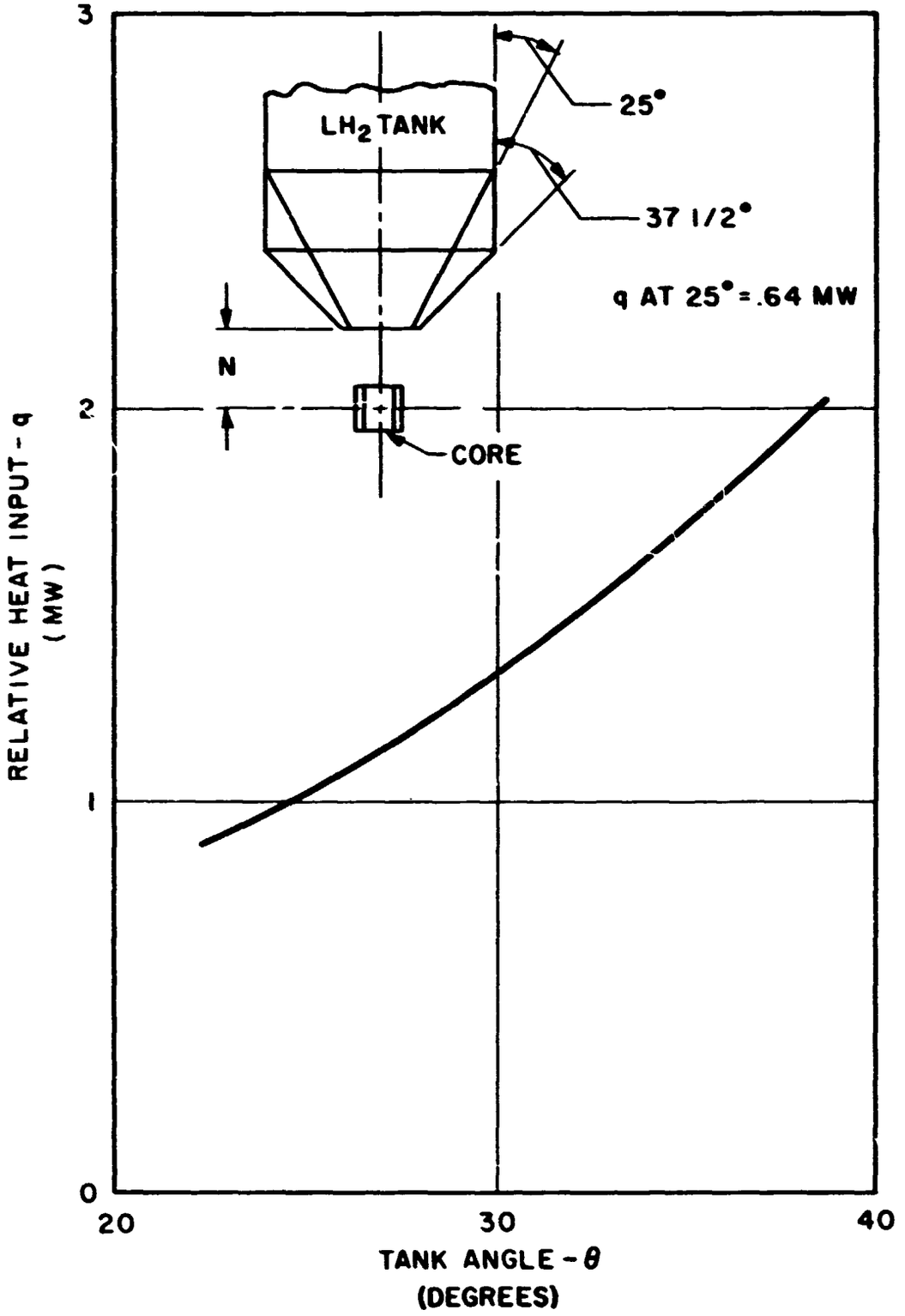

Figure 28

537623

Heat Input to Propellant Tank vs. Tank Angle

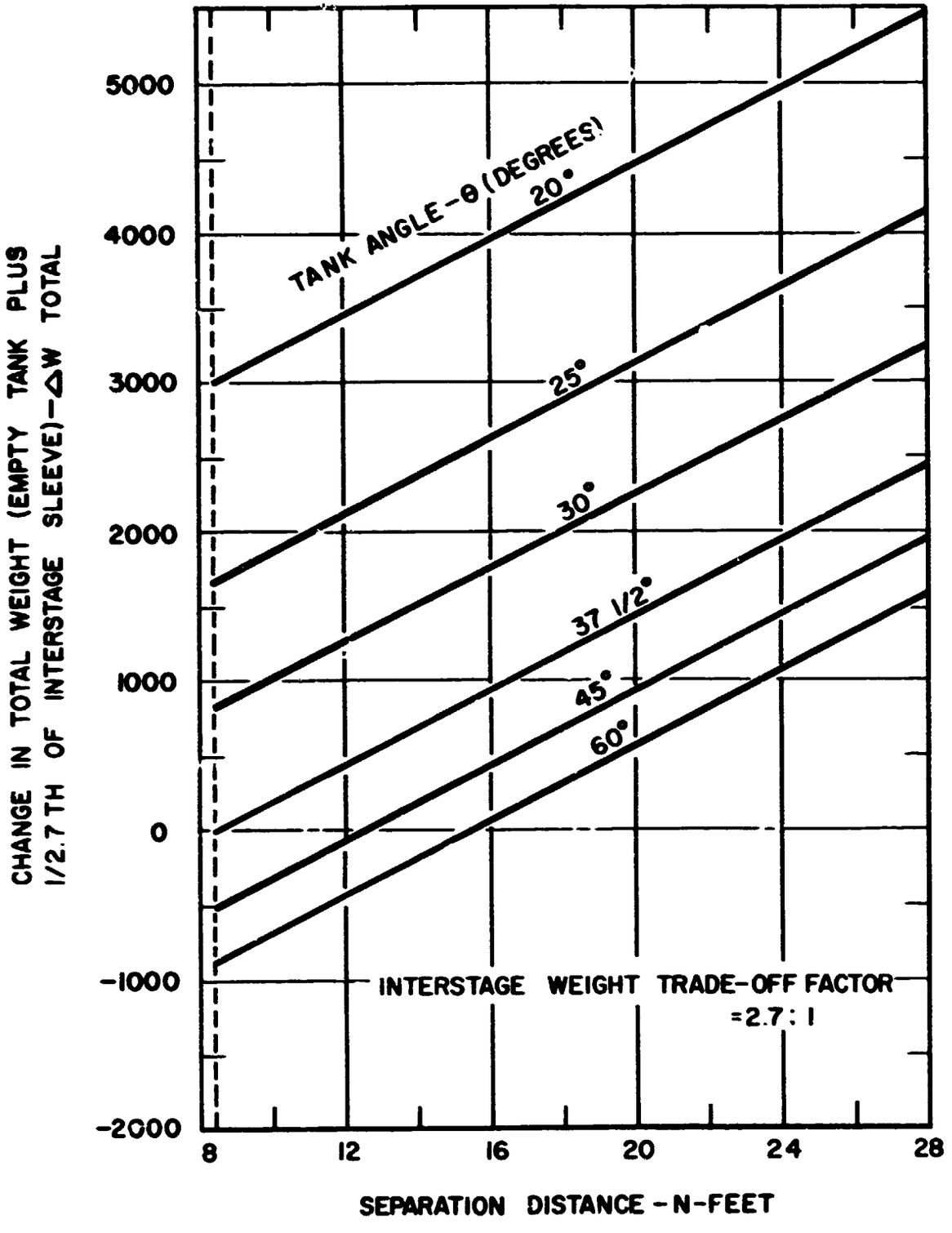

Figure 29 537622

Change in Total Weight vs. Separation Distance for Various Tank Angles

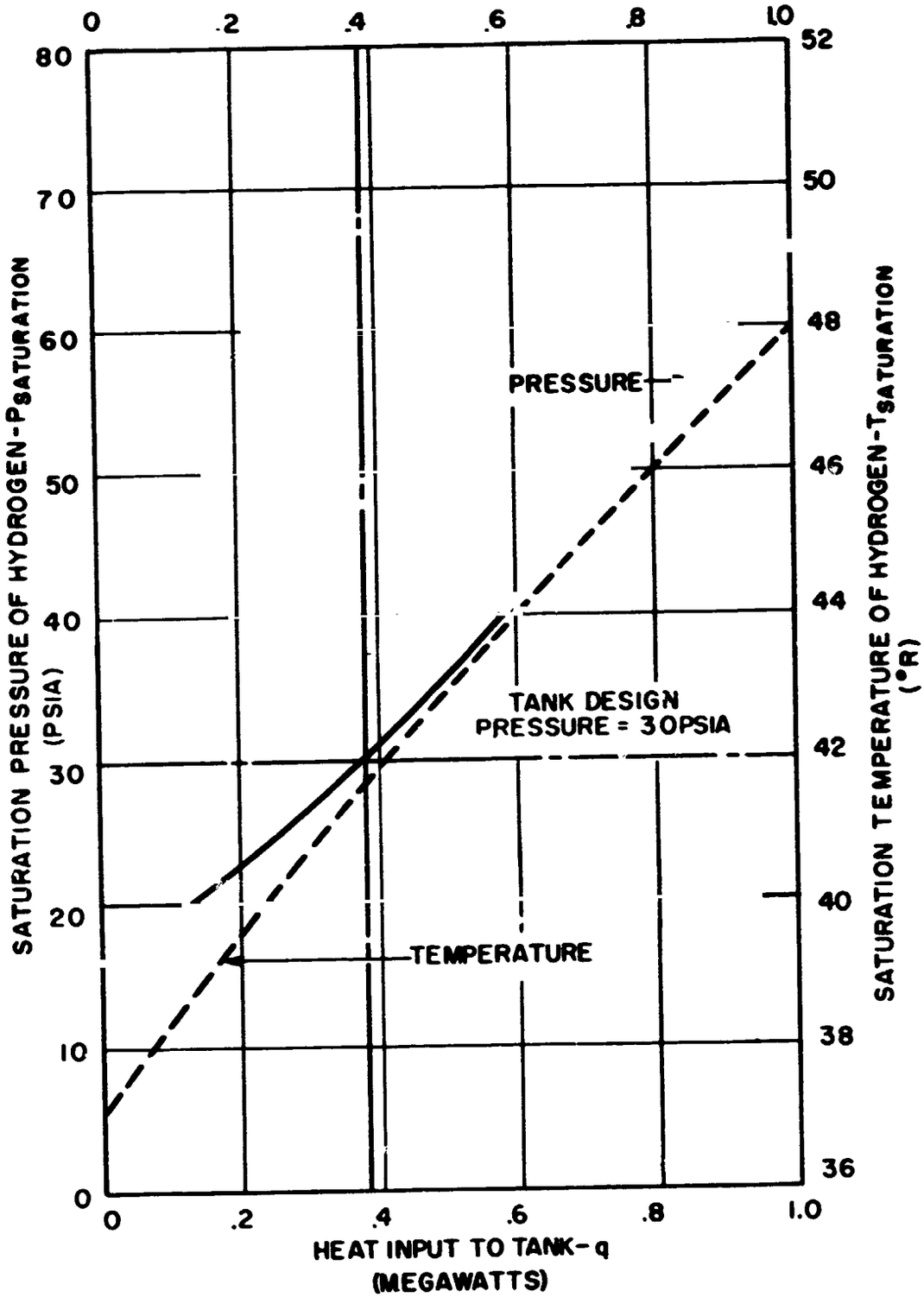

Figure 30

537624

Saturation Pressure vs. Tank Heat Input (Liquid Para-Hydrogen)

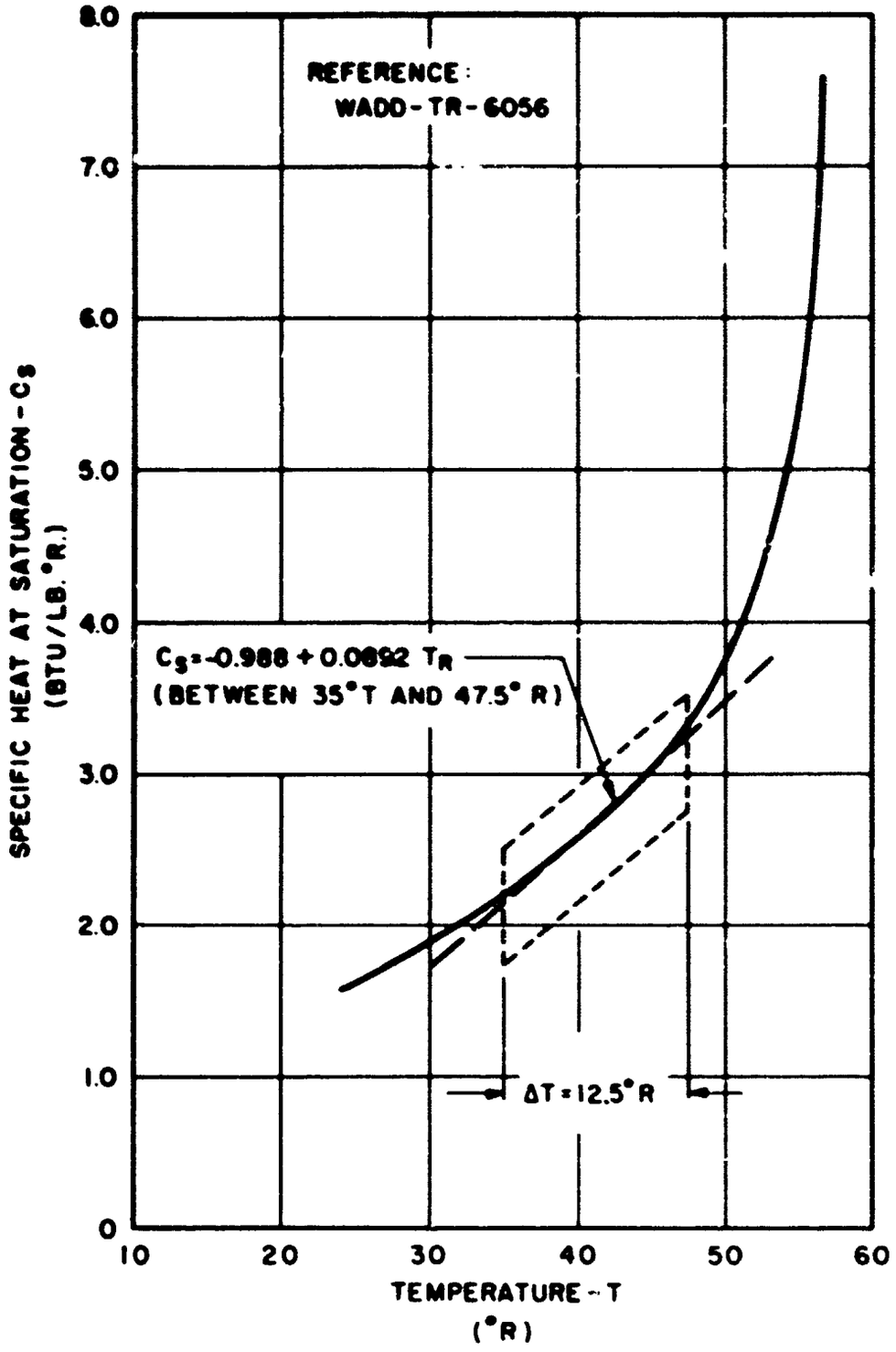

Figure 31 537625

Specific Heat at Saturation vs. Temperature for Liquid Para-Hydrogen

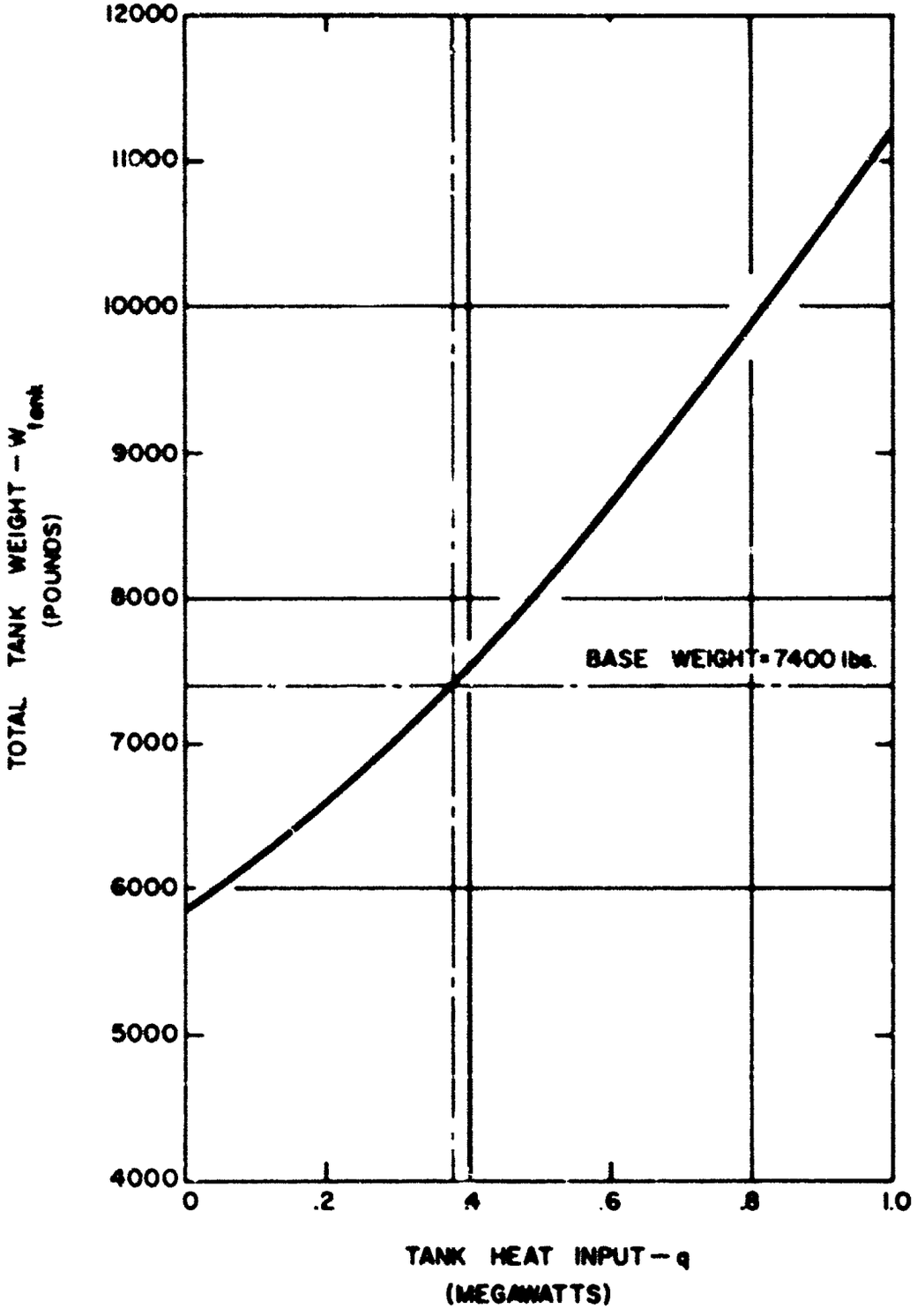

Figure 32 537627

Total Tank Weight vs. Tank Heat Input

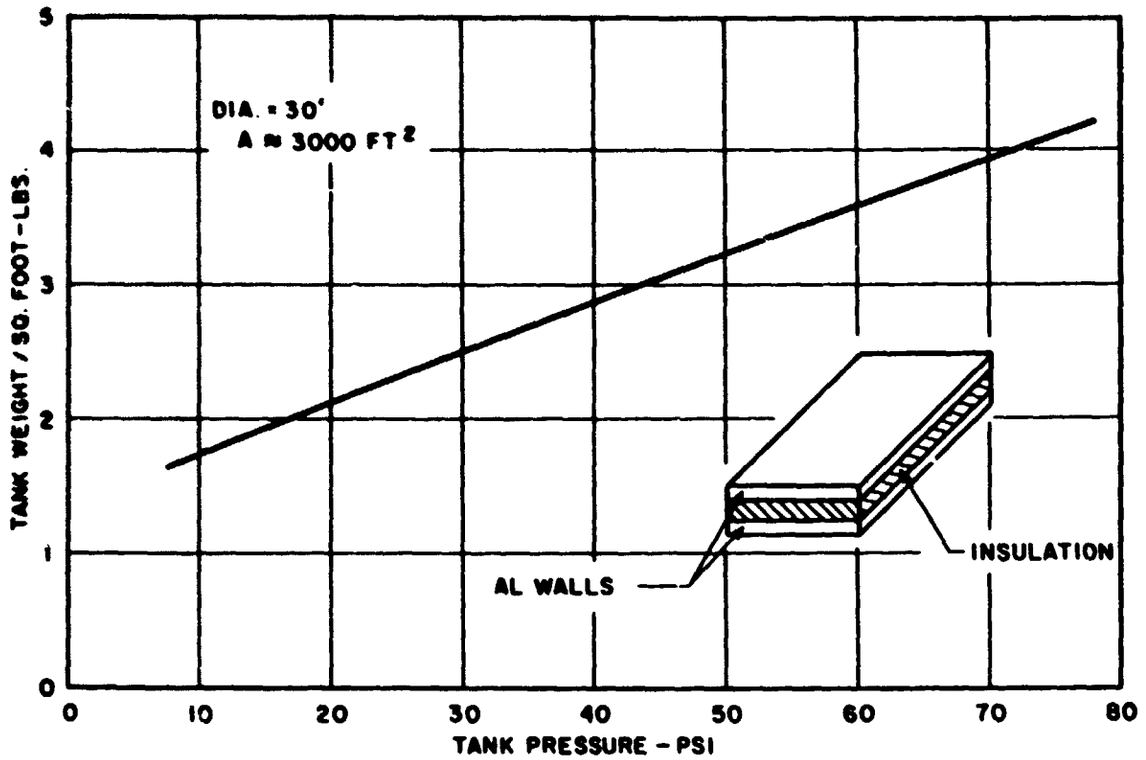

Figure 33 537626

Tank Wall wt/ft^2 of Surface vs. Tank Internal Pressure

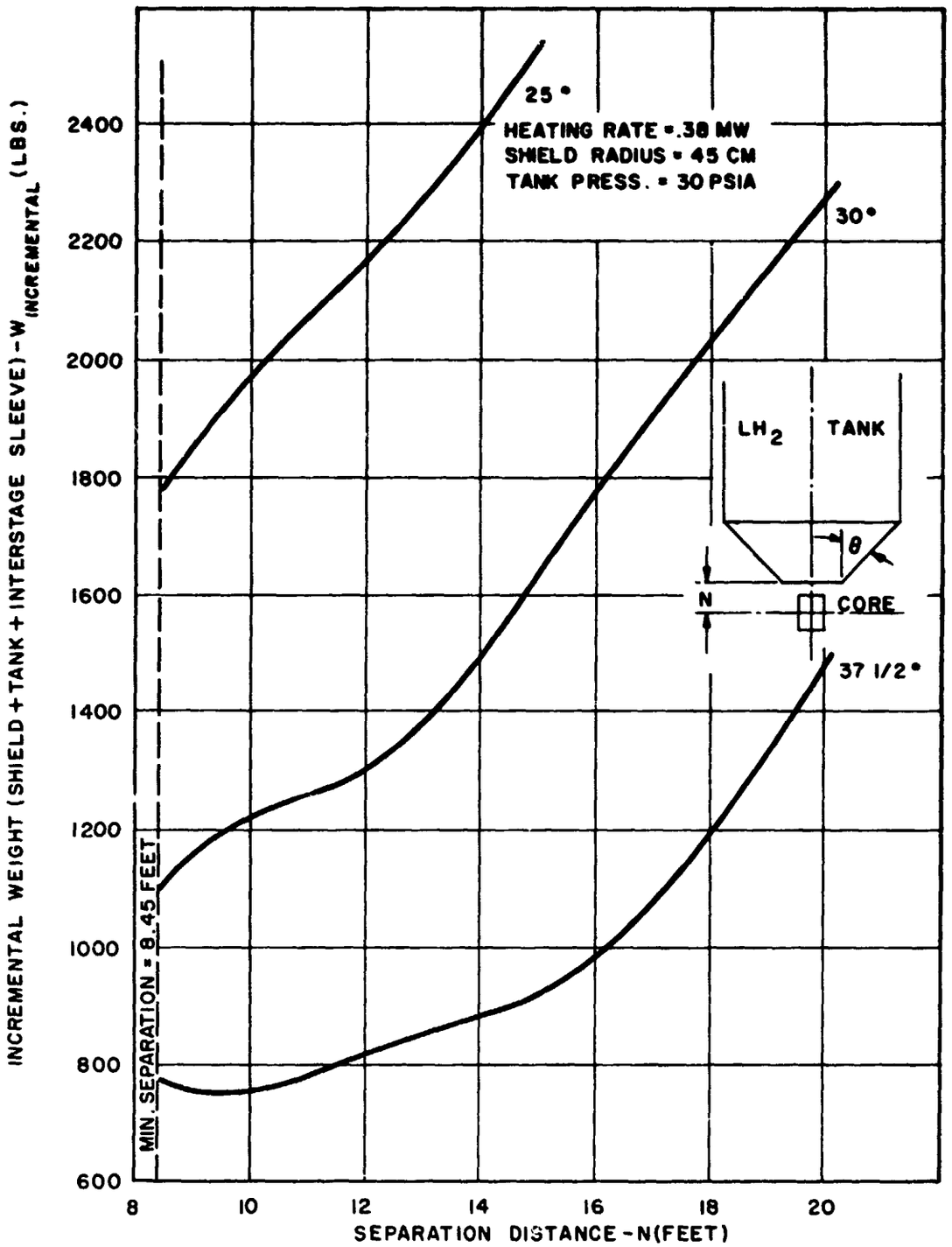

Figure 34 547196

System Weight vs. Tank - Core Separation for Several Tank Angles

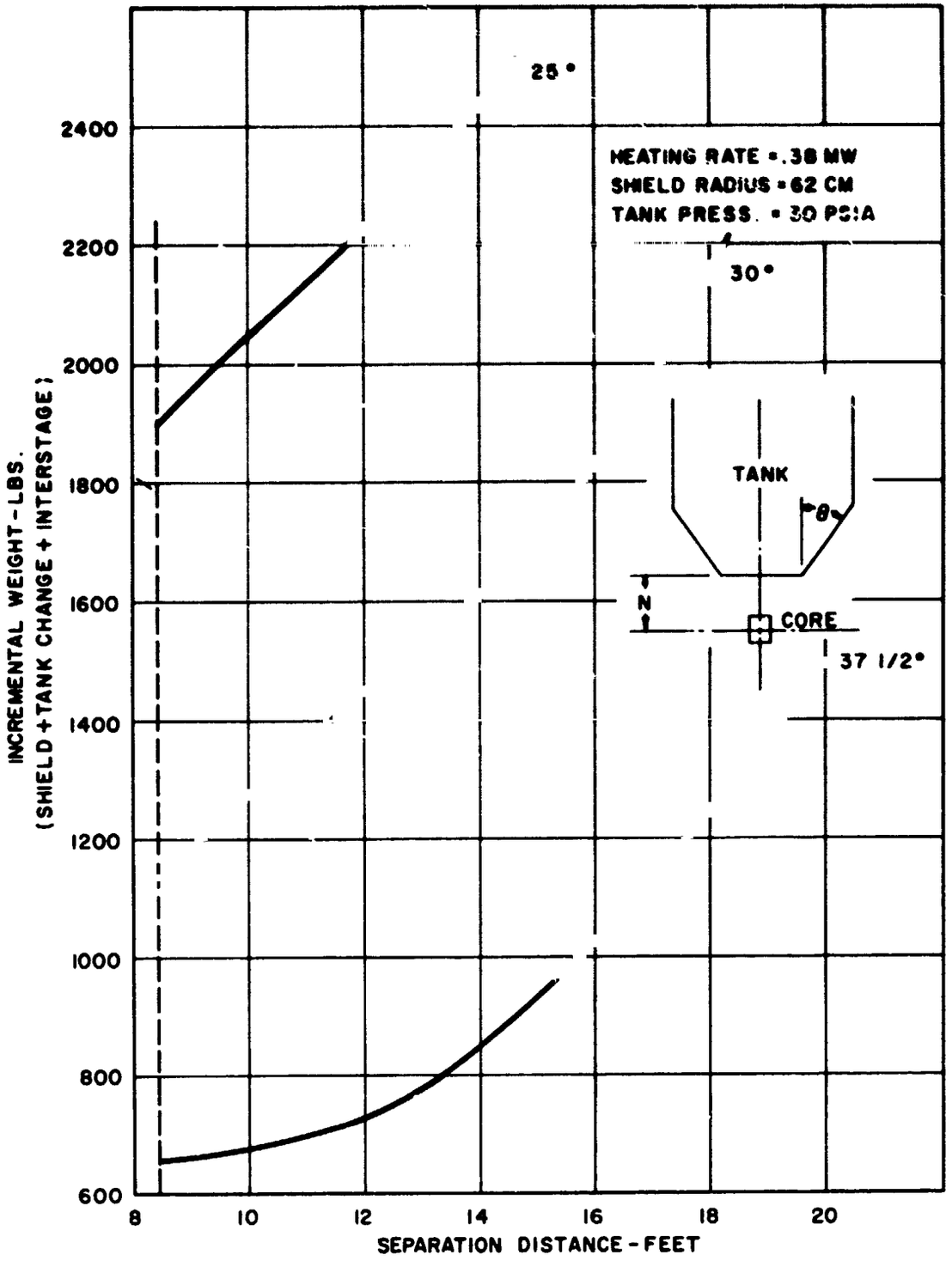

Figure 35 547197

System Weight vs. Tank – Core Separation for Several Tank Angles

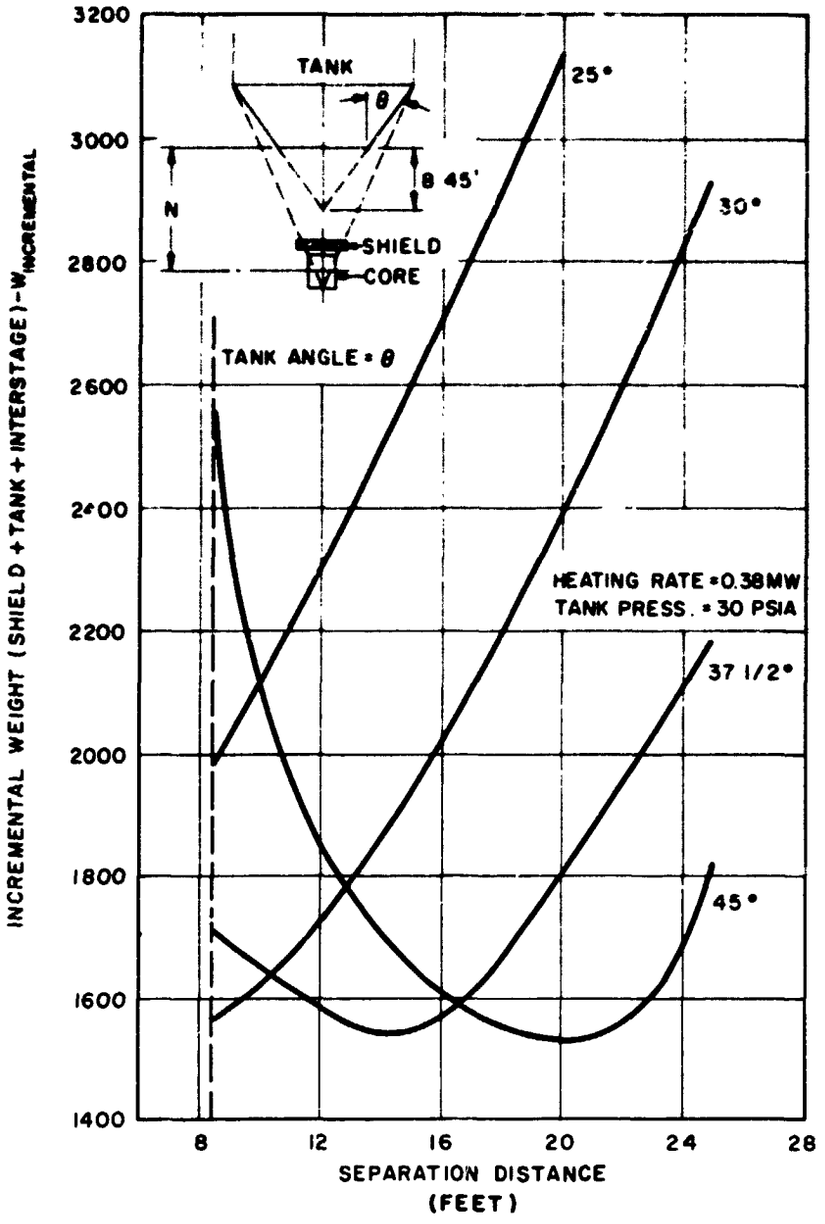

Figure 36

Total Weight vs. Separation Distance

547201

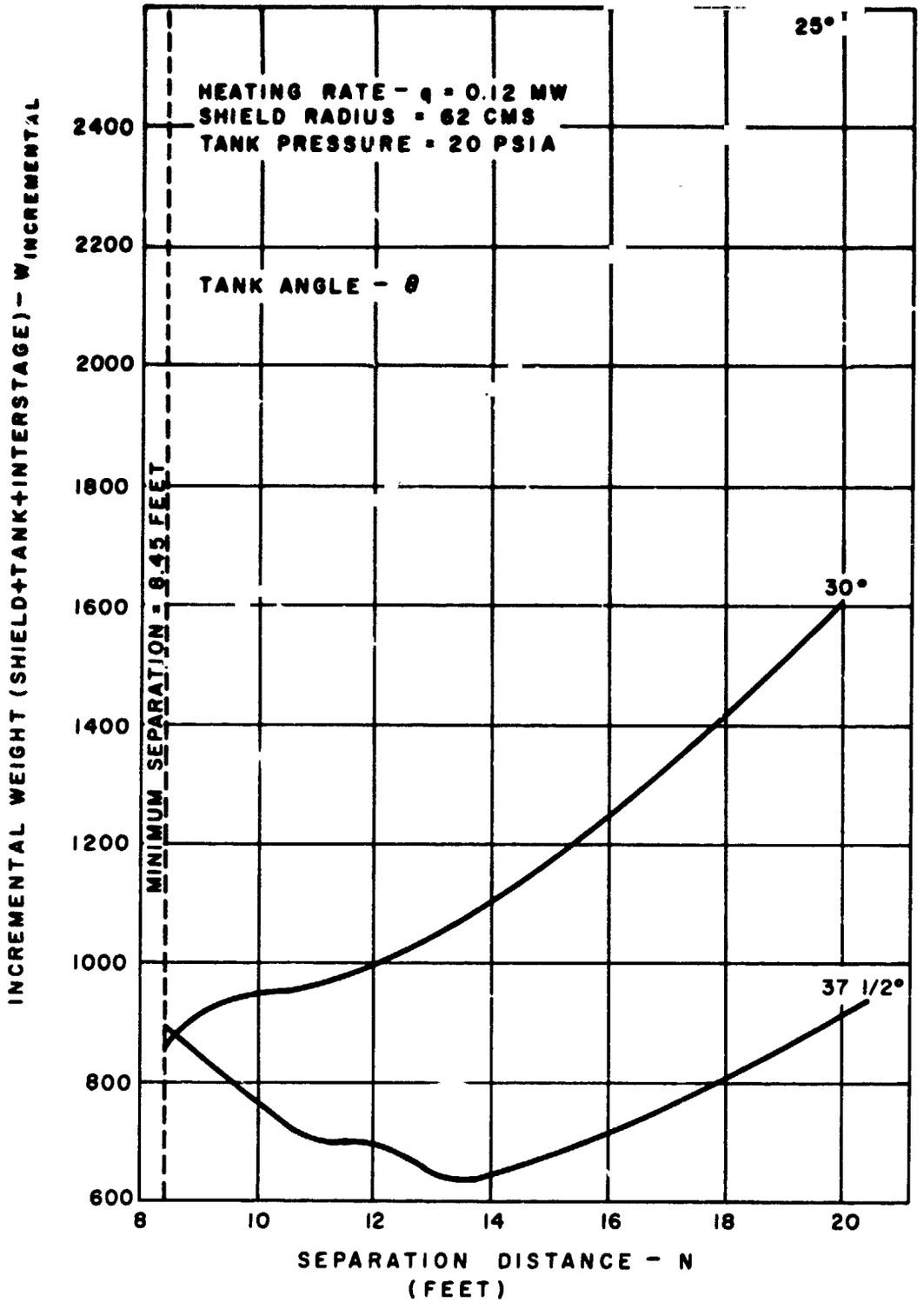

Figure 37 547198

System Weight vs. Tank - Core Separation

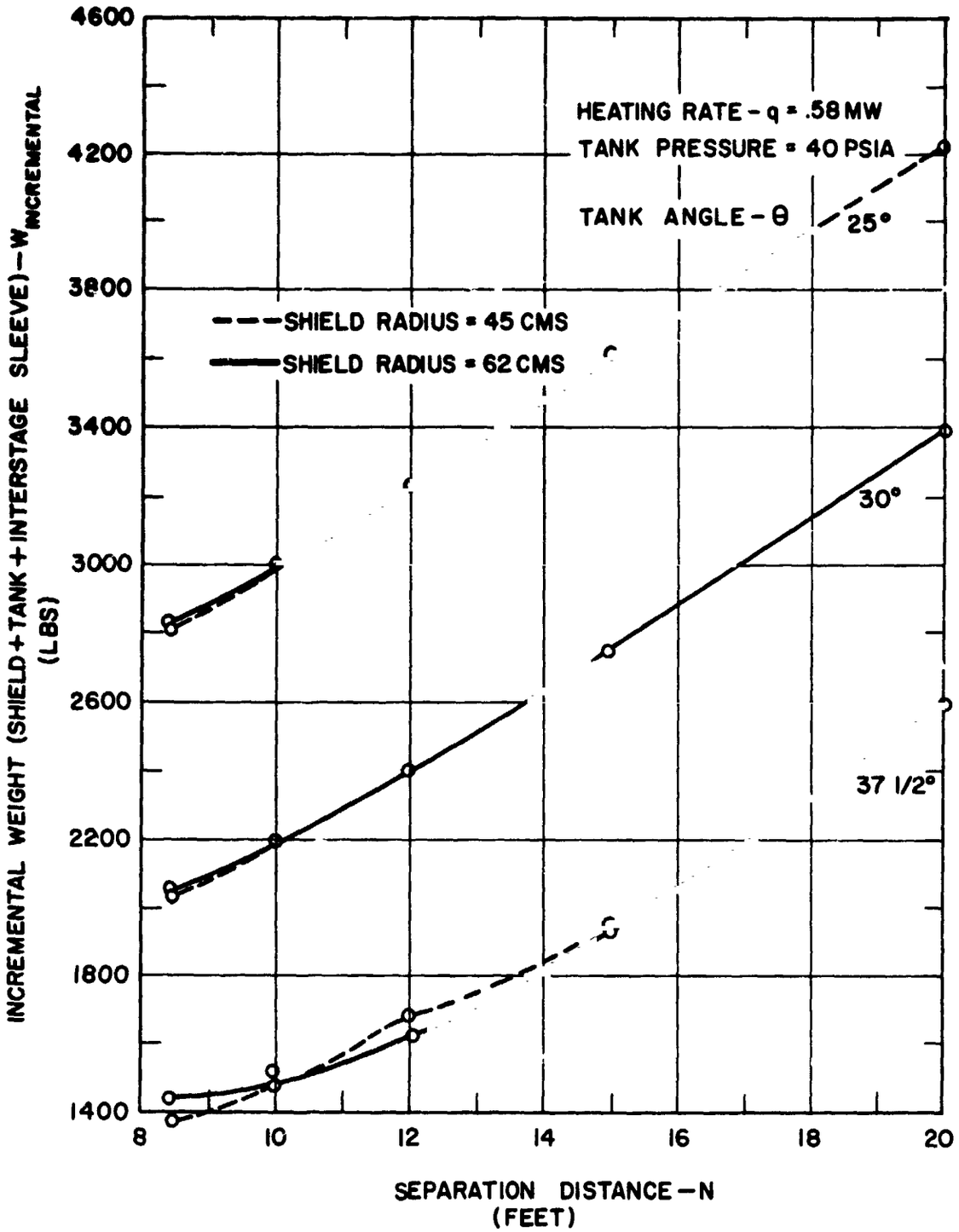

Figure 38

547199

System Weight vs. Tank - Core Separation

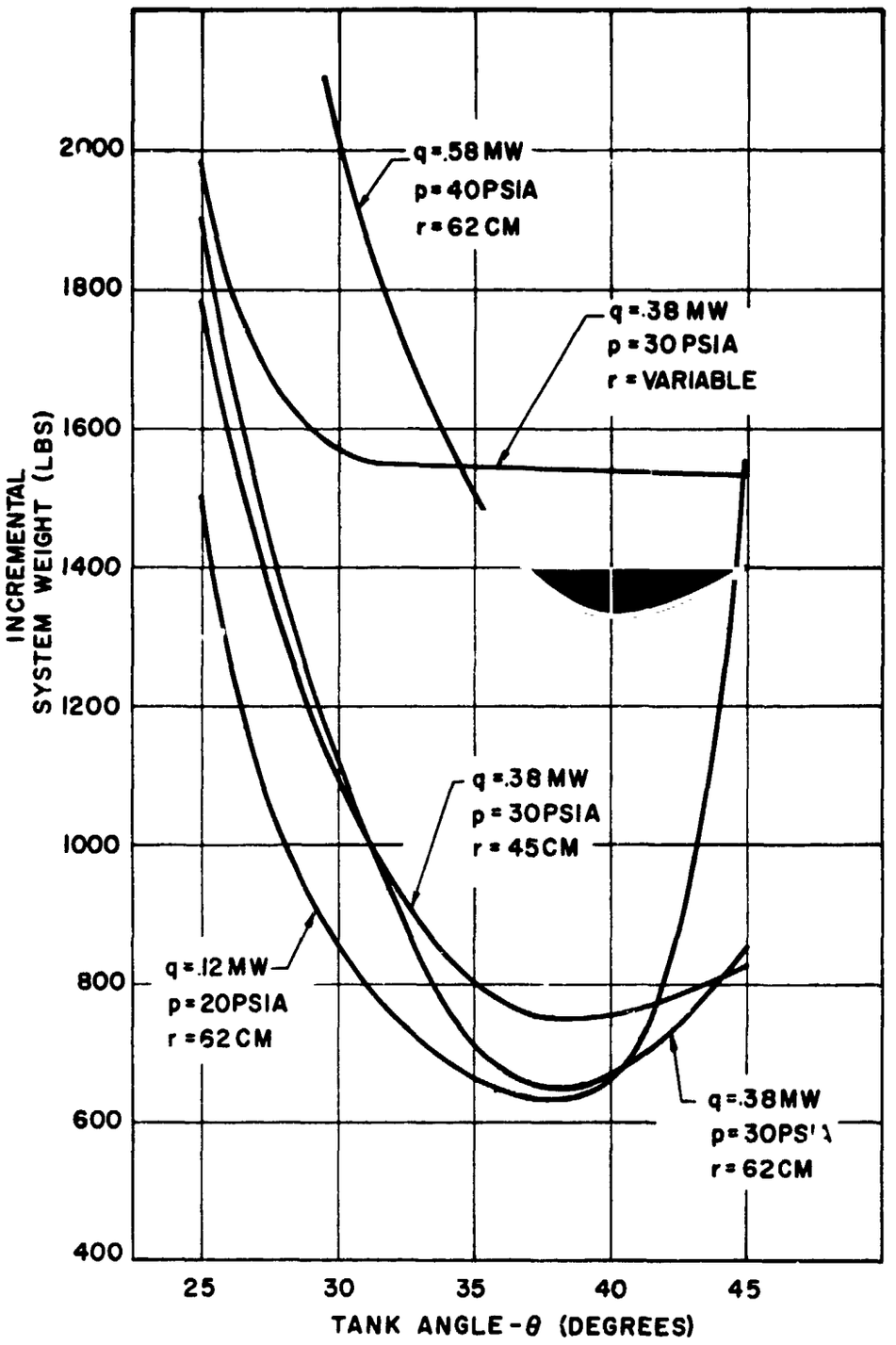

OPTIMUM TANK ANGLE - TANK ANGLE VS SYSTEM WEIGHT

Figure 39 547200

Optimum Tank Angle - Tank Angle vs. System Weight

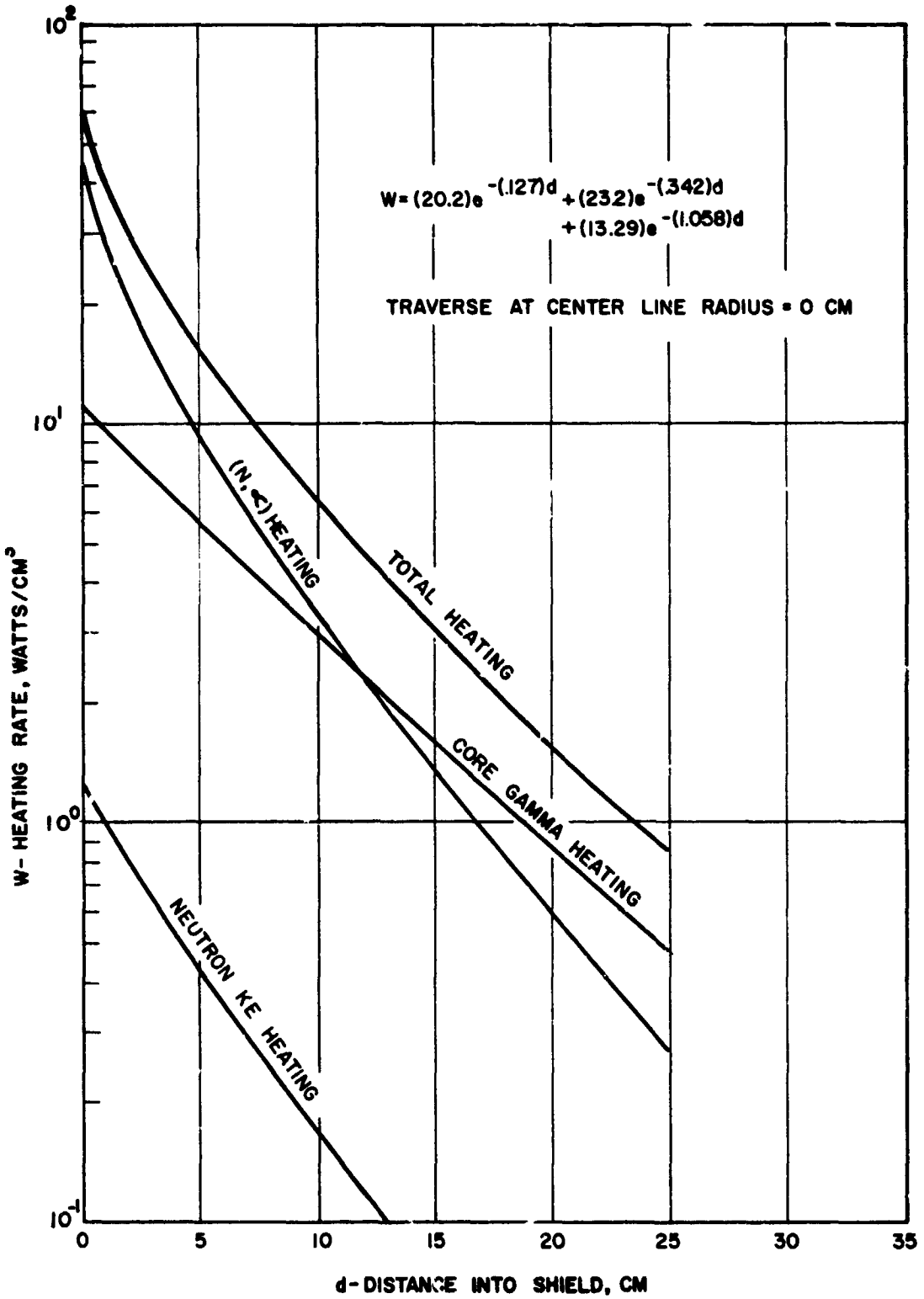

Figure 40 537606

Radiation Heating in Li H Shield (63% Li H, 27% Fe, 10% Void)

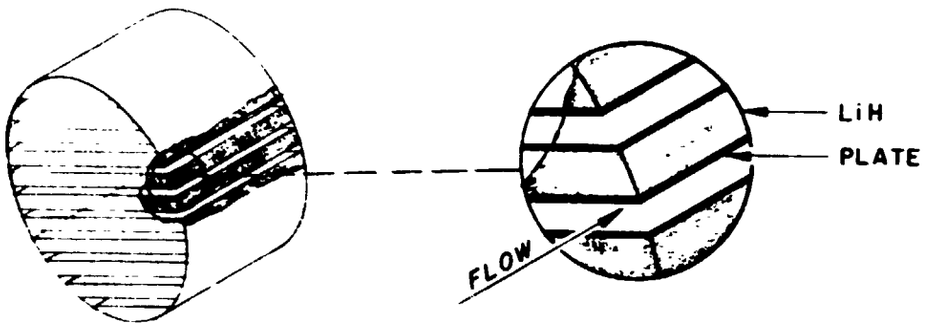

CONFIGURATION NO. 1

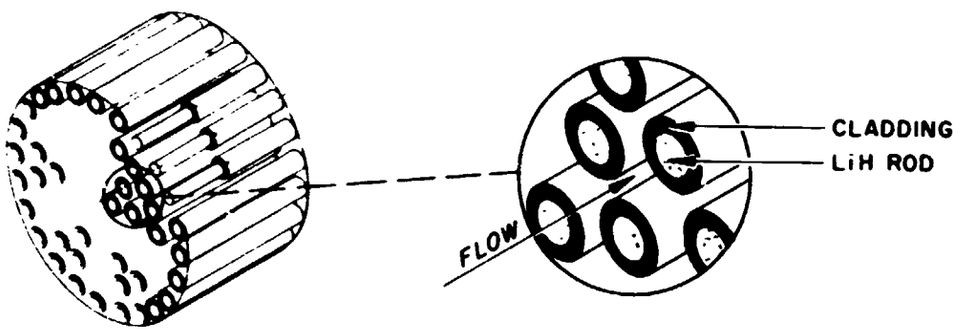

CONFIGURATION NO 2

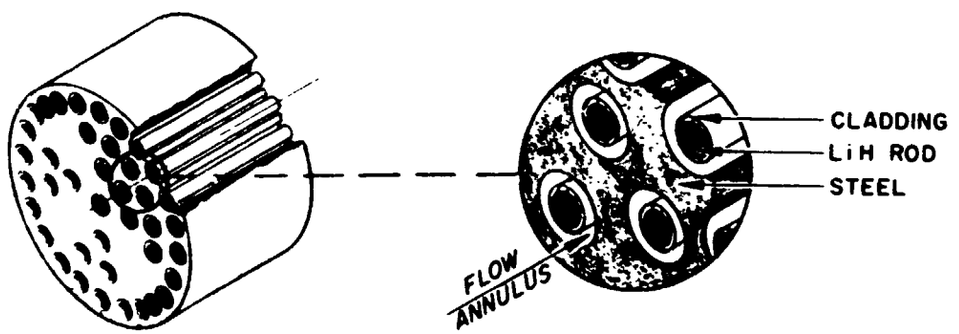

CONFIGURATION NO. 3

Figure 41 570A515

Shield Configurations Investigated

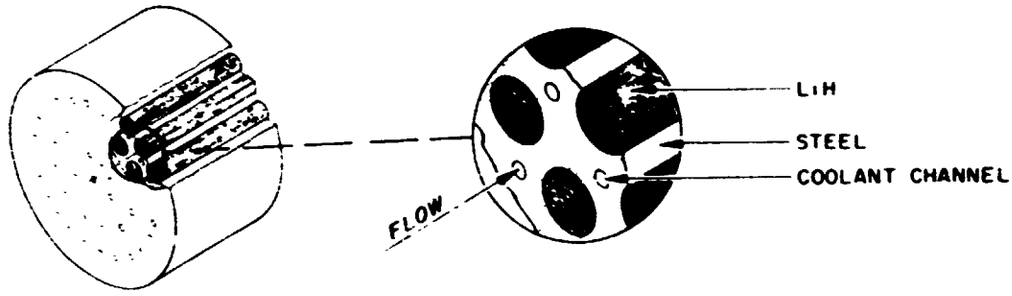

CONFIGURATION NO. 4

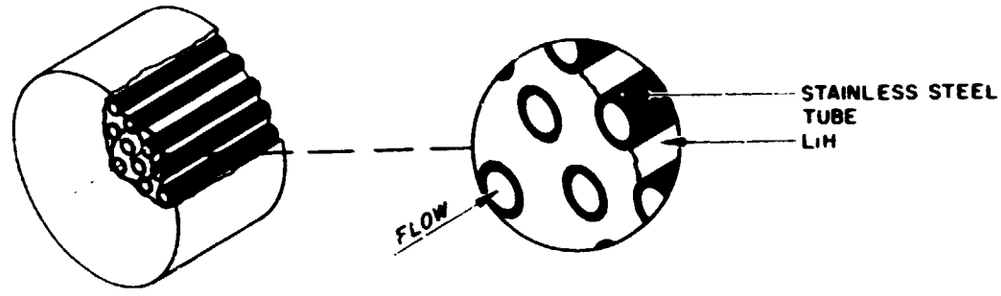

CONFIGURATION NO 5

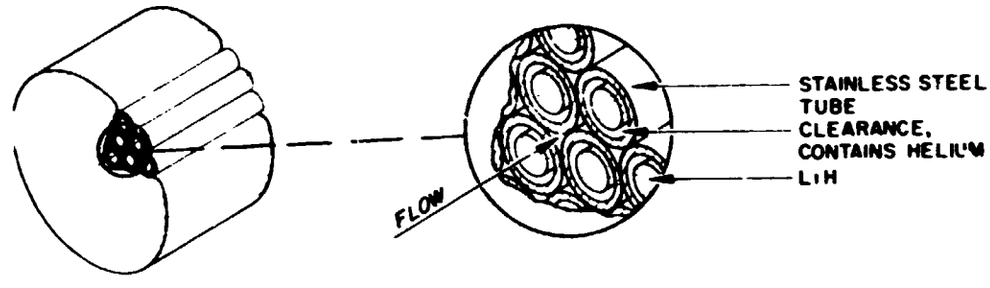

CONFIGURATION NO 6

SHIELD CONFIGURATIONS INVESTIGATED

Figure 42 570A616

Shield Configurations Investigated

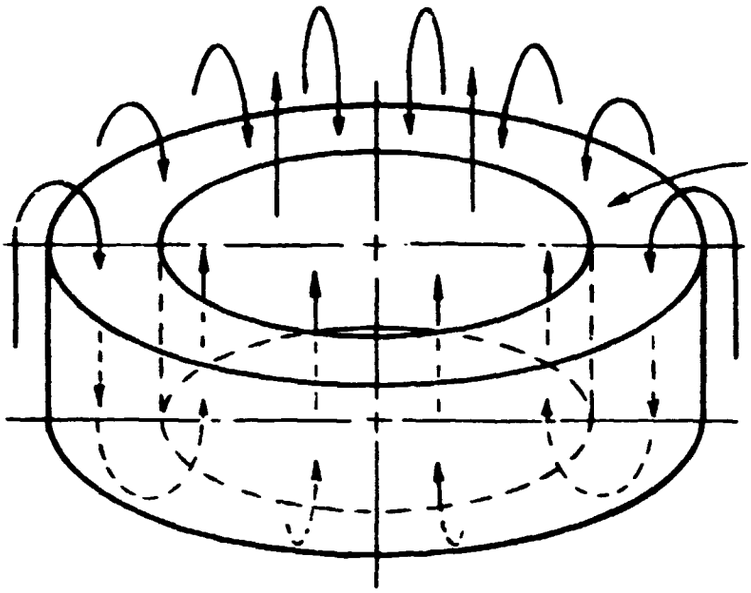

DOUBLE PASS DESIGN
(BOTH PASSES HAVE EQUAL
FLOW AREAS)

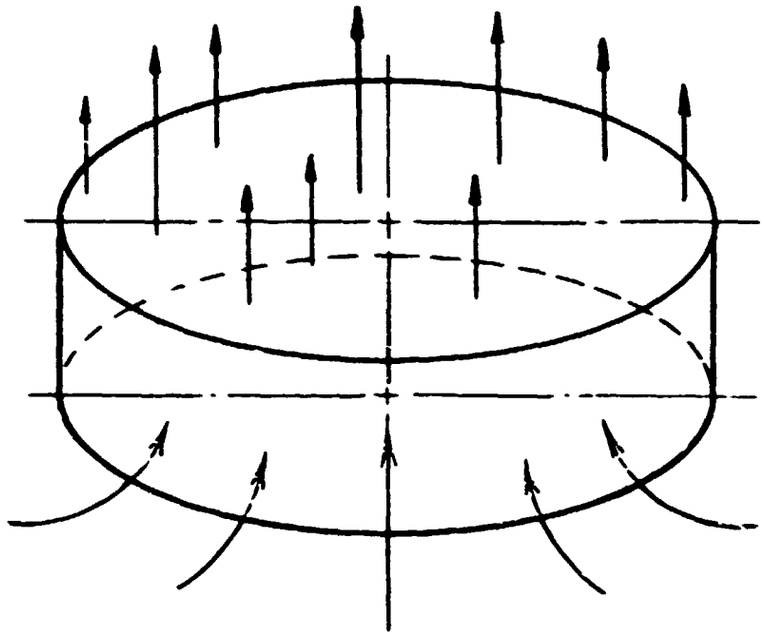

SINGLE PASS DESIGN

Figure 43 570A625

Schematic of Shield Double and Single Pass Arrangements

Astronuclear

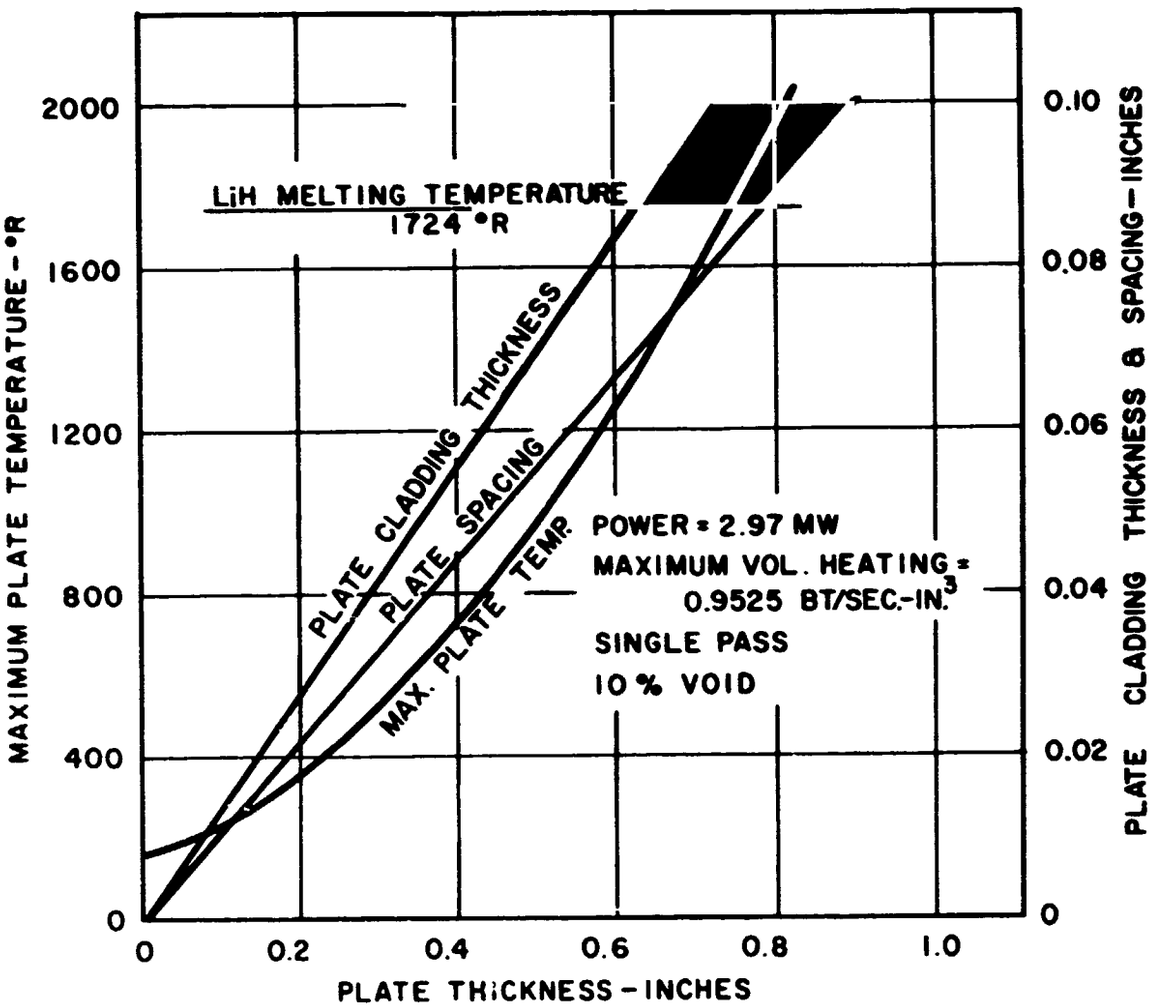

Figure 44

537402

Characteristics of Shield Configuration No. 1

Astronuclear

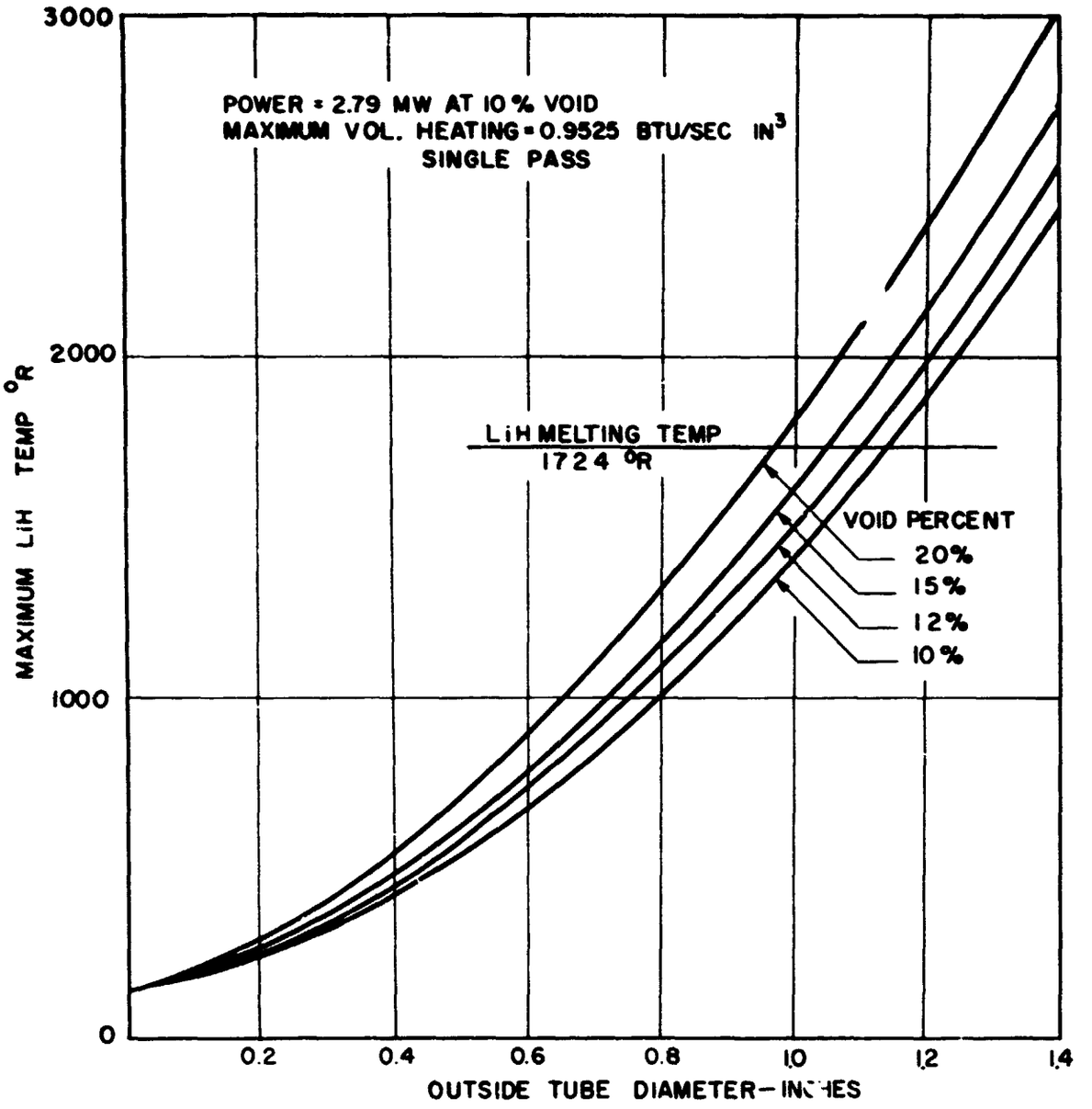

Figure 45 537403

Maximum Temperature Characteristics of Shield Configuration No. 2 - Single Pass

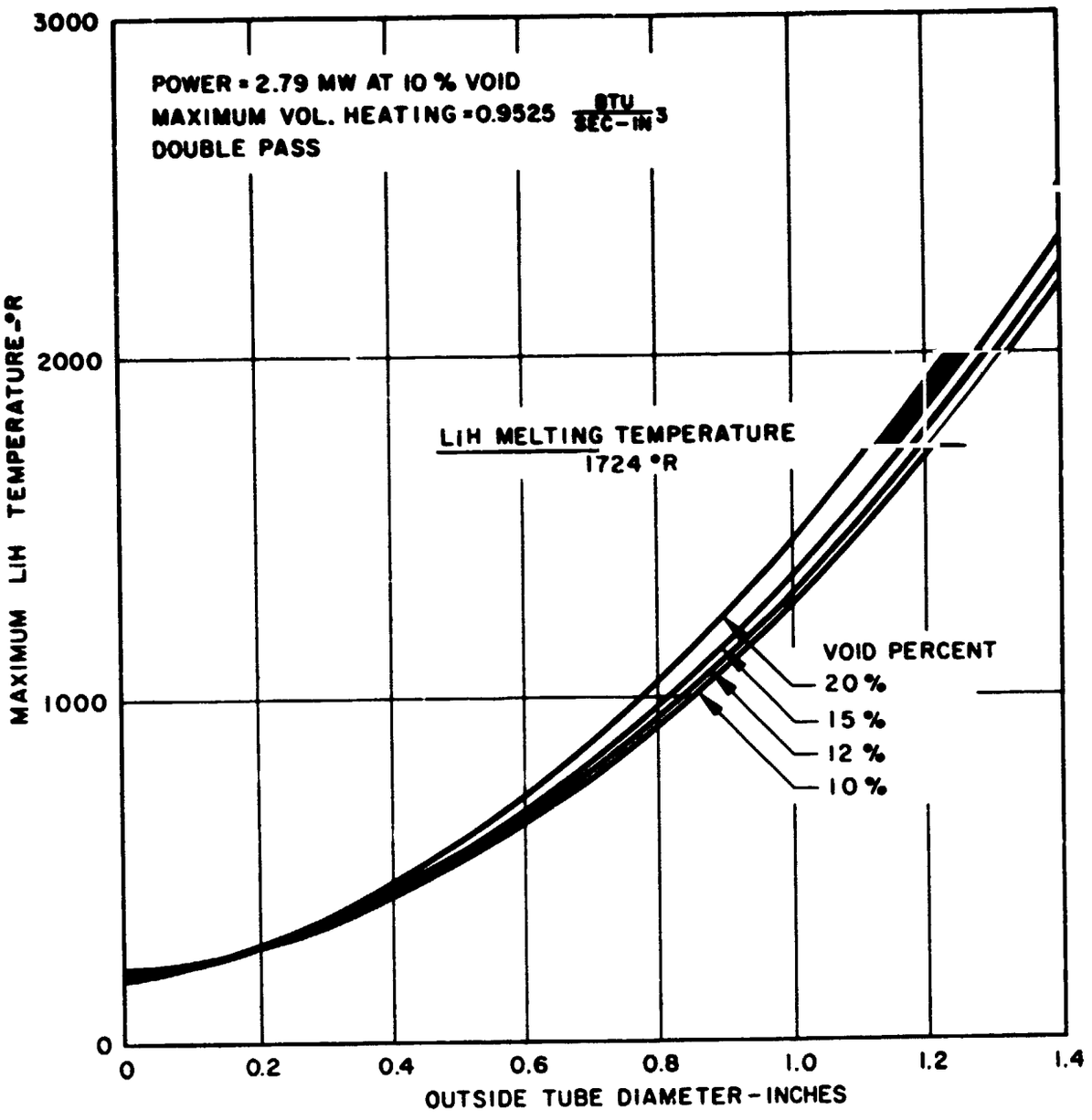

Figure 46 537404

Maximum Temperature Characteristics of Shield Configuration No. 2 Double Pass

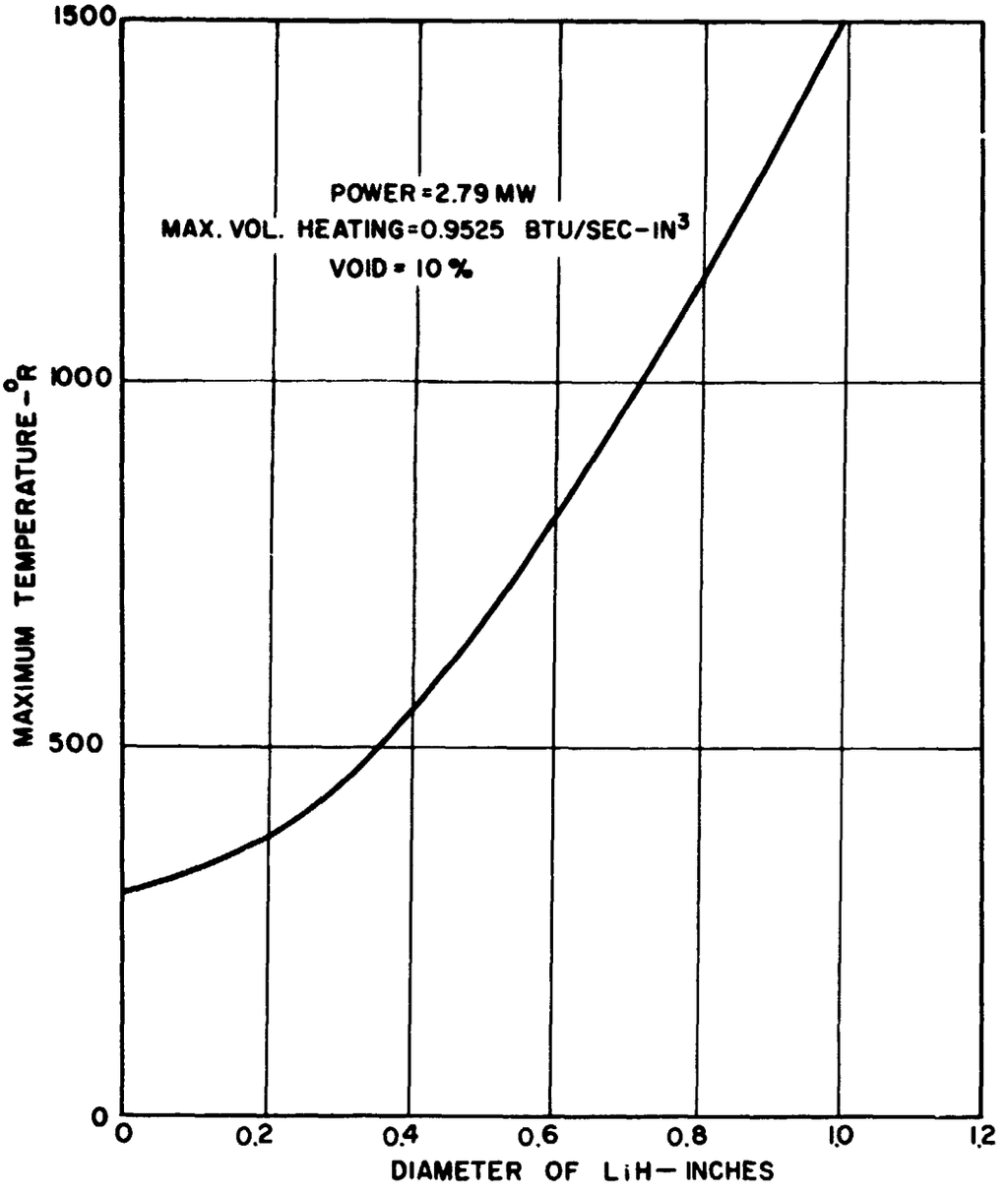

Figure 47 537406

Maximum Temperature Characteristics of Shield Configuration No. 3

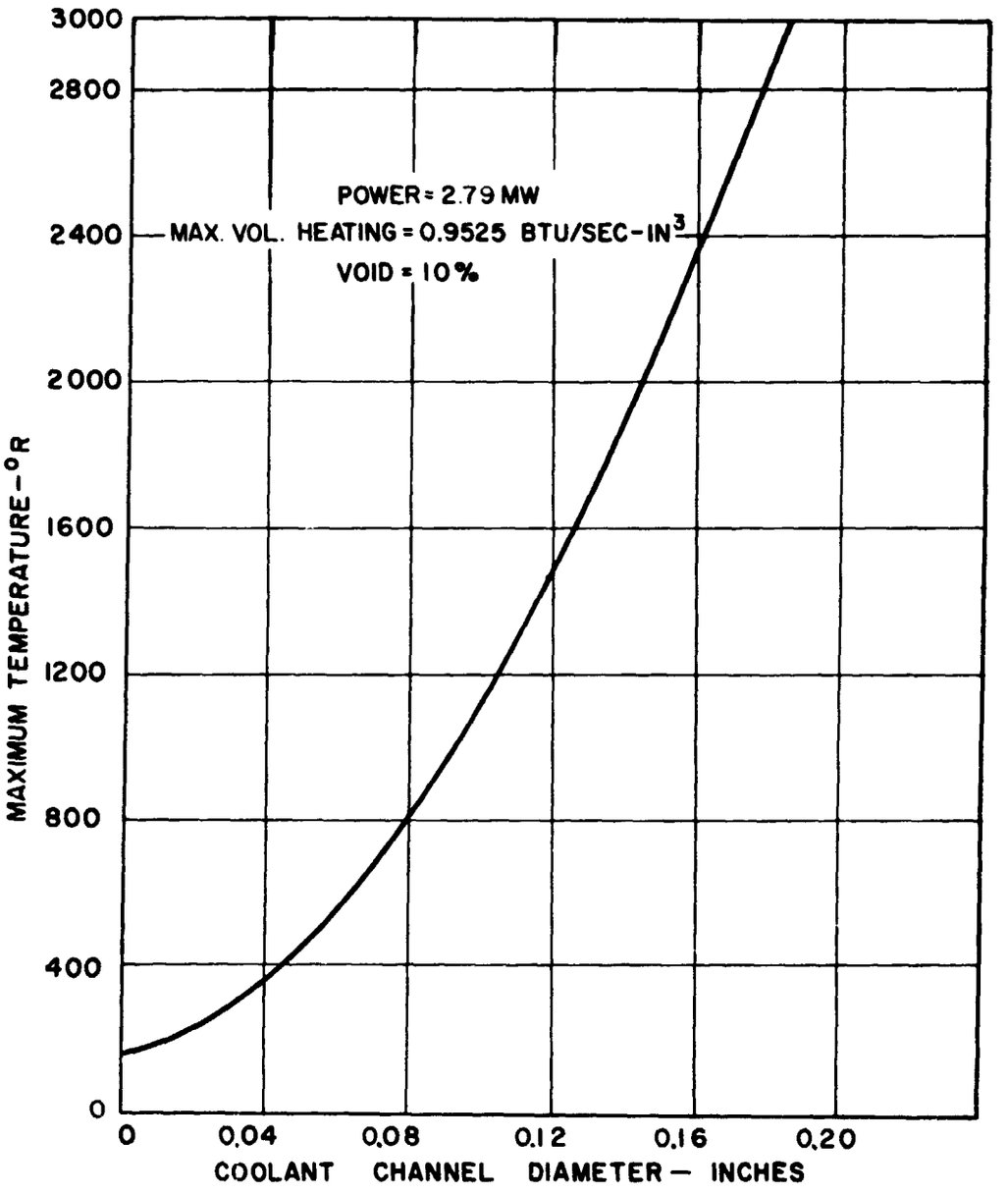

Figure 48 537407
Maximum Temperature Characteristics of Shield Configuration No. 4 Hexagonal Coolant Channel Array

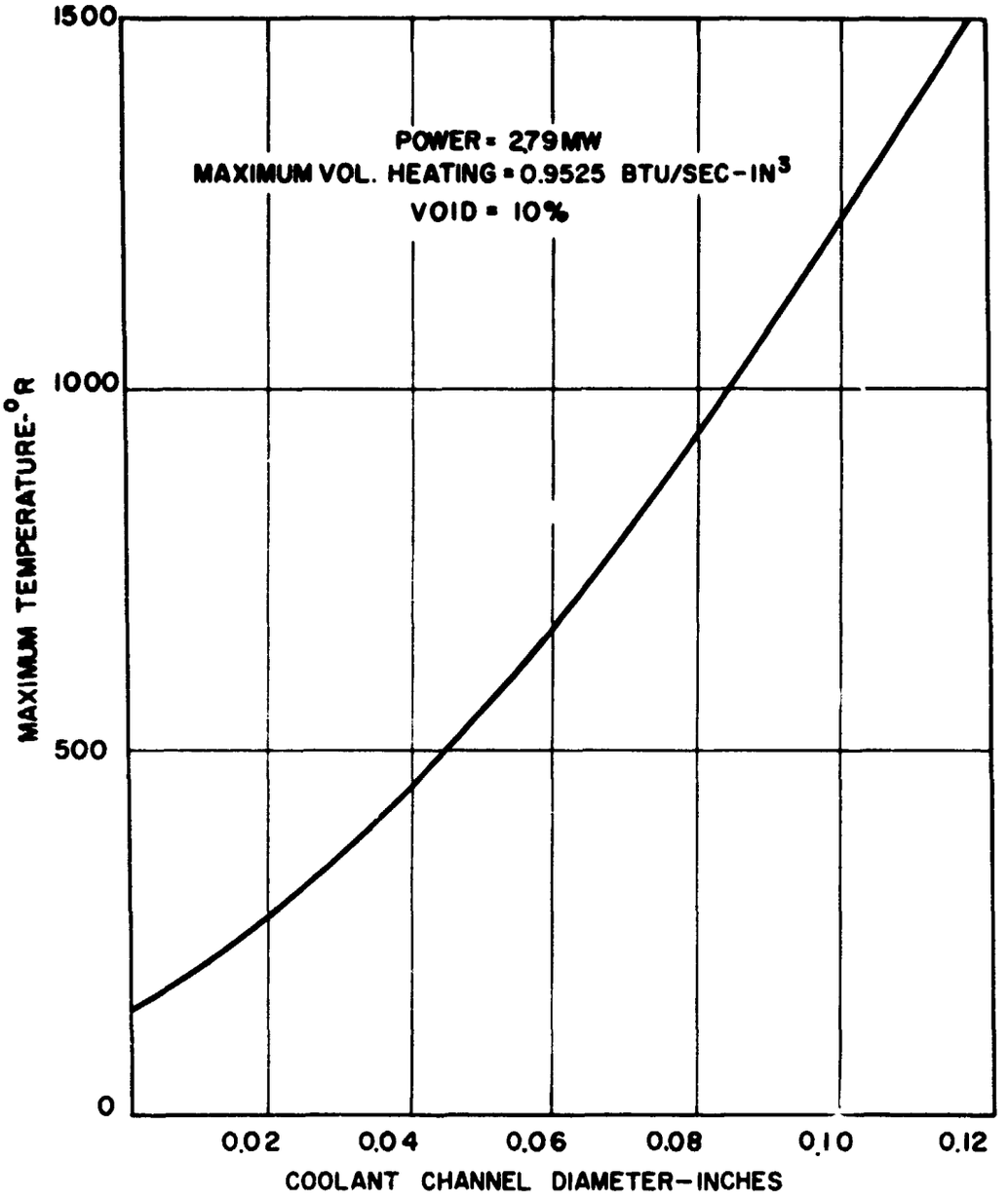

Figure 49 537408

Maximum Temperature Characteristics of Shield Configuration No. 5

Astronuclear

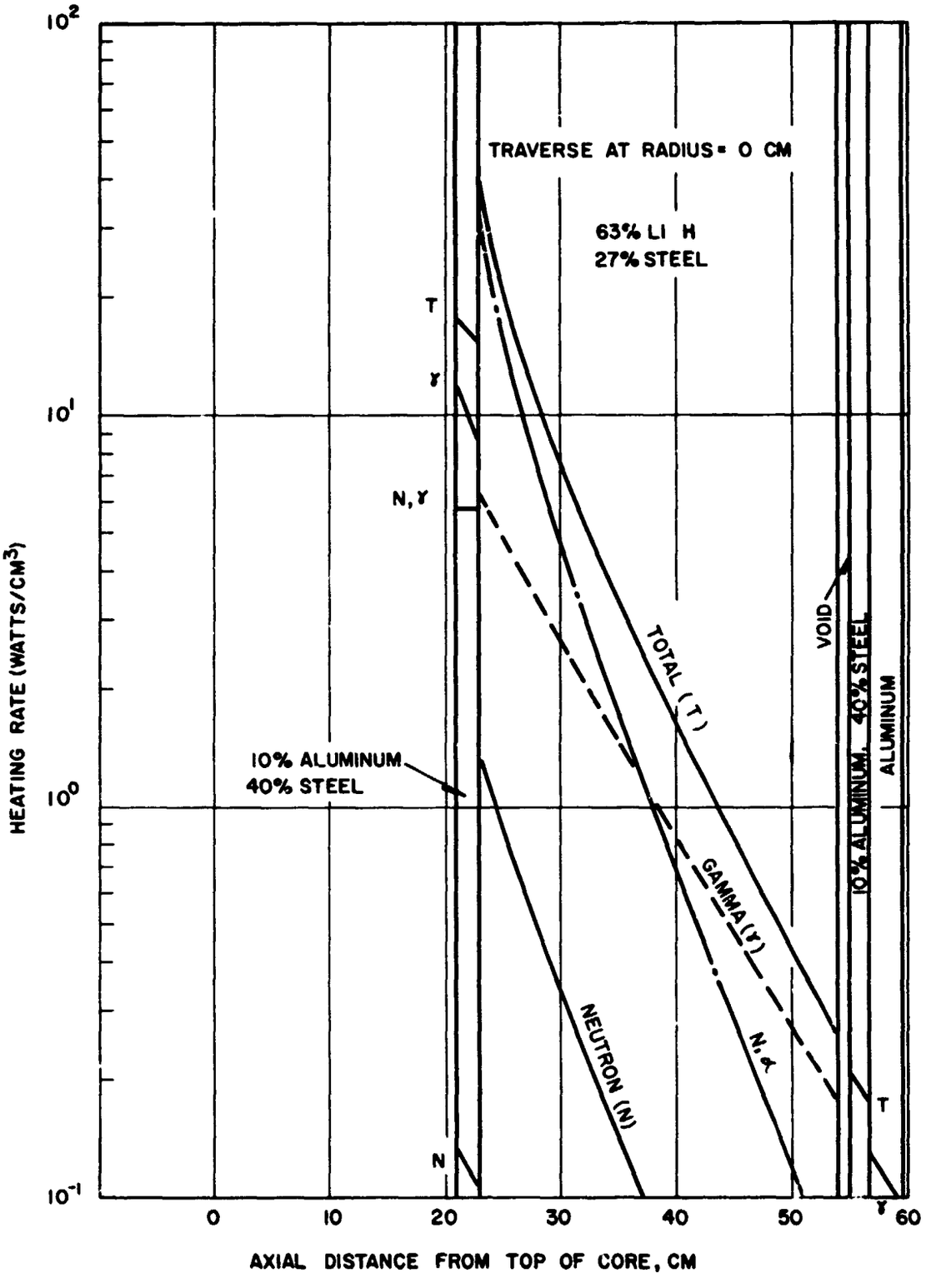

Figure 50

547016

Radiation Heating in Shield - 0 Cm. Radius

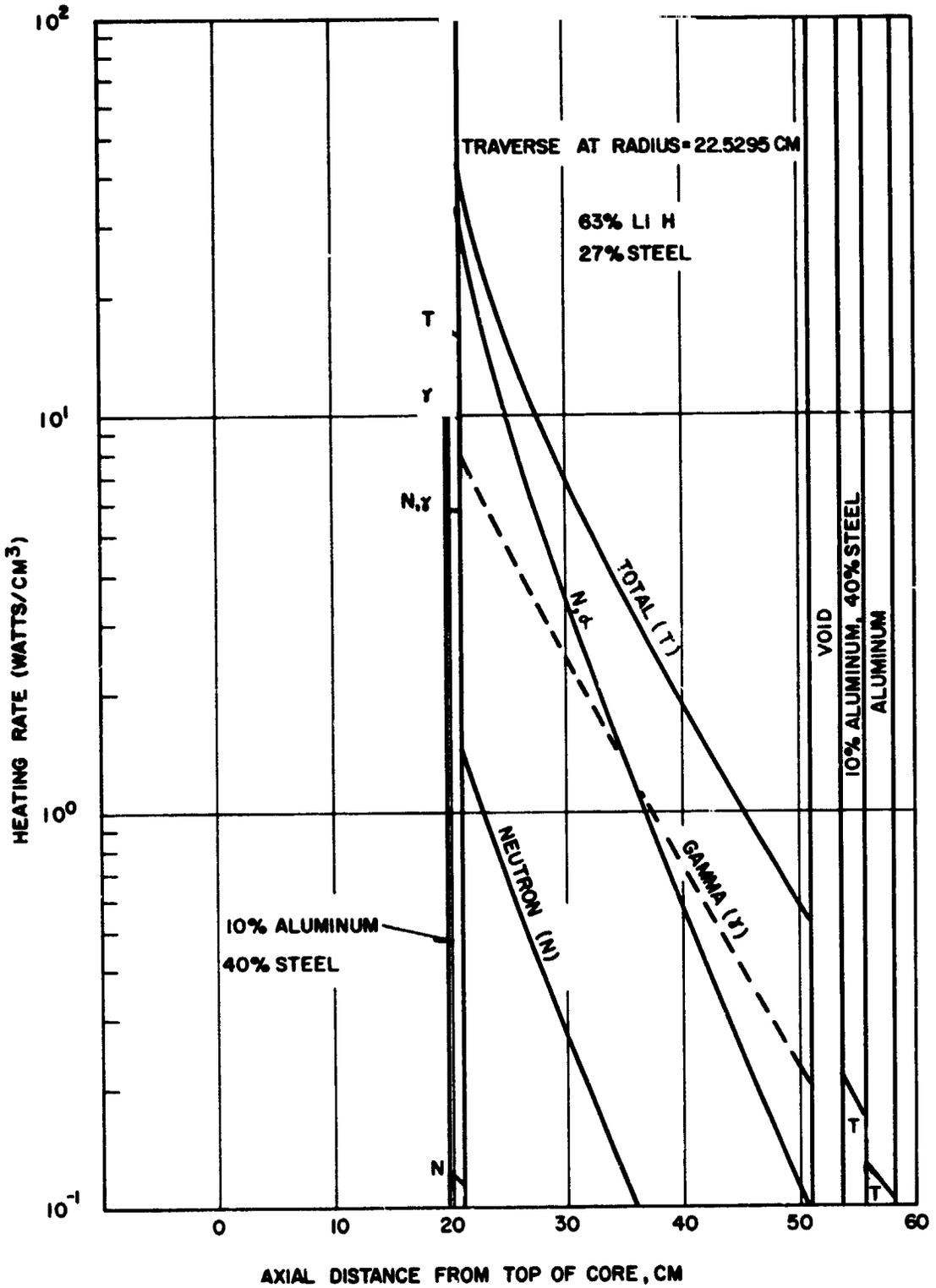

Figure 51

547017

Radiation Heating in Shield - 22.5 Cm Radius

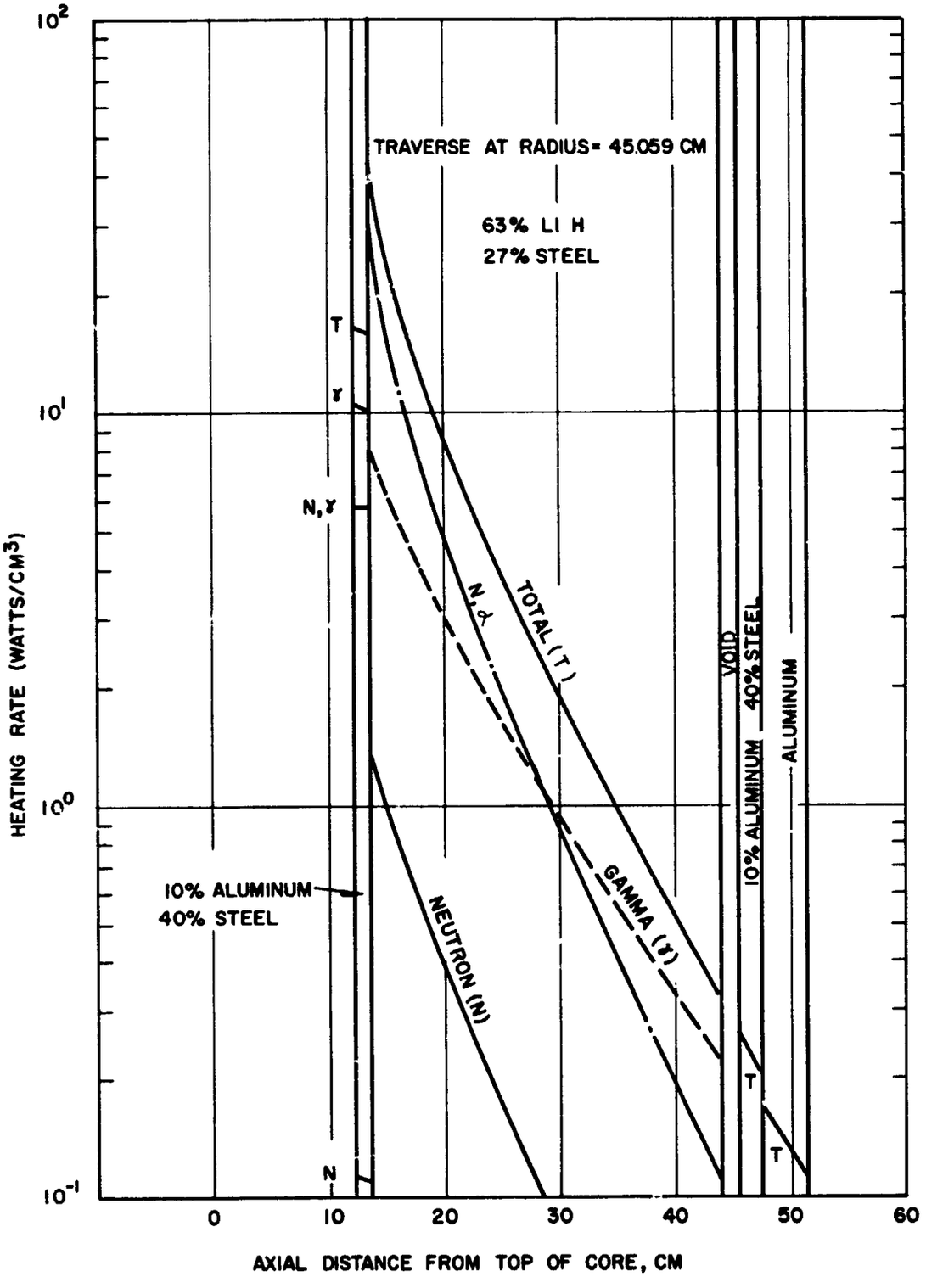

Figure 52

547015

Radiation Heating in Shield - 45.0 Cm Radius

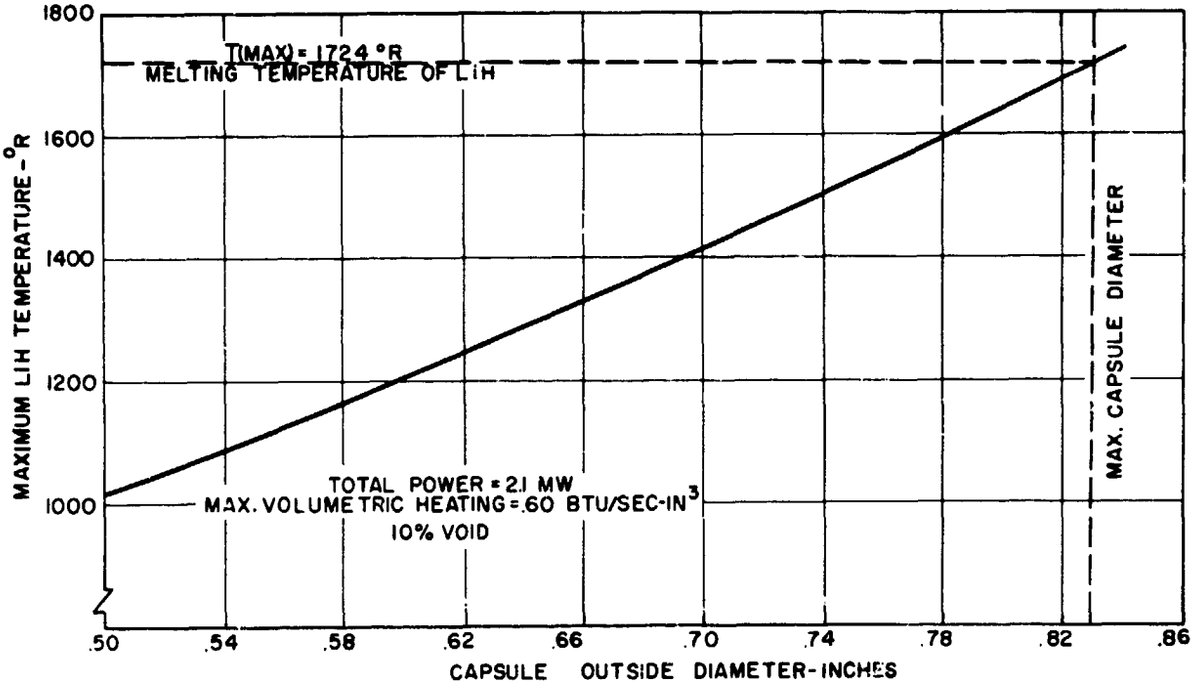

Figure 53 537409
Maximum Lithium Hydride Temperature as a Function of Capsule Diameter-Heated Bleed Cycle

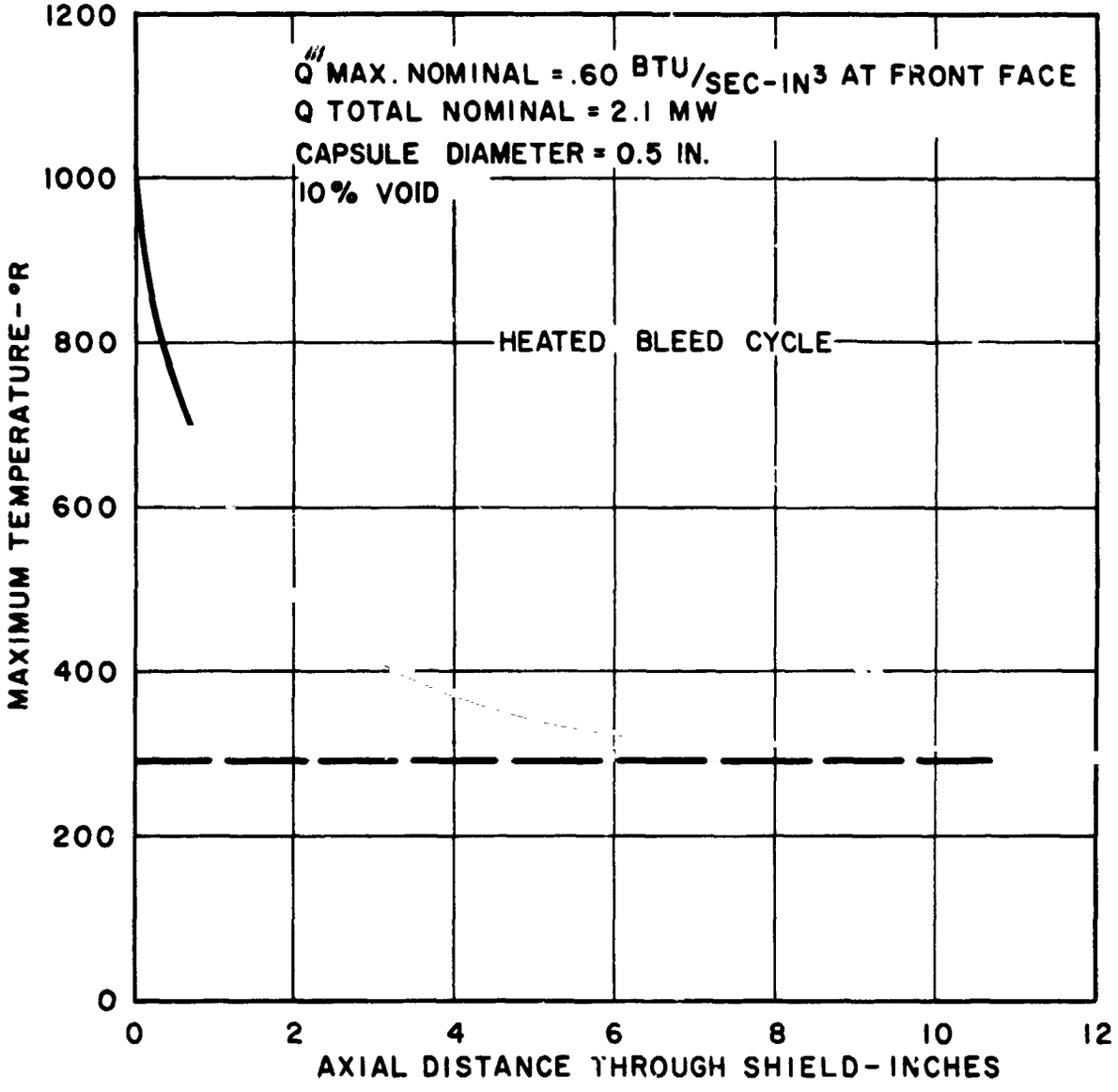

MAXIMUM LITHIUM HYDRIDE TEMPERATURE AS A FUNCTION OF DISTANCE

INTO THE SHIELD - HEATED BLEED CYCLE

Figure 54 537410
Maximum Lithium Hydride Temperature as a Function of Distance into the Shield-Heated Bleed Cycle

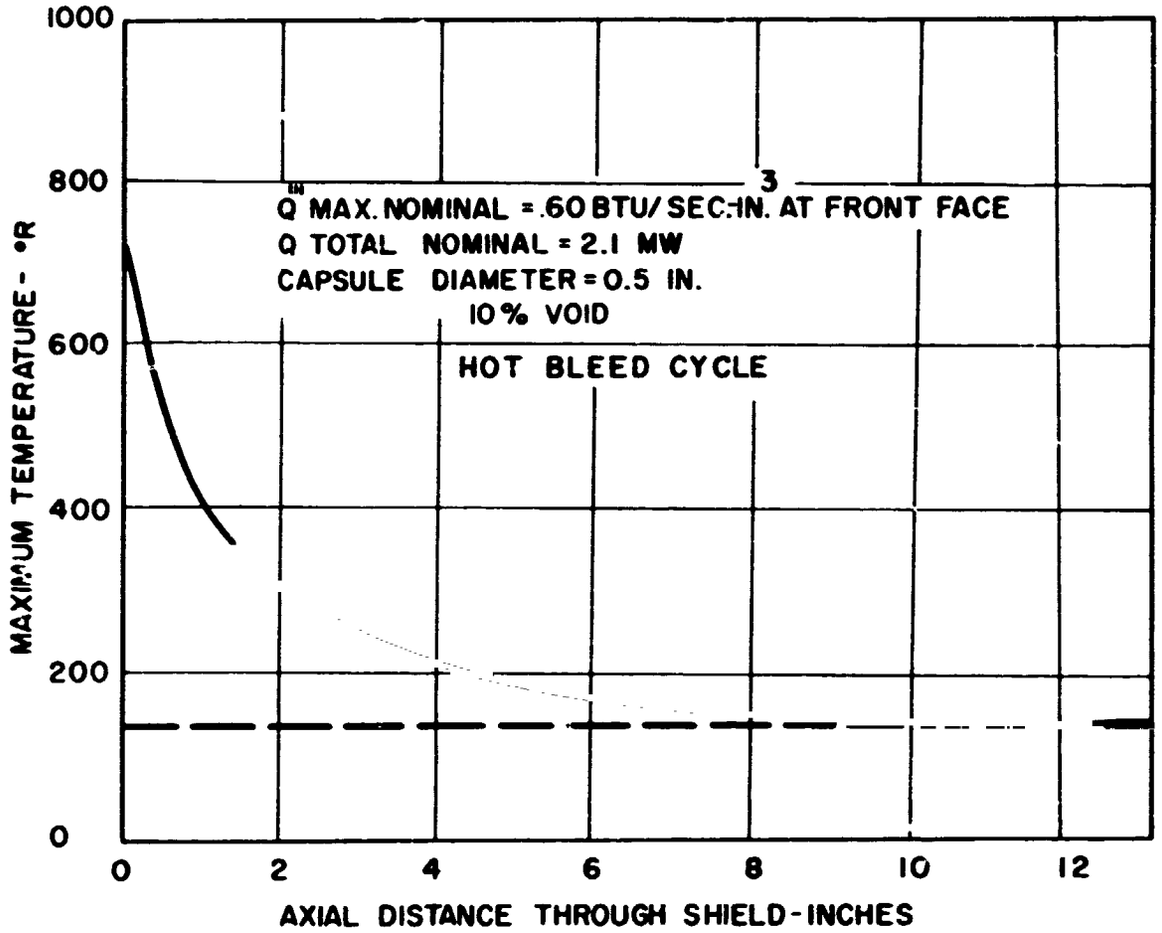

Figure 55 537411
Maximum Lithium Hydride Temperature as a Function of Distance into the Shield - Hot Bleed Cycle

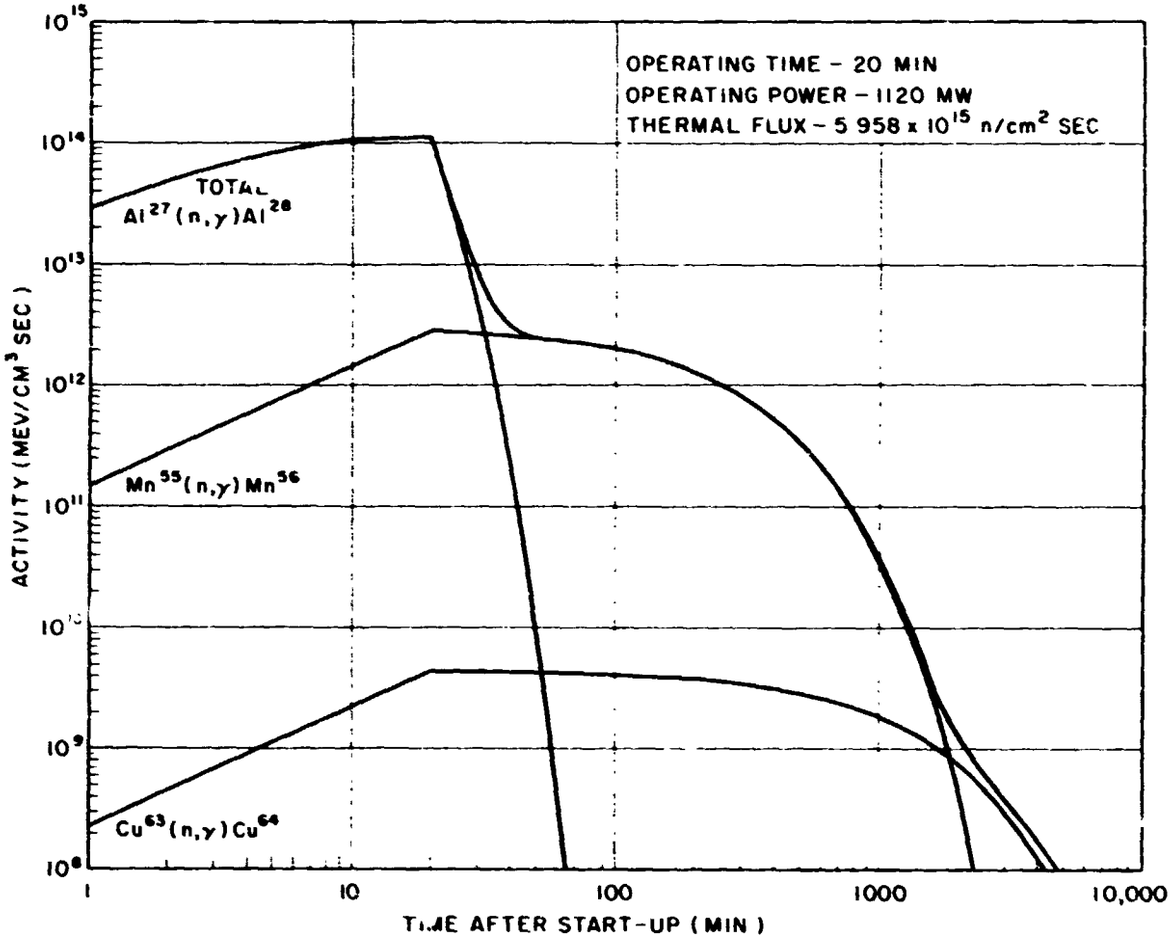

Figure 56

Activity in Aluminum

537559

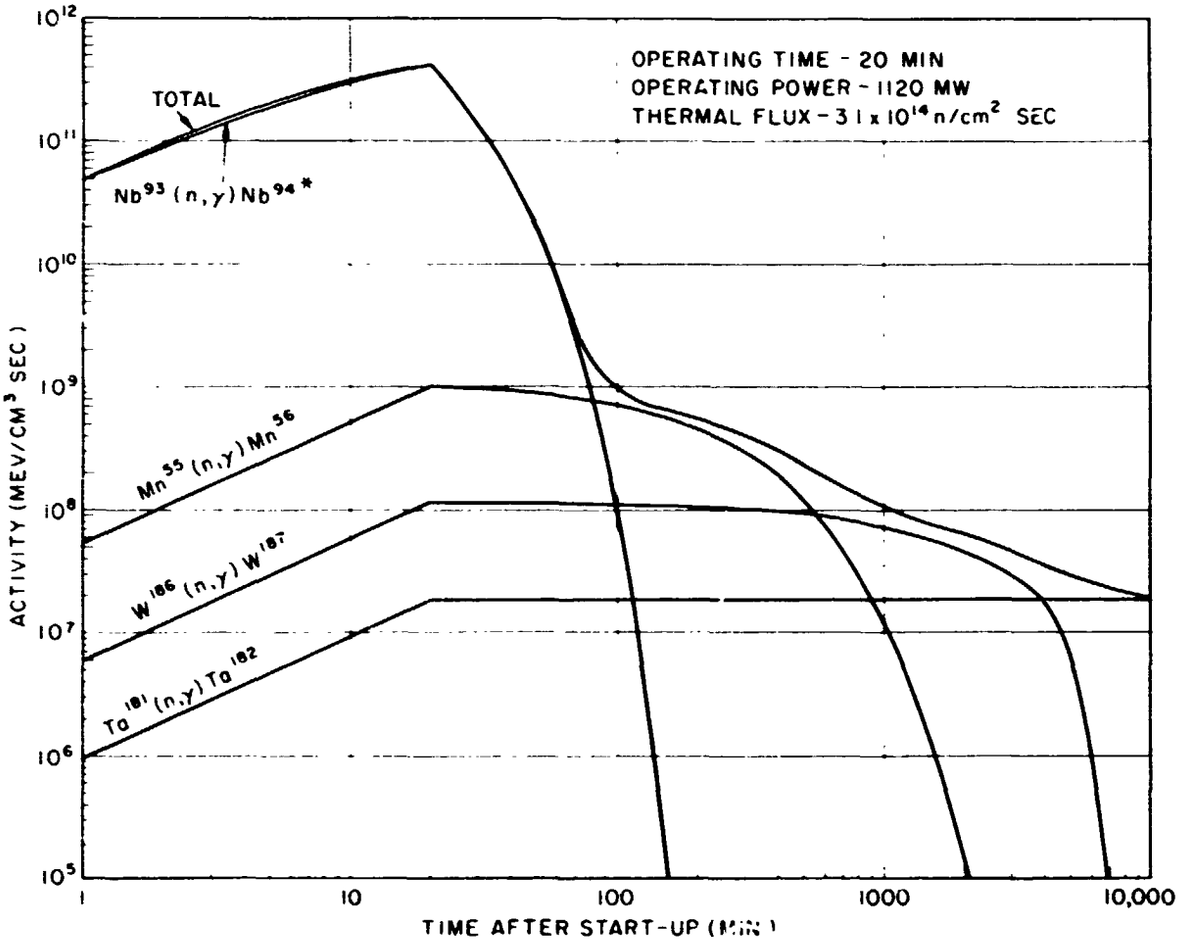

Figure 57

Activity in Niobium

537558

Astronuclear

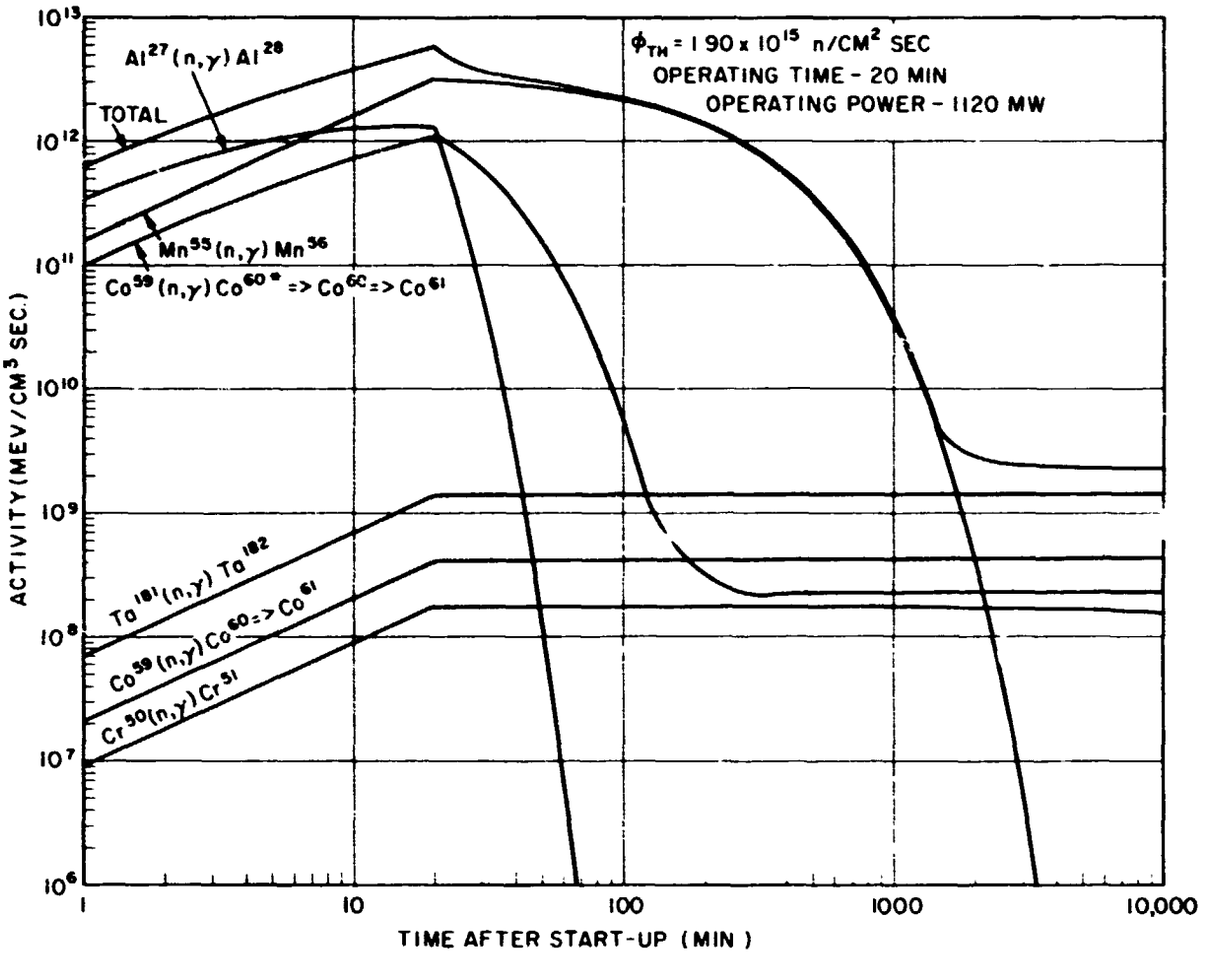

Figure 58

Activity in Inconel

537557

8.0 REFERENCES

1. XDC 59 - 2-16 — "Shielding Computer Programs, 14-0 and 14-1 Reactor-Shield Analysis", General Electric Company, Aircraft Nuclear Propulsion Department, J. T. Martin, J. P. Yalch, W. E. Edwards, June 15, 1959

2. WAPD 15 — "A Simplified Theory of Neutron Attenuation and its Application to Reactor Shield Design", Westinghouse Electric Corporation, R. D. Albert and T. A. Welton, November 30, 1950

3. WAPD - TM - 135 — "P1MG - A one-dimensional multigroup P1 Code for the IBM- 704," Bettis Atomic Power Division, Westinghouse Electric Corporation, H. Bohl, Jr., E. M. Gilbard, G. R. Culpepper, P. F. Buerger, July 1959

4. DC 59 - 7 - 170 — "Use of Program G-2 for Shielding Calculations", General Electric Company, Aircraft Nuclear Propulsion Department, J. W. Haffner, July 20, 1959

5. WAPD - TM - 39 — "The Calculation of Thermal Constants Averaged over a Wigner-Wilkens Flux Spectrum; Description of the SOFOCATE Code", H. Amster, R. Suarez, 1957

6. NAA Program Description — "TEMPEST", R. H. Shudde, J. Dyer, 1960

7. NDA 12 - 18 — "Penetration of Neutrons from a Point Fission Source Through Carbon and Hydrocarbons", Nuclear Development Corporation, J. Certaine, et.al., June 30, 1956

8. XDC 60 - 1 - 157 — "U^{235} Fission Product Activity", General Electric Company, Aircraft Nuclear Propulsion Department, M. R. Smith, 1960

9. AERE - R2938 "Radioistope Data", 1961

10. Nucleonics Data Sheet No. 28

11. WADD - TR - 60 - 56 "A Compendium of the Properties of Materials at Low Temperature", October, 1960